Anna Vadymivna Kladova

Metals in proteins from sulphate-reducing bacteria: adenylate kinase and ATP sulfurylase

Proteins containing cobalt, zinc, iron (II) ions

Ph.D. Thesis

A Thesis submitted at the Faculty Science and Technology of the New University of Lisbon for a degree in Doctor of Philosophy in Biochemistry with specialization in Physical Biochemistry

LISBON

2009

- nº de arquivo

- copyright

Dedicated to my parents

Acknowledgments

I have been fortunate enough to have been taught and allowed to work in the Laboratory of Biochemistry and Biophysics of Proteins at the Department of Chemistry at the New University of Lisbon under the supervision of Professor Dr. Sergey Bursakov. These years in my life represent a unique experience at the professional and personal levels.

I would like to thank Professor Dr. Isabel Moura and Professor Dr. José João Galhardas de Moura for receiving me at the Department and at the laboratory.

I would like to thank Professor Dr. Maria João Romão for her steadfast interest and attention to the work I was developing with cobalt/zinc-containing proteins. Over the years, I have had several colleagues who created an enjoyable and pleasant working environment at the Laboratory. Many thanks are due to Professor Dr. Cristina Costa, Professor Dr. Carla Carneiro, Professor Dr. Maria dos Anjos Macedo, Professor Dr. Jorge Caldeira, and Professor Dr. Stephane Besson.

My Thesis at the New University of Lisbon has had the invaluable help of many people that provided essential contribution to my work. I would like to thank the members of crystallography group of Professor Dr. M.J. Romão: Dr. Ana Luísa Carvalho, Cecília Bonifácio, Dr. Teresa Santos-Silva, Dr. Jóse Trincão, Dr. Abhik Mukhopadhyay and Dr. Shabir Najmudin.

Acknowledgements are also due to Ana Teresa Lopes, Celia Silveira, Alexandra Serra, Rui Almeida, Dr. Marta Santos, Dr. Marta Carepo, Dr. Raquel Grasina, Dr. Gabriela Almeida, Dr. Rui Duarte, Dr. Sofia Pauleta.

My gratitude goes also to several collaborators on this project from outside the New University of Lisbon for having made substantial contributions each in their own very personal way. I received excellent advice and assistance in the area of structural stability from Professor Valery Shnyrov from the University of Salamanca, Spain. I thank him for his friendship and for influencing much of my internal thought processes. I would like to thank also Dr. Juan J. Calvete from the *Instituto de Investigaciones Biomédicas,* CSIC, Valencia, Spain for his help and advice in the work with mass spectrometry measurements.

But my fondest thanks go to my parents. Only with your love, genuine interest in what I do and infinite care could I to start and complete this work.

Finally, thanks to everyone for lots of great memories!

I am formally grateful to the Foundation for Science and Technology, Portugal, for financial support (fellowship BD SFRH/BD/24744/05), with which this Thesis was made possible.

Summary

This work is devoted to the biochemical, biophysical and structural characterization of four proteins: cobalt-, zinc- and iron (II) - forms of adenylate kinase and Co^{2+}/Zn^{2+} form of native ATP sulfurylase from two anaerobic Gram-negative strains of the sulphate-reducing bacteria *Desulfovibrio (D.) gigas* NCIB 9332 and *D. desulfuricans* ATCC 27774, respectively. Both enzymes were found to be involved in the bioenergetic metabolism of SRB: AK contributes to the maintenance of constant levels of cellular adenine nucleotides and nucleic acid synthesis, ATP sulfurylase catalyses the first step of sulphate activation to accomplish the reduction of sulphate to sulphide that is used to drive oxidative phosphorylation.

The methods for the production of fully cobalt- zinc- and iron (II) -substituted forms of adenylate kinase of *D. gigas* overexpressed into *E. coli* were developed. As a result, homogeneous (with the ratio metal/protein 1/1) Co^{2+}-, Zn^{2+}- and Fe^{2+}- forms of the protein were produced.

The presence of metal ions in the LID domain affects the kinetic properties of AK. Holo-AK_{gig} shows the highest affinity of Fe^{2+}-AK_{gig} to the substrates of the backward reaction (MgADP/ADP), while Co^{2+}- and Zn^{2+}-AK_{gig} have the highest affinity to the substrates of the forward reaction AMP and MgATP, respectively. Thus, the magnitude of the K_m(AMP) and K_m(MgATP) could be depicted in the following order: Fe^{2+}-AK_{gig}>Co^{2+}-AK_{gig}≈Zn^{2+}-AK_{gig}, while for K_m(ADP,MgADP) this order is Co^{2+}-AK_{gig}> Zn^{2+}-AK_{gig}> Fe^{2+}-AK_{gig}.

According to the disparities in the apparent optimal temperatures of Co^{2+}-, Fe^{2+}- and Zn^{2+}-AK_{gig} for their AK activity (32 °C for Fe^{2+}-AK_{gig}, and 36 °C for Co^{2+}- and Zn^{2+}-AK_{gig}) the type of the metal ion in the LID mobile domain to some extent controls the temperature dependence of the catalytic activity.

Far UV-CD spectra analysis indicates no differences between secondary structural elements of holo-AK_{gig}, while tertiary structures of them, observed by near UV CD, are different. The major difference observed in tyrosine region for Fe^{2+}- form of AK_{gig} as compared to Co^{2+}- and Zn^{2+}- forms of AK_{gig}.

The thermal denaturation of Co^{2+}- and Zn^{2+}-forms of AK_{gig} (T_m values of 43.7 and 45.3 °C, respectively) was determined as a cooperative two-state process, sufficiently reversible at pH 10, that can be correctly interpreted in terms of a simple two-state thermodynamic model. In contrast, the thermally induced denaturation of Fe^{2+}-AK_{gig} is irreversible and strongly dependent upon the scan rate, suggesting that this process is under kinetic control. The changes between T_s values between holo-AK_{gig}, also indicates that the hydrophobicity of the Fe^{2+}-AK_{gig} is different, as the result of tertiary structure changes.

Well ordered diffracted crystals of Co^{2+}-, Zn^{2+}- and Fe^{2+}-AK_{gig} were obtained, and the structures were resolved with a resolution of 2.0, 2.1 and 3 Å, respectively. The carbon skeleton superposition of Zn^{2+}- AK_{gig} with Co^{2+}- and Fe^{2+}-AK_{gig} gives the rmsd values of around 0.1 and 0.37 Å, respectively, indicating very similar crystal structures for all of them. The NMA analysis indicates that metal ion nature does not influence the directionality of the substrate-binding domains (LID and AMP_{bd}).

The thermal denaturation process of ATP sulfurylase from *D. desulfurycans* was found to be strongly dependent upon the scan rate, suggesting that it is under kinetic control. The T_m and ΔH_{cal} values of the ATPS thermal denaturation process were found to be independent within the protein concentration range of 0.4 – 2.1 mg mL^{-1}, suggesting, that the dimer does not dissociate into monomers when unfolds. Thus, the mechanism of ATPS denaturation process can be presented on the basis of the simple kinetic scheme: $N_2 \overset{k}{\rightarrow} D_2$ with the value of the free stabilization energy of around 105 kcal per mol at 25 °C.

Phylogenetic analysis shows that the sequence of ATP sulfurylase from *D. desulfuricans* is posted together with other ATPS from mesophiles, whereas ATP sulfurylase from thermophiles or psychrophiles are located in different clades. At that point clade of psychrophiles ATPS is situated more close in comparison to that of thermophiles.

Well diffracted crystals of native ATP sulfurylase from *D. desulfuricans* were obtained. The structure was resolved to the resolution of 2.5 Å.

Sumário

Este trabalho tem como o objectivo a caracterização do ponto de vista bioquímico, biofísico e estrutural de duas enzimas, a cinase do adenilato (AK_{gig}) nas suas formas recombinantes contendo cobalto(II), zinco(II) e ferro(II), expressas em *E. coli* e Co/Zn ATP sulfurilase na sua forma nativa (ATPS), que está presente nas bactérias redutoras de sulfato, *Desulfovibrio (D.) gigas* NCIB 9332 and *D. desulfuricans* ATCC 27774 respectivamente.

Ambas as enzimas estão envolvidas no metabolismo bioenergético das bactérias redutoras de sulfato (BRS), sendo essencias para o seu crescimento e desenvolvimento. A cinase do adenilato contribui para a manutenção de níveis constantes da adenina e da síntese de ácidos nucleicos dentro da célula. A ATPS cataliza o primeiro passo da activação do sulfato para a sua posterior redução a sulfito, usado na redução de oito electrões envolvidos na fosforilação oxidativa.

A enzima AK recombinante foi sobre expressa em *E. coli* (na razão metal/proteína igual à 1/1) com obtenção das formas protéicas homogéneas contendo Co^{2+}-, Zn^{2+}- e Fe^{2+} .

A presença de iões metálicos no domínio LID da AK_{gig} afecta as suas propriedades cinéticas. Entre as holo-formas da AK_{gig} analisadas, o complexo Fe^{2+}-AK_{gig} demonstra a afinidade mais elevada para os substratos da reacção no sentido inverso (Mg^{2+}ADP/ADP), enquanto que os complexos Co^{2+}- e Zn^{2+}-AK_{gig} tem a maior afinidade para os substratos da reacção no sentido directo, que são AMP e Mg^{2+}ATP. Assím, a magnitude dos parâmetros K_m(AMP) e K_m(Mg^{2+}ATP) da reacção no sentido directo, presenta a seguinte ordem: Fe^{2+}-AK_{gig} > Co^{2+}-AK_{gig} ≈ Zn^{2+}-AK_{gig}, com os valores de Vm muito semelhantes. Os valores de K_m(ADP,Mg^{2+}ADP), para a reacção no sentido inverso seguem a ordem de Co^{2+}-AK_{gig} > Zn^{2+}-AK_{gig} > Fe^{2+}-AK_{gig}.

Foi testada a diferença nos valores da temperatura óptima para os complexos Co^{2+}-, Fe^{2+}- e Zn^{2+}-AK_{gig} na actividade da enzima. Os três perfis para a temperatura apresentam as formas semelhantes, com o valor máximo de 32 ºC para Fe^{2+}-AK_{gig} e 36 ºC para Co^{2+}-e Zn^{2+}-$AK_{gig.}$ Apesar de as diferenças na eficiência catalítica entre as formas enzimáticas contendo iões metálicos distintos serem relativamente pequenas, este resultado demonstra claramente que o tipo do metal presente no domínio móvel LID condiciona a dependência da actividade catalítica com a temperatura.

A espectroscopia CD na região distante de UV demonstrou que os elementos da estrutura secundária de todas as formas da enzima $AK_{gig,}$ em associação com ião são praticamente iguais, mas diferem ligeiramente da estrutura terciária, obtidos no espectro UV CD na região próxima.

A maior diferença é observada nas regiões ricas em resíduos da tirosina para o complexo Fe^{2+}-AK_{gig}, ao comparar com os complexos contendo cobalto e zinco.

Foi detectado o estado da desnaturação térmica reversível no valor de pH igual a 10, para os complexos enzimáticos com Co(II) e Zn(II), o que pode ser descrito pelo modelo simples de equilibrio de dois estados. Foram registados os valores de T_m de 43.7 ºC e 45.3 ºC para os iões de cobalto e zinco, respectivamente. No entanto, o processo da desnaturação térmica irreversível para Fe^{2+}-AK_{gig} apresentou o valor de T^* de aproximadamente 45 ºC. Uma diferença acentuada entre os valores T_s para Fe^{2+}-AK_{gig}, ao comparar com Co^{2+}- e Zn^{2+}-AK_{gig} demonstra que as propriedades hidrofóbicas de Fe^{2+}-AK_{gig} alteram como sendo o resultado da mudança na estrutura terciária.

Co^{2+}-, Zn^{2+}- e Fe^{2+}-AK foram cristalizados. Através do método de cristalografia de raio X, foram detectadas as estruturas cristalinas para todas as formas enzimaticas, livres do substrato, na resolução de 2.0, 2.1 e 3.0 Å para Co^{2+}-, Zn^{2+}- e Fe^{2+}- AK_{gig}, respectivamente. A sobreposição do esqueleto carbónico do complexo Zn^{2+}-AK_{gig} com Co^{2+}- e Fe^{2+}-AK_{gig} deu os valores de EQM (erro quadrático médio) de cerca de 0.1 e 0.37 Å, respectivamente, o facto que indica que todas as holoformas da enzima apresentam a estrutura cristalina semelhante.

O NMA (Normal Mode Analysis) identifica que as três formas enzimáticas exibem a mesma direccionalidade de dominios de ligação com os substratos (LID e AMP_{bd}), independentemente da natureza do ião presente no complexo.

Demonstrou-se que a pH 9.5 o processo da desnaturação térmica do ATPS de *D. desulfuricans* ATCC 27774 depende fortamente "upon scan rate" o que sugere que está submetido ao controlo cinético. Os valores de T_m e ΔH_{cal} para a desnaturação térmica de ATPS, à pH 9.5 não dependem da concentração proteica entre 0.4 à 2.1 mg mL^{-1} ao sugerir que o dímero no estado não dobrado não se dissocia para as formas monoméricas. O mecanismo da desnaturação da ATPS pode ser apresentado com base na esquema cinética simples: $N_2 \xrightarrow{k} D_2$, com o valor de energia livre de estabilização cerca de 105 kcal/mol à 25 ºC. A análise filogenética demonstrou que a sequência da ATPS de *D. desulfuricans* é semelhante às sequências para a mesma enzima em outros mesófilos, enquanto que ATPS de termófilos ou psicrófilos pertencem aos ramos filogeneticamente distintos. Conclui-se ainda que ATPS dos psicrófilos, é filogeneticamente mais próxima comparando com os termófilos.

ATPS foi cristalizada e a sua estrutura cristalina, livre do substrato foi determinada por cristalografia de raio X com a resolução de 2.5 Å.

Table of contents

Abbreviations and symbols

ε	molar extinction coefficient,
Abs	absorption
AK	Adenylate kinase
ADP	adenosine-5´- diphosphate
AMP	adenosine-5´-monophosphate
ATP	adenosine-5`-triphosphate
BSA	bovine serum albumin
CD	circular dichroism
DSC	differential scanning calorimetry
C_p	partial specific heat capacity
IPTG	isopropyl β-D-thiogalactoside
K_m	Michaelis-Menten constant
LB	Luria-Bertani Broth, Miller
LMCT	ligand-to-metal charge transfer
MALDI-TOF	matrix-assisted laser desorption-ionization - time of flight
SDS-PAGE	sodium dodecyl sulfate-polyacrylamide gel electrophoresis
T_m	temperature at the midpoint of the unfolding transition
UV	ultraviolet
rmsd	root mean square deviation
SRB	Sulphate-reducing bacteria
PP_i	Inorganic pyrophosphate
ATPS	Adenosine triphosphate sulfurylase
T_s	the temperature of maximum stability
ΔG	free energy changes
ΔH	calorimetric enthalpy changes
ΔH^{vH}	van't Hoff enthalpy changes
K_m	Michaelis constant
V_{max}	maximum initial velocity
AK_{col}	adenylate kinase from *Escherichia coli*
AK_{glo}	adenylate kinase from *Bacillus globisporus*
AK_{sub}	adenylate kinase from *Bacillus subtillis*
AK_{ste}	adenylate kinase from *Bacillus stearothermophillus*

AK_{aeol}	adenylate kinase from *Aquaflex aeolicus*
AK_{vol}	adenylate kinase from *Methanococcus voltae*
AK_{ac}	adenylate kinase from *Sulfolobus acidocaldarius*
ATPS	Adenosine-triphosphate sulfurylase
Da	Dalton
FPLC	Fast Performance Liquid Chromatography
PCR	Polymerase chain reaction
U	Units

Microorganisms

A. vinelandii	*Azotobacter vinelandii*
B. stearothermophilus	*Bacillus stearothermophilus*
B. subtilis	*Bacillus subtilis*
D. desulfuricans	*Desulfovibrio desulfuricans*
D. gigas	*Desulfovibrio gigas*
D. vulgaris	*Desulfovibrio vulgaris*
E. coli	*Escherichia coli*
P. denitrificans	*Paracoccus denitrificans*
T. brucei	*Tripanosoma brucei*
M. maripaludis	*Methanococcus maripaludis*
M. tuberculosis	*Mycobacterium tuberculosis*
Pn. chrysogenum	*Penicillium chrysogenum*
A. aeolicus	*Aquifex aeolicus*
Sc. cervisiae	*Saccharomyces cervisiae*
R. sphaeroides	*Rhodobacter sphaeroides*
T. thermophilus	*Thermus thermophilus* HB8
A. fulgidus	*Archaeoglobus fulgidus*
P. duponti	*Penicillium duponti*

Chapter 1

General introduction

Sulphate-reducing bacteria

Sulphate-reducing bacteria (SRB) are those prokaryotic microorganisms, both bacteria and archaea, that can use sulphate as the terminal electron acceptor in their energy metabolism, i.e. that are capable of dissimilatory sulphate reduction. SRB are widespread in nature and play important roles in sulphur cycles in soil, sediments from freshwater and marine environments, and deep-sea hydrothermal vents [1-3]. Generally they require a complete absence of oxygen and a highly reduced environment to function efficiently. Hydrogen sulphide- the final product of their respiratory metabolism process is chemically reactive and quite toxic to animals and plants. SRB are usually classified by their oxygen sensitivity and their ability to use sulphate as a terminal electron acceptor [4].

Members of this genus *Desulfovibrio* are the most readily cultured and best studied of the SRB. The bioenergetics of sulphate reduction in the genus *Desulfovibrio* is summarized in **Scheme 1** when the bacteria grow in presence of lactate and sulphate. The bacteria generate two ATP molecules by phosphorylation at substrate level coupled to the oxidation of two molecules of pyruvate. On the other hand, one ATP is consumed to activate sulphate to adenosine -5´-phosphosulphate (APS) and another ATP is used to regenerate two ADP molecules by adenylate kinase. The net production of ATP cannot be attained by substrate-level phosphorylation alone. Therefore, for growth on lactate and sulphate, *Desulfovibrio* has an obligatory requirement for electron transfer-coupled phosphorylation for the net production of ATP. The reduction of bisulphite to sulphide must compensate the energy investment of sulphate activation and yield additional ATP for growth. Three molecules of ATP are formed in an electrontransfer-coupled manner during the reduction of one molecule of sulphite to sulphide.

Thus, two key enzymes of energetic metabolism of SRB adenylate kinase and ATP sulfurylase are the objects of this work.

Reaction	**Enzyme**
$2lactate \leftrightarrow 2pyruvate + 4e^- + 4H^+$	lactate dehydrogenase
$2pyruvate + 2CoA \leftrightarrow 2acetyl\text{-}CoA + 2CO_2 + 2e^- + 2H^+$	pyruvate: ferredoxin oxidoreductase
$2acetyl\text{-}CoA + 2Pi \leftrightarrow 2acetyl\ phosphate + 2CoA$	phosphotransacetylase
$2acetyl\ phosphate + 2ADP \leftrightarrow 2acetate + 2ATP$	acetate kinase
$\mathbf{SO_4^{2-} + ATP \leftrightarrow APS + PPi}$	**ATP sulphurylase**
$MgPPi + H_2O \leftrightarrow 2Pi + Mg^{2+}$	inorganic pyrophosphatase
$APS + 2e^- \leftrightarrow SO_3^{2-} + AMP$	APS reductase
$\mathbf{AMP + ATP \leftrightarrow 2ADP}$	**adenylate kinase**
$SO_3^{2-} + 6e^- + 8H^+ \leftrightarrow H_2S + 3H_2O$	sulfite reductase
$2lactate + SO_4^{2-} + 2H^+ \leftrightarrow 2acetate + 2CO_2 + H_2S + 2H_2O$	net reaction

Scheme 1. The bioenergetics of sulphate reduction [5, 6].

Adenylate kinase

Adenylate kinase (EC 2.7.4.3. ATP:AMP phosphotransferase) catalyzes the reversible transfer of the γ- phosphate group from Mg^{2+}ATP to the phosphate moiety of AMP, producing Mg^{2+}ADP and ADP with high-energy turnover [7]:

$$AMP + Mg^{2+}ATP \rightleftharpoons ADP + Mg^{2+}ADP$$

AK also catalyses, to a lesser extent, the following reaction [8, 9]:

$$ADP + Mg^{2+}ATP \rightleftharpoons AMP + Mg^{2+}Ap_4$$

This reaction has an absolute requirement for Mg^{2+} and occurs at a lower rate by way of an associative type in-line displacement without an enzyme bound intermediate [10].

The role of AK is to facilitate the storage and use of the high energy of adenine nucleotides in cell. AK is an essential catalyst for bacterial growth and multiplication and belongs to a family of essential enzymes since its inactivation is not compatible with cell survival [11].

There are two oligomeric classes of AK: monomeric as found in Eubacteria and trimeric as found in Archaebacteria [12]. The sequence identity and structure of AK from Eubacteria and Archaea are related only distantly, suggesting that archaeal AK belong to a different AK class. The crystal structures have been determined for several members of both classes [13, 14]. In the same time AK from *Paracoccus denitrificans* (AK_{den}) was determed as a dimer [15, 16], but no structure is available till now.

The structure of the trimeric AK from the mesophile Archaebacteria *Methanococcus maripaludis* (AK_{mar}), which has T_m (temperature at the midpoint of the unfolding transition) value close to 74 ° C, has been solved to the resolution of 2.5 Å in Ap5A inhibitor presence. Consistent with other methanococcal AK, the trimeric interface is comprised of a three-helix bundle formed by the long helix of each subunit (**Fig. 1**). The potentially important intrasubunit ion-pair was identified at the trimeric interface of AK_{mar} between Glu150 and Arg156 with the average distance of 3.35 Å.

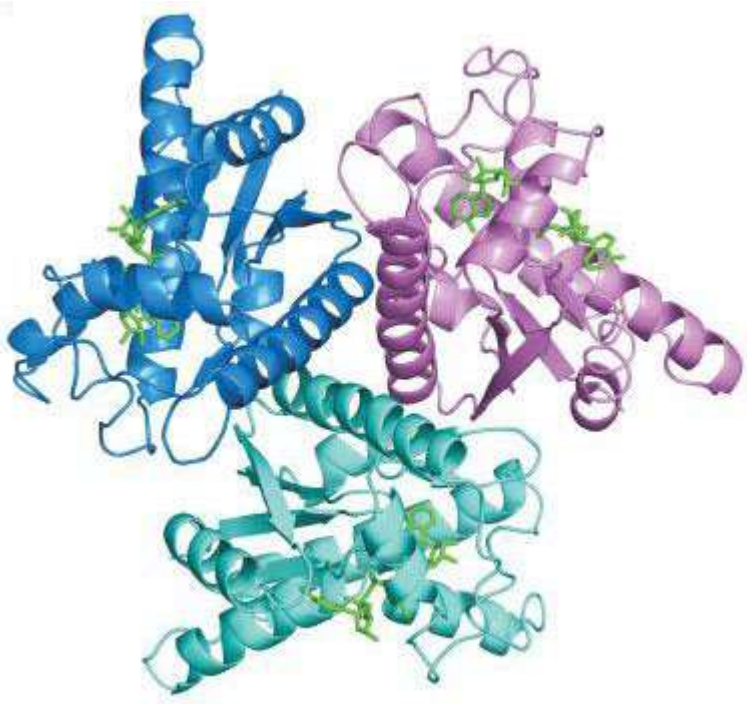

Fig. 1 Trimeric structure of AK_{mar}, the trimeric interface consists of a three helix bundle. The bound Ap5A molecule (green) spans the active site of the enzyme [12].

All AK share a highly related tertiary structure with the five-stranded parallel β-sheet with helices on both sides and could be divided into three main domains: the CORE, the LID and AMP binding domain (AMP_{bd}) or also called NMP_{bd} (**Fig. 2**):

The CORE (^{1}Met-^{29}Ile, ^{60}Thr-^{121}Val, ^{160}Gln-^{214}Gly for AK from *E. coli* (AK_{col})) is the largest domain that includes the central parallel β- sheet and the immediately packed helices (β_1-β_4 and β_9 surrounded by helices α_1 and α_4-α_9 for AK_{col}). This domain is the most similar among AK. It contains the P-loop that plays an important role in ATP binding. This binding motif is the general feature among proteins that bind nucleoside triphosphates, in all nucleoside monophosphate kinases, and in the weakly homologous guanine nucleotide-binding proteins (G-proteins) [17]. Residues 7-15 in the P-loop and residues 198-214 in the C- terminal helix of AK_{col} with its connecting loop region form the ATP binding site.

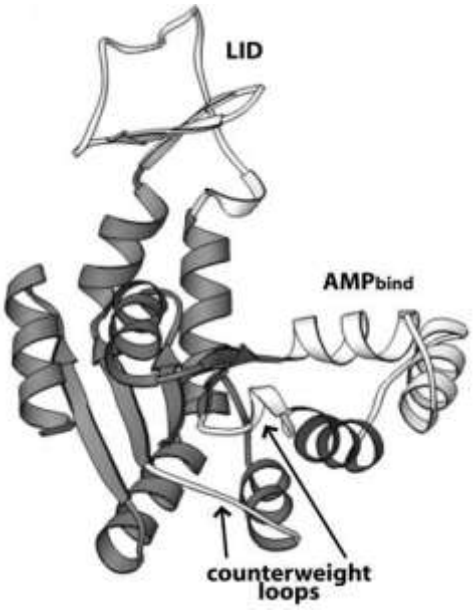

Fig. 2 Structure of AK_{col} on the open conformation [17].

The AMP_{bd} domain (^{30}Ser-^{59}Val for AK_{col}) is helical (α_2 and α_3 for AK_{col}) and contributes to the AMP binding, closing over bound AMP.

The LID domain (^{122}Gly-^{159}Asp for AK_{col}) includes a four stranded antiparallel β-sheet (β_5-β_8 for AK_{col}). In long-type AK this domain consists of around ~37 amino acid residues and only a short loop in the other AK. The LID domain is well solvent exposed domain that undergoes large movement during catalysis and upon substrate binding, closing over the active site [18] and protecting the MgATP/AMP-ternary complex from bulk water, facilitating phosphoryl transfer and preventing hydrolysis [19]. The amino acid sequences of the LID domains are highly conserved among the long type AK. The LID domain of AK containing Zn^{2+} has its chain fold the same as those of other LID domains [20]. LID has been suggested to interact with other cellular components, fulfilling further functions [21].

Generally, AK from Gram-positive bacteria contain a Cys-X_2-Cys-X_{16}-Cys-X_2-Cys/Asp structural motif in its LID domain that is responsible for the binding of zinc ion [13, 20, 22], whereas the AK from Gram-negative bacteria are usually devoid of metal ions, since their Cys residues are substituted by another four highly conserved amino acids - His, Ser, Asp and Thr, respectively [23]. Nevertheless, previously published exceptions are AK from *Desulfovibrio gigas* and *Desulfovibrio desulfuricans* ATCC 27774, that contain either cobalt or zinc [24], the AK from *Paracoccus denitrificans*, overproduced in *E. coli* [15, 16], that binds either zinc or iron, and the AK from *Chlamidia pneumoniae* and *Thermotoga neapolitana*, that contain zinc [25, 26]. Metal ion in AK was proposed to play rather structural than catalytic role [23, 27], enhancing thermal stability of the enzyme. Thus, mutant of AK from *E. coli* with genetically engineered zinc binding site has T_m value of 61.6 °C, while for native apo- form only 52.5 °C

with comparable kinetic parameters [23]. Removal of the metal ion in AK_{gig} was accompanied with decreasing of T_m up to 5.3 °C with invariable heat capacity, indicating that removal of metal ion does not result in any appreciable decomposition of the structure of the enzyme [28]. Previous studies have shown also that zinc depletion reduces T_m value by 7.5 °C and 6.3 °C in AK from *Bacillus stearothermophilus* and *T. neapolitana*, correspondingly [26, 29].

The study of series of chimeric AK based on mesophile *Bacillus subtilis* and the thermophile *Bacillus stearothermophilus*, that share high sequence homology (74 %), indicates that CORE domain governs overall stability of the enzyme, while two other mobile domains themselves (the AMP and LID domains) control the temperature dependence of the catalytic activity [30].

The catalytic mechanisms of bacterial and eucaryotic AK have been studied extensively, mainly due to their biological importance and ubiquitous distribution of the enzyme [7, 17, 31-35]. The presence of two substrate binding sites per AK molecule has been shown: the one site for metal-free substrates (AMP and ADP) and another for metal-bound substrates (Mg^{2+}ATP and Mg^{2+}ADP). The basic kinetic mechanism was proposed to be random Bi Bi, where binding of any of two substrates (Mg^{2+}ATP, for instance) favours bound of the second one (AMP), that causes the products production (Mg^{2+}ADP and ADP) [31]. Later on, an iso- random Bi Bi mechanism was proposed [36]. The major difference of the iso- Bi Bi mechanism is the presence in equilibrium at least two forms of enzyme, where the first form can bind substrates of the forward reaction (Mg^{2+}ATP and AMP), whereas the other can bind substrates of the reversed reaction (Mg^{2+}ADP and ADP). The conformation of the ternary complex of AK in a complex with AMP and Mg^{2+}ATP is different from that of enzyme binding with ADP and Mg^{2+}ADP. Thus, AK undergoes at least two steps of conformational changes. One step is the change of a ternary complex with bound substrates to one with bound products during the reaction, and the other is the change of free AK into different forms. In a catalytic cycle, the conformational changes of the free enzyme and the ternary complexes are the rate-limiting steps. This mechanism is based on the fact that AK undergoes large domain movements upon substrate binding [37].

AK are in general very specific with respect to phosphate acceptors [7, 38]. However, in several enzymes some activity was observed when AMP was substituted by 5´-AMP and dAMP [7, 39]. The short form of AK from *Tripanosoma brucei* can use AMP, CMP and UMP as an acceptors [40]. Human AK5 uses AMP and dAMP with equal efficiency and can use CMP and dCMP. Human AK6 uses AMP and dAMP as preferred substrates, but CMP, dCMP and to a much less extent IMP also can be phosphorylated [41]. Among nucleoside monophosphates other than AMP: 2´dAMP, 3´dAMP and AraAMP act as good acceptors for AK from *Y. pestis*

[42]. AK are not very specific with respect to phosphate donors. All AK except SK3 and AK6 prefer Mg^{2+}ATP at the ATP site and can be substituted with 2`-dATP, GTP, CTP, UTP, or ITP to some extent [7, 38]. AK3 can use both GTP and ITP as effective phosphate donors, but GTP is most probably the physiological substrate [7]. AK6 can use all NTPs and dNTPs with CTP as the best phosphate donor [41].

A bivalent metal ion is required for AK activity. Thus, for rabbit and yeast AK the order of reactivity is $Mg^{2+} > Mn^{2+} > Ba^{2+}$ and $Mg^{2+} > Ca^{2+} > Mn^{2+} > Ba^{2+}$, respectively, while for bovine liver AK the order is different: $Mg^{2+} > Mn^{2+} > Ca^{2+}$, Co^{2+}. In spite of the individual differences observed, the Mg^{2+} ion shows the highest activity [7]. The ATP, ADP and AMP species bind magnesium ion with very different stability constants. Moreover, Mg^{2+}-bound and Mg^{2+}-free species have quite diverse, sometimes opposite, effects on enzymes. Nucleoside triphosphates bind magnesium very tightly, and their actions as cofactors and energy-rich compounds are carried out in complexes with Mg^{2+}. Nucleoside diphosphates bind Mg^{2+} with a less extent (the stability constant is 2500 M^{-1}) [7], and the enzymes that use Mg^{2+}ADP are usually strongly inhibited by free form of ADP. The uncomplexed forms of both ADP and ATP may cause appreciable inhibition of the kinase-type phosphotranferase enzyme systems [43, 44]. Nucleoside monophosphates, particularly AMP, that allosterically regulates many key enzymes, bind Mg^{2+} very weakly [45] and participate in metabolic processes in the magnesium-free form [43].

AK require a bivalent metal ion for its efficient catalytic activity and, as was mentioned before, Mg^{2+} shows the highest activity through binding with ATP forming Mg^{2+}ATP. Magnesium ion serves to neutralize the highly negative charge of the ATP, thereby reducing electronic repulsion of the transferred phosphate and increasing the efficiency of nucleophilic attack. In AK, conserved serine, threonine, or aspartate residues participate in binding the Mg^{2+}, coordinating it either directly in the first coordination sphere or indirectly through water molecules. In the structure of AK from *B. stearothermomophilus* (AK_{bst}), magnesium ion is coordinated to β- and γ-phosphates of ATP and four water molecules (300-303) [20]. Binding of the Mg^{2+} activates catalysis by orienting phosphate donor and acceptor for further phosphoryl transfer. Two of the four water molecules (300 and 303), are within hydrogen bound distances from the α-phosphate of AMP. Water molecule 300 is hydrogen bounded to ^{33}Asp and ^{36}Arg. The last residue interacts with the phosphate of AMP and is highly conserved. Water molecules 301 and 303 are hydrogen-bonded to ^{84}Asp, while 301 to ^{14}Gly. Water molecule 302 reinforces the linkage between phosphate and Mg^{2+}, interacting with the oxygen atoms of the α-, β-, and γ-phosphates of ATP.

Thus, two (300 and 303) of the four coordinated water molecules act to bridge the gap between phosphate chains, linking together and stabilizing the motion of the two phosphate

chains at the active site [20]. This assembles a functional ternary complex in which the phosphate oxygen atoms of AMP is free to attack the Mg^{2+} polarized γ-phosphate of ATP. Once phosphate transfer has occurred, the interactions between two water molecules (300 and 303) with the new ADP α-phosphate and residues ^{33}Asp and ^{36}Arg connected with these molecules provides a new scaffolding for the Mg^{2+} coordination complex and a starting point for the back reaction. Water molecule 302 may then act to facilitate the back reaction by hydrogenbonding back to the terminal phosphate of the ADP in the Mg^{2+}ADP/Mg^{2+}ATP binding site.

The partially open position of the LID domain has increased access of the bulk water to the active site compared to the fully closed position. This serves to hydrate both the phosphates chains of the substrates/products and the polar residues of the LID. Bulk water, which is excluded from the active site during the reaction, can then interrupt the binding of the phosphate chains by replacing hydrogen bonds to the protein with hydrogen bonds to water molecules [20].

Two water molecules 218 and 220 in the crystal structure of AK_{col} (**Fig. 3**), that correspond to water molecules 300 and 302 from AK_{bst} have additional H-bonds interactions with ^{156}Arg [46]. ^{156}Arg has been implicated in the stabilization of the transition state of the phosphoryl transfer reaction of the enzyme. The ^{156}Arg side chain mobility between binding states suggests the stabilizing role of the top (the LID domain side) of this amino acid, while ^{13}Lys and the Mg^{2+} stabilize the bottom and the front [47].

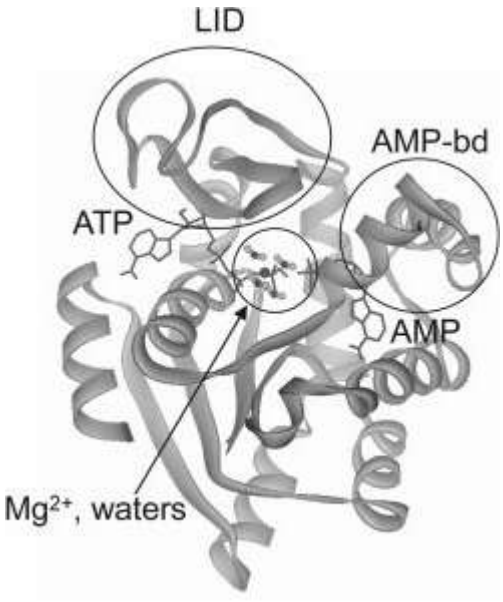

Fig. 3 Structure of AK from *E. coli* on the closed conformation; ATP, and AMP are in stick representation; the Mg^{2+} atom and its 4 coordinating water molecules are in a ball-and-stick representation [46].

The ^{84}Asp main and side chains from AK_{col} form a stable network of H-bonds with ^{30}Ser and ^{31}Thr and water molecules [46]. The ^{31}Thr residue in its own turn is linked to AMP molecule. These interactions anchor AMP to the Mg^{2+} complex involving the ATP phosphate

chain. ^{84}Asp also forms a salt bridge with ^{13}Lys in P-loop. ^{13}Lys stabilizes the active site by forming H-bonds and salt bridge-like interactions with both ATP (β-PO_4) and AMP (α-PO_4) using its flexibility and multifunctionality. In addition to Lys, Mg^{2+}, its coordination waters, and some surrounding charged residues maintain the geometry and distances of the AMP α-phosphate and ATP β- and γ-phosphates in a configuration that suggests that phosphoryl transfer occurs by associative mechanism in AK [46]. The results of oxygen-18 kinetic isotope effect experiments support the notion that phosphoryl transfer occurs through an associative transition state [48].

Recent analysis shows, that the Lys171, in human AK4, which is located in a hinge that binds LID and CORE domains and is strickly conserved in all AK family is essential for orientation of the LID domain (**Fig. 4**). Thus, the provided mutation of Lys171Pro dramatically changes the orientation of the LID domain, which could be described as a novel twistedand-closed conformation in contrast to the open and closed conformations in other AKs [49].

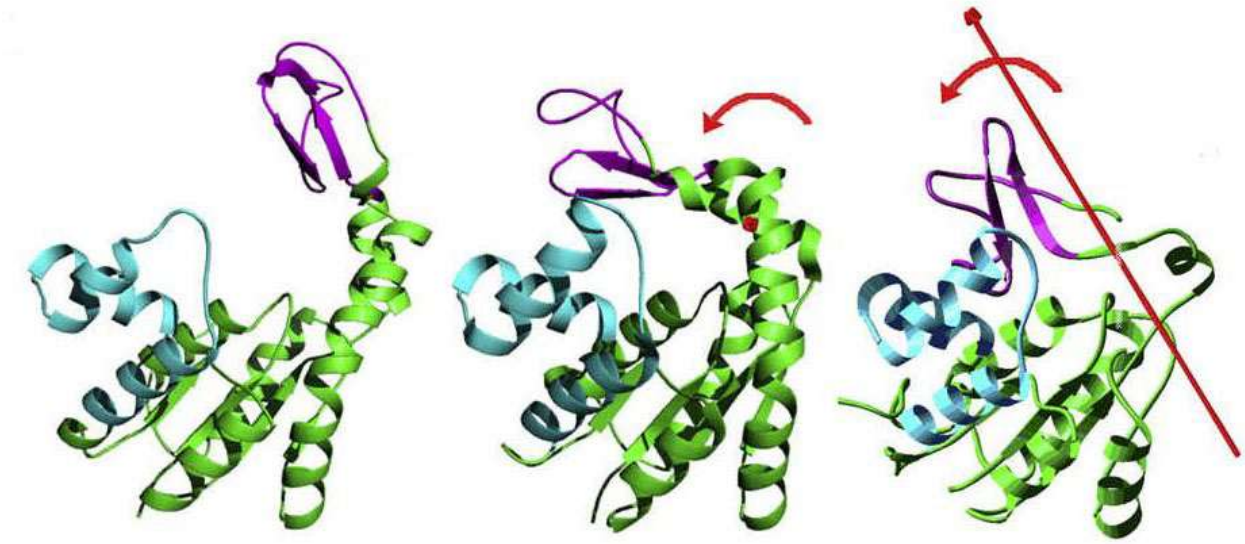

Fig. 4 Overal structural comparison of human AK4 Lys171Pro mutant with the native AK4 in open and closed form (left is native AK4 open form, middle is native AK4 bound with GP5 in close form and right is the AK4 Lys171Pro [49].

Adenylate kinase from *D. gigas* is monomeric enzyme with the molecular mass of 24.7 kDa that bind either cobalt (II) or zinc (II) ions [27]. The UV-Vis spectrum of AK_{gig} contains the following peaks at around 278 nm, ligand-to-metal charge transfer (LMCT) at 312, 320 and 338 nm and d-d transitions at 610, 647 and 688 nm. The EXAFS data revealed that either cobalt or zinc ions in AK_{gig} contain the same mixed metal-sulphur and metal-nitrogen environment. The analyses of X-ray crystallography data indicated that the bound Zn^{2+} was located in the LID domain of the AK_{gig} and it is tetrahedrally coordinated to three cysteines and one histidine in a motif ^{129}Cys-X_5-His-X_{15}-Cys-X_2-Cys, which is similar, but not identical, to the putative zinc-

binding motif in another AK. Both metal ions were reported to play rather structural than catalytic role.

ATP sulfurylase and sulphate activation

The sulphate reduction plays a very important role in the sulphur cycle. Most plants and microorganisms can use inorganic sulphate as their sole source of sulphur. Because sulphate is nonreactive at cellular temperatures and pH, the anion must first be ″activated″ in order to enter the mainstream of metabolism [50]. In biological systems, sulphate is chemically activated via adenylation. Activated substrate is ready to be used by essential biological processes such as the biosynthesis of reduced sulphur metabolites, driving oxidative phosphorylation; sulphuryl group donation, modification of neuropeptides and peptide hormones, cell-cell adhesion, detoxification, homeostasis processes that may be critical for life.

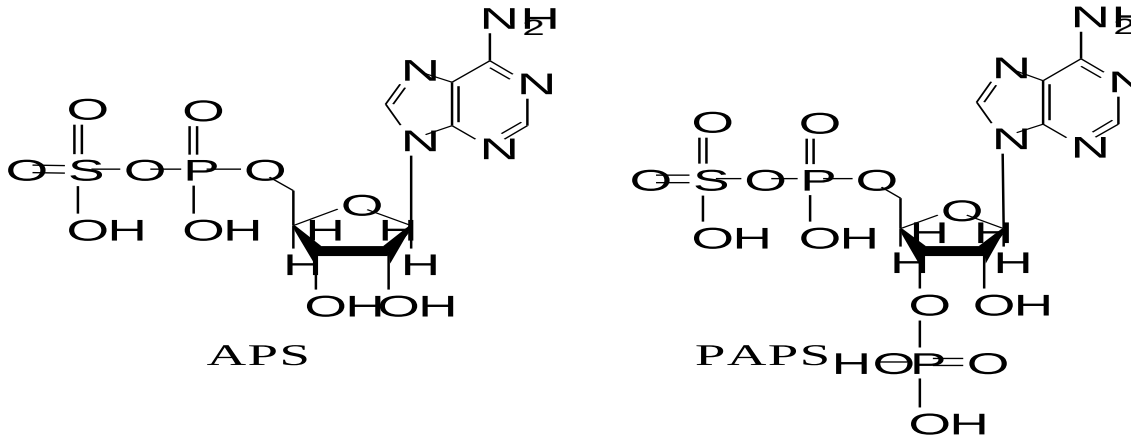

Fig. 5 Structural formulas of APS and PAPS.

ATP sulphurylases (EC 2.7.7.4. MgATP:SO_4^{2-} adenylyltransferase) are ubiquitous enzymes that catalyze the transfer of the adenylyl group from ATP to inorganic sulphate, yielding adenosine-5´-phosphosulphate (APS) (**Fig. 5**) and pyrophosphate (PP_i):

$$MgATP + SO_4^{2-} \rightleftharpoons APS + MgPP_i$$

The phosphoric-sulfuric acid anhydride bond of APS has a free energy of hydrolysis that is approximately twice that of the replaced pyrophosphate bond of ATP [51], making the synthesis of APS and the inorganic pyrophosphate a highly unfavourable reaction. This energy dilemma is resolved differently in different organisms.

One strategy to overcome this thermodynamic barrier would be to remove the ATP sulfurylase-catalyzed reaction products in a subsequent step of the pathway, thereby limiting the reverse reaction and shifting the equilibrium toward APS synthesis. Alternatively, APS synthesis could be coupled to a highly exergonic reaction. Some bacteria employ the latter strategy by

coupling APS synthesis to GTP hydrolysis [52, 53]. However, the APS-synthesizing enzyme in these bacteria (known as CysD) is unrelated to the APS-synthesizing enzyme found in most other organisms [54]. The GTP-hydrolyzing enzyme (known as CysN) is also specific to these bacteria [55].

In the reductive branch of the pathway, APS-reductase reduces APS to sulfite, with thioredoxin, providing the reducing potential. Additional enzymatic steps subsequently reduce sulfite to sulfide and incorporate the latter into thiol- and sulfur-containing molecules as previously mentioned. Alternatively, APS may undergo further activation into 3'-phosphoadenosine 5'-phosphosulfate (PAPS), the activated sulfate donor needed for sulfation. APS is activated into PAPS by the phosphorylation activity of APS-kinase (EC 2.7.1.25. ATP:adenylylsulfate-3-phosphotransferase):

$$MgATP + APS \rightleftharpoons MgADP + PAPS$$

PAPS is used by all sulfotransferase enzymes to covalently attach sulfate to carbohydrates, proteins, and small organic molecules. PAPS can also be reduced to sulfite via a PAPS-reductase [56].

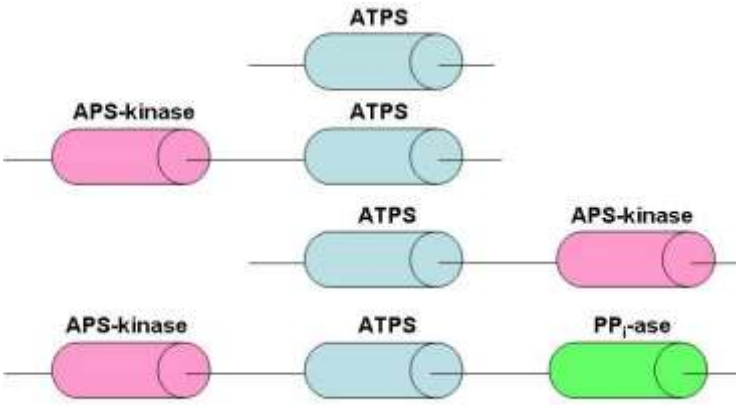

Fig. 6 Structural architecture of the ATPS family of proteins.

In most plant and microbial cells, ATP sulfurylase, APS kinase and PP_i-ase are separate proteins. However, animals and some bacteria possess a ″PAPS synthetase″ in which the two sulphate activating enzymes are co-located on a single polypeptide chain in some cases [57]. Besides, ATP sulfurylase can fused also with APS-kinase and pyrophosphatase (PP_i-ase) are known (**Fig. 6**) [56].

In metazoans, a fused, sequentially acting bifunctional enzyme, commonly known as PAPS synthetase, has both APS kinase and ATP sulfurylase activities [58]. This fusion protein has the APS kinase domain at the amino-terminal end of the protein, followed by the ATP sulfurylase domain [59, 60]. The exclusive function of the kinase-sulfurylase fusion protein in metazoans is thought to be PAPS synthesis for use by sulfotransferase enzymes. It has been

argued that the kinase-sulfurylase fusion protein enables the labile APS intermediate to be rapidly 'channeled' from the sulfurylase active site into the neighboring kinase active site [61-66]. In some fungal and bacterial species, a fusion of the ATP sulfurylase and APS kinase domains is found with a reversed domain order (**Fig. 6**) relative to the metazoan gene have been described from the filamentous fungi *Penicillium chrysogenum* [67], the chemolithotrophic bacterium *Aquifex aeolicus* [68, 69] the budding yeast *Saccharomyces cerevisiae* [70], and the proteobacterium *Rhodobacter sphaeroides* [66]. The kinase domain of the sulphurylase-kinase fusion protein is not well conserved, and a range of functions has been attributed to the kinase domain in different organisms. In *S. cerevisiae* the APS kinase domain of sulfurylase-kinase fusion is important for the quaternary structure of the enzyme but is highly degenerate at the sequence level [71]. In *Penicillium chrysogenum* the kinase domain of sulfurylase-kinase protein serves as a PAPS-binding allosteric regulator of the sulfurylase domain and has lost all APS-kinase activity [72, 73]. In *Aquifex aeolicus* and *Rhodobacter sphaeroides* the kinase domain of sulfurylase-kinase fusion protein still functions as an APS-kinase [66, 69].

In several protozoan genomes within the Stramenopile lineage was discovered a novel triple fusion protein of ATP sulfurylase, APS and pyrophosphatase (PP_i) also located on a single polypeptide chain (**Fig. 6**) [56].

It appears, that isolated from different sources, ATP sulfurylase family is heterogeneous in terms of amino acid sequences, molecular masses, subunit composition and behaviour. Two completely different, unrelated types of ATP sulfurylase can be distinguished:

1. The heterodimeric type, which occurs exclusively in sulphate-assimilating prokaryotes, e.g. two subunits with masses of 23 and 53 kDa in *Escherichia coli* K-12 [51], 35 kDa and 68 kDa in *M. tuberculosis* [74], nodulating, and some other bacteria [51].

2. All other ATP sulfurylases characterized in sufficient detail are monomers, dimers and hexamers with a range of molecular masses from 38 to 69 kDa per subunit [75, 76]. Correspondingly, size variations are due to APS kinase, PAPS or PP_i-binding allosteric domains residing on the same polypeptide [56, 57, 64, 67, 70, 75, 76].

The amino acid sequences alignment of ATP sulfurylases from yeasts, bacteria, plants, fungi and mammals shows highly conserved regions with a high content of basic amino acid residues, considered to be the binding sites for Mg^{2+}ATP and SO_4^{2-}. The highly conserved active site of ATP sulfurylases mainly includes three motifs: QXRN, GRD and HXXH. The HXXH motif is a common feature of nucleotidyl transferases [77]. Site directed mutagenesis experiments have demonstrated that residues His(s) from the HXXH motif and the Arg from the QXRN motif are essential for ATP sulfurylase activity [78]. The His(s) of the HXXH of ATP

sulfurylase binds and stabilizes the PP_i group of ATP before and during hydrolysis of the α, β-bond, and assist the dissociation process [70].

ATP sulfurylase are in general very specific to ATP. Thus, only ATP and to a lesser extent dATP serve as effective substrates, although the latter was not tested for ATP contamination [79, 80]. The preference of adenine nucleotides can be explained by a hydrogen bond in which the N1 nitrogen of the adenine ring is the hydrogen acceptor and the main chain amide of Val333 of ATP sulfurylase from *Penicillium chrysogenum* is the hydrogen donor [81]. Pyrimidine nucleotides would be too far from the Val333 main chain amide to make this hydrogen bond and N1 nitrogen of guanine nucleotides is protonated and thus cannot be a hydrogen bond acceptor.

The real substrate for ATP sulfurylase catalysis is magnesium complex of ATP, while free ATP is the competitive inhibitor. Magnesium ions required for catalysis and not for nucleotide binding [82]. In the reverse direction, only $MgPP_i$ is ATPS´s substrate, while divalent oxyanions [X = molybdate (MoO_4^{2-}), selenate (SeO_4^{2-}), tungstate (WO_4^{2-}), chromate (CrO_4^{2-}), and also arsenate ($AsHO_4^{2-}$)] can inhibit ATP sulfurylase [79]. They render adenosine phosphate complexes (APX) unstable and spontaneously hydrolyze to form AMP. The monovalent oxyanions (perchlorate (ClO_4^-), nitrate (NO_3^-), chlorite (ClO_3^-), and fluorosulphonate (FSO_3^-) also compete with sulphate for ATP sulfurylase, thereby inhibiting APS formation. However, they differ from the divalent oxyanions in that APX complexes are not formed [79, 80].

The stereochemical course of the reaction catalyzed by the ATP sulfurylase from yeast has been determined. It proceeds with an inversion of the stereochemistry at the α-phosphoryl moiety, suggesting that the reaction follows an ″in-line″ nucleophilic attack by SO_4^{2-} at the α-phosphoryl group of ATP [83]. The structural data confirm this substitution mechanism (see below) that leads to direct APS formation with PP_i as the leaving group and without covalent adenylyl-enzyme intermediates formation [70]. The enzyme provides suitable binding sites for ATP and sulphate, brings the reactive groups in close contact, and promotes stabilization of the nucleotide conformation that is most favourable for ″in line″ attack of the sulphate. Thus, the β-phosphate group of ATP is hydrogen-binding to the one His residue of HXXH and Arg of GRD motifs, while other His coordinates the γ-phosphate of ATP, SO_4^{2-} binds to QXRN and GRD motifs. The mechanism for ATP sulfurylase from *Penicillium crysogenum, Aquifex aeolicus* and rat liver was proposed to be random for the forward reaction substrates (ATP and SO_4^{2-}) and preferred order for the backward reaction substrates (for the first APS ligation and only then PP_i) [69, 80, 84]. The mechanism operates in a similar way for both spinach leaf and, probably, *Riftia* enzymes [85, 86].

The crystal structure of ATP sulfurylase from *Thermus thermophilus* HB8 [87] has special interest for this work because of its dimeric nature and zinc-chelating properties that makes it to

be much more similar to that of *D. desulfuricans*. The ATP sulfurylase of *Thermus thermophilus* is composed of a N-terminal domain (residues 1-34), a catalytic domain (residues 135-290) and domain III (residues 291-347), but it lacks a C-terminal domain. APS is located in the active site of ATP sulfurylase, which contains several conserved motifs (QXRN, HXXH and GRD). The active site pocket of the *Thermus thermophilus* ATP sulfurylase-APS complex is more compact than the active site pocket of *Saccharomyces cerevisiae* and *Penicillium chrysogenum* ATPS-APS complex, indicating adaptation to a hot environment (**Fig. 7**).

The zinc ion is located in the N-terminal half of linker domain, immediately after catalytic domain and is tetrahedrally coordinated by Cys294, Cys297, Cys306, and His310, and could not be removed from the protein by treatment with EDTA. The zinc-binding region appears to be a hinge between catalytic and linker domains and also has been involved in protein-protein interactions.

The linker domain covers the active site of *Thermus thermophilus* ATP sulfurylase and the adenine moiety of bound APS. The distances from the zinc ion to the adenine ring of the bound APS and to His from HXXH motif are 14 and 17 Å, respectively, and zinc is distant from the active site. It has been suggested that Zn^{2+} binding and/or the dimer interaction may contribute to tight active site and to holding the conformation of this region in the correct orientation [87].

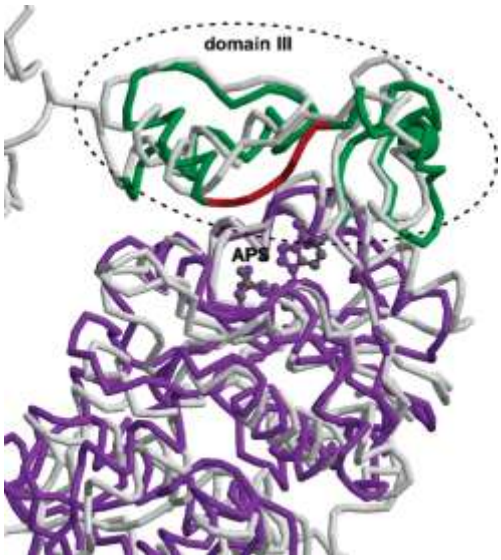

Fig. 7 Comparison of the active sites of ATP sulfurylase from *Thermus thermophilus* HB8 and S*accharomyces cerevisiae.* The ATP sulfurylase of *Sc. cerevisiae* (grey) was superimposed over that of the ATP sulfurylase from *Thermus thermophilus* [domain III (green) and other (purple)]. APS (purple) and zinc (green) are shown as ball-and-stick, respectively [87]

ATP sulfurylase from *Saccharomyces cervisiae* and *Penicillium chrysogenum* are homohexamers and have very similar kinetic properties [67] except for their response to PAPS. In fact, the N-terminal and catalytic domains of the two enzymes (residues 1-395) are 67 % identical in sequence and superimpose with a root mean square deviation (rmsd) of 0.72 Å for

363 equivalent α-carbons. Hovewer, the yeast enzyme is not allosterically inhibited by PAPS because of the lacks of many C-terminal residues responsible for sulfonucleotide binding [50].

The crystal structure of ATP sulfurylase from *Saccharomyces cerevisiae* as substrate-free and product complex (with APS and PP_i bound) have been determined to the resolution of 1.95 Å and 2.6 Å, respectively [70]. The protein crystallizes reproducibly within 2 days from solution containing Cd^{2+} as an additive. The enzyme is a homohexamer with the *D3* symmetric structure, where two trimer rings assemble in a staggered configuration with the twist of 60 ° (**Fig. 8**). Interactions within the hexamer are mediated through hydrogen bonding and salt bridges including a broad system of solvent molecules. A number of cadmium ions also contribute to the formation of the monomer-monomer interfaces.

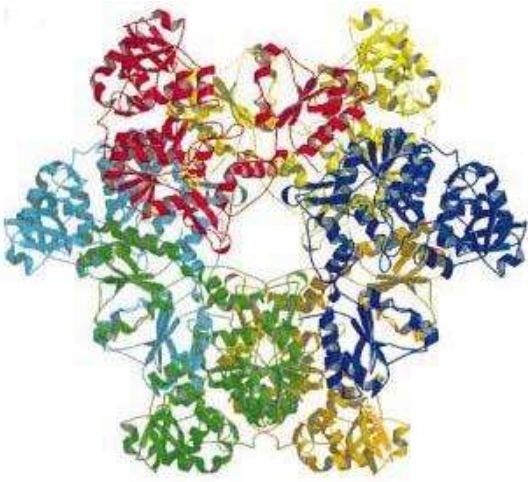

Fig. 8 Hexameric structure of ATPS from *Saccharomyces cerevisiae* [70].

The monomer of *Sc. cerevisiae* is characterized by a high ratio of regular secondary structure elements and can be divided into four domains: the N-terminal, catalytic, linker and C-terminal domains (**Fig. 9**). The N-terminal part of the peptide chain (residues 2-167), comprises a main β-barrel motif formed from five anti-parallel β-strands with several helical insertions, and an additional short β-hairpin motif. The N-terminal and catalytic domains interact mainly through hydrogen bonds and salt bridges.

The catalytic domain (residues 168-327) is composed of both the active site and the substrate binding pocket. A right-handed α, β-fold in three layers (Rossmann-like fold) is typical for nucleotide-binding enzymes. It exhibits distinct features, such as typical fold topologies and an active site design, resembling that of other nucleotidylyl transferase [88]. ATP sulfurylase has the typical HXXH-box and its own finger-print motifs, such as the highly conserved QXRN, GRD, and PFR loops. The catalytic and linker domains are held together mainly by the charged and hydrophilic residues.

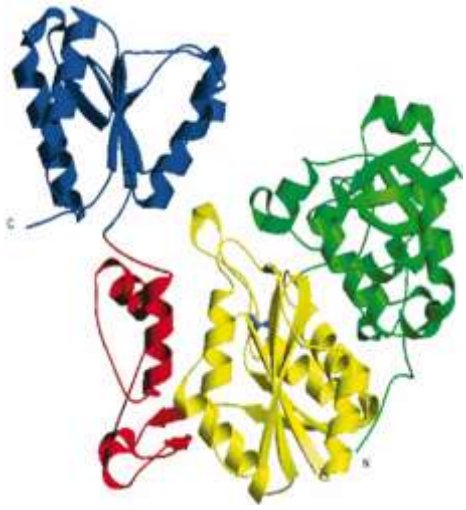

Fig. 9 Ribbon plot of the monomer of yeast ATP sulfurylase. The colour-coding represents the four domains, N-terminal (green), catalytic (gold), linker (red) and C-terminal (blue). The location of the active site is indicated by the binding position of a phosphate ion [70].

The linker domain (residues 328-393) is relatively short and links the C-terminal and catalytic domains. This domain can assist in the formation of the upper section of the ATP sulfurylase substrate binding pocket. The highly conserved PFR motif allows some flexibility when ATP binds to the enzyme. Nucleotide binding causes significant conformational changes, which lead to a rigid-body structural displacement of C-terminal and linker domains towards N-terminal and catalytic domains of the ATP sulfurylase monomer and may serve for substrate recognition.

The C-terminal domain (residues 394-511) displays an α, β-fold with five-twisted parallel β-strands. The C-terminal domain of yeast ATP sulfurylase is structurally quite independent from the rest of the molecule, and not essential for catalytic activity. However, C-terminal domain is intimately involved in the association of three monomers in a trimer ring and also in the association of two of those rings in the mature hexamer. Truncation of this domain results in a monomeric enzyme with slightly enhanced catalytic efficiency [71]. Structural alignment of the C-terminal domain indicates that it is extremely similar in its fold to fungal APS kinase, although not catalytically competent, indicating a potential evolutionary relationship with a bifunctional PAPS synthetase. The ATP sulfurylase structure supports the hypothesis that the primary function of the APS kinase-like domain is to stabilize the oligomeric state of the enzyme.

Yeast ATP sulfurylase (**Fig. 9**) exhibits a sufficiently deep and wide, as well as properly positioned, surface groove that connects the active site of the adenylyltransferase and defunct active site of the APS kinase-like domain. It is tempting to speculate that this groove represents a substrate channel between the ATP sulfurylase and the APS kinase-like domains of the enzyme.

Nucleotide binding causes a significant rigid body displacement within the ATP sulfurylase hexameric assembly. Hovewer, two histidines of the HXXH motif, which bind to α

and β- phosphates of a nucleotide in many nucleotidyl transferases, are located in the ATP sulfurylase product complex far away from the α-phosphorous of the APS, with a distance of 5.7 Å. This suggests that histidines of ATP sulfurylase are not directly involved in the cleavage of α-β-phosphodiester bond, but play a role in pyrophosphate binding and stabilization of a productive ATP conformation.

The structure of ATP sulfurylase from *Saccharomyces cerevisiae* was also solved in a complex with its second substrate ATP. Due to the horseshoe-like conformation of ATP in the pocket, this model allows an ″in-line″ nucleophilic attack of the adjacent sulphate (**Fig. 10**). In support of kinetic data and stereochemical investigations [89] the structural data [70] confirm a substitution mechanism with stereochemical inversion at the α-phosphorus leading directly to the formation of APS, with PP_i as leaving group and without covalent adenylyl-enzyme intermediates. The enzyme provides suitable binding sites for its substrates, ATP and sulphate, that brings the reactive groups in close contact and promotes the stabilization of the nucleotide conformation most favourable for the ″in-line″ attack at the sulphate. During the reaction cycle, it stabilizes the pentavalent transition state of the reactants. As typical for ATP-binding enzymes, a Mg^{2+} ion could coordinate to the β and γ-phosphate groups but has not been identified in the crystal structure.

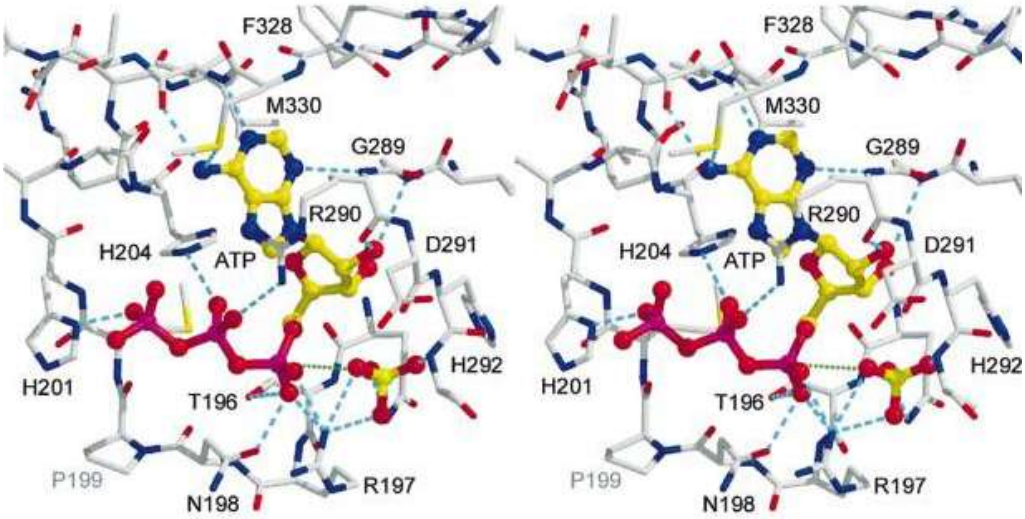

Fig. 10 Stereoview of the active site of ATP sulfurylase with sulfate and a modelled ATP molecule in the typical horseshoe conformation. Hydrogen bonds are shown in cyan; the direction of the nucleophilic attack of the sulfate is marked in green [70].

ATP sulfurylase from *Penicillium chrysogenum* is a homohexameric enzyme that is subject of allosteric inhibition by PAPS (the product of APS kinase). The crystal structures of ATP sulfurylase from *Penicillium chrysogenum* were solved in the presence of either APS or PAPS [69, 90]. Two enzymatic conformations were found for enzyme with substrate and allosteric inhibitor ligation. Substrate-binding conformation was termed ″closed switch″ R-state, while

inhibitor binding conformation was termed ″open switch″ T-state. The termes R and T are commonly thought to abbreviate ″relaxed″ and ″tout″ states of a cooperative enzyme and are actually backward descriptions of the ATP sulfurylase allosteric transition. The X-ray structure shows hexameric organisation of enzyme as a dimer of triads in the shape. Each subunit is divided into a discreet N-terminal domain (residues 1-170), a central catalytic domain (residues 171-395) and a C-terminal allosteric domain (residues 396-573) that is very similar to APS kinase in sequence [67] and structure [91, 92]. However, this regulatory domain has no APS kinase activity because of modifications to the ATP P-loop and the filling of the ATP binding region with protein side chain surrogates (e.g. Phe-548, which fills the space that would otherwise be occupied by the adenine ring of ATP) [68]. Within a given triad, the allosteric domain of one subunit interacts with the catalytic domain of another. Each C-terminal domain interacts across the triad interface with an N-terminal domain, a catalytic domain, and another C-terminal domain, considering the many oligomer-stabilizing interactions of the C-terminal domain [50]. In moving from the high substrate affinity R-state to the low substrate affinity T-state [93-95], the side chain of Arg-515 moves toward PAPS, the allosteric domain of each subunit pivots 27 ° relative to the catalytic and N-terminal domains, and the hexamer expands slightly to the volume (**Fig. 11a**). The T-state active site is in a much open conformation than the R-state (**Fig. 11b**). Thus, the dimensions of the R-state hexamer are 134 Å × 73 Å, the T-state hexamer is dilated to 139 Å × 85 Å [90] The opening of the active site is largely a result of a 17 Å shift in the position of the loop comprising residues 227-237. This loop was termed ″active site switch″ because it is dramatically flipped out of the active site in the T-state structure. Although no portion of this loop comprising directly interacts with the APS product bound to the active site in the R-state structure, Asp234 participates indirectly by forming a salt linkage with Arg199. Amino acid Arg 199 from ^{197}QXRN^{200} active site is strictly conserved in all ATP sulfurylases and binds the phosphosulphate moiety of APS in the R-state and is essential for activity [78, 96]. The PAPS is believed to initiate the allosteric transition by disrupting a salt link between Arg-515 in the C-terminal of one subunit and Asp-111 in the N-terminal domain of a trans-triad subunit [90]. Thus, Asp234 and the flexible loop on which these residues may be considered as ″second layer″ active site residues that do not interact with the substrates directly, but instead function by positioning the substrate-binding or catalytic residues. In moving to the open T-state conformation, the switch coils back on itself and adds one turn to the preceding α-helix. In the R-state, Asp234 orients Arg199 for optimum sulphate (or sulfuryl group) binding (or catalysis). In the T-state, Asp234 stabilizes the open conformation of the active site switch by forming an α-helical N-cap. Rotation about the interface between catalytic-allosteric domains provides the space for the switch to open. It have been suggested that the allosteric effector may

not induce a totally new subunit conformation but rather may exploit the existing flexibility of the enzyme [50]. The major difference between ATP sulfurylase from yeast and *Penicillium chrysogenum* is the C-terminal domain, while the catalytic domains have the same topology.

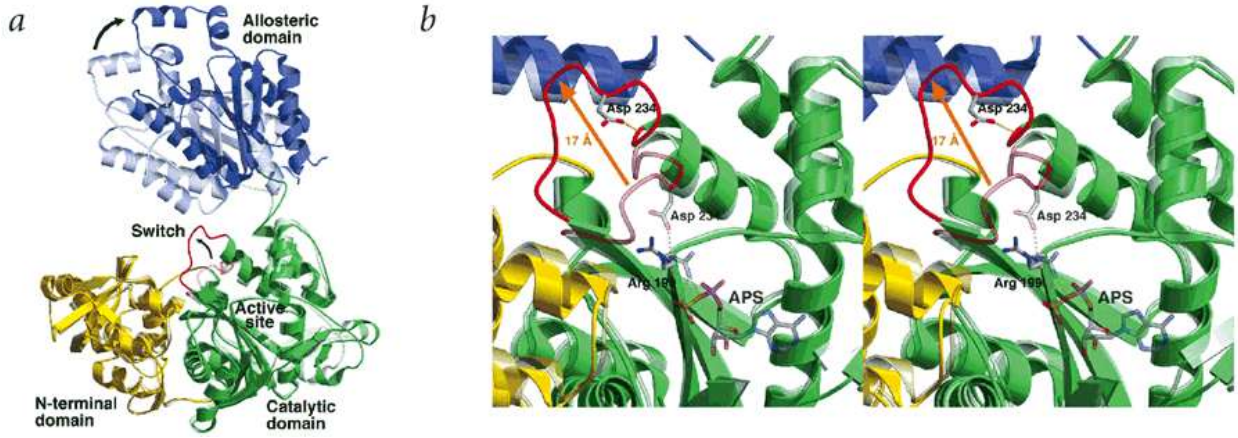

Fig. 10. Conformational changes observed in the R-to-T allosteric transition. ***a***, R- and T-state subunit superimposition. Domains of a single subunit are colored as follows: N-terminal domain (yellow), catalytic domain (green) and allosteric domain (blue). The R-state subunit is shown partially transparent to distinguish it from the T-state. The active site switch (residues 228−238) is red ***b***, Active site switch. The active site region of the T-state structure is shown superimposed on the R-state active site. The R-state structure and bound APS are shown partially transparent to distinguish them from the T-state structure. The active site switch is red [90].

Penicillium chrysogenum ATP sulfurylase missing the C-terminal allosteric domain is catalytically active but it is monomeric and much less stable than the hexameric wild type enzyme. In contrast to the wild type, all k_{cat} values were decreased. Additionally, the Michaelis constants for Mg^{2+}ATP and sulphate (molybdate), the dissociation constant of *E*-APS, and the monovalent oxyanion dissociation constants of dead end *E*-Mg^{2+}ATP- oxyanion complexes were all increased. The cumulating results indicate that besides serving as a receptor for the allosteric inhibitor, the C-terminal domain stabilizing the hexameric structure and indirectly, individual subunits [50].

ATP sulphurylase from *D. desulfuricans* ATCC 27774 ($ATPS_{des}$) was described as Co^{2+}/Zn^{2+}- containing homotrimer with molecular mass of 141 (3 × 47) kDa. The UV-Vis spectra of $ATPS_{des}$ has absorbance maxima at around 279 nm, LMCT bands at 335 and 370 nm, the contribution of d-d bands at 625, 666 and 715 nm. The sequence and EXAFS analyses of the $ATPS_{des}$ reveal that either cobalt or zinc ions is tetrahedrally coordinated presumably equivalent metal-binding site by the nitrogen and three sulphur atoms in the motif $^{349}Cys\text{-}X_2\text{-}Cys\text{-}X_8\text{-}Cys\text{-}X\text{-}His$ [27, 97].

The objectives of this work were:

1. To develop methods for the production *in vivo* of fully cobalt- zinc- and iron-substituted forms of recombinant adenylate kinase from *D. gigas* overexpressed in *E. coli.*

2. To develop methods for crystallization of Co^{2+}, Zn^{2+} and Fe^{2+}-AK_{gig} and Co^{2+}/Zn^{2+}-$ATPS_{des}$ enzymes and resolve their structures.

3. To determine the role of the three metal ions (Co^{2+}, Zn^{2+} and Fe^{2+}) in the LID domain of adenylate kinase from *D. gigas* by different biochemical and biophysical tecniques. To study the mechanism of thermal denaturation of holo-AK_{gig} and role of these metals to the stability and activity of these proteins.

4. To determine structural stability and mechanism of thermal unfolding of $ATPS_{des}$.

Chapter 2

Zinc-, cobalt- and iron-chelated forms of adenylate kinase from the Gram-negative bacterium *Desulfovibrio gigas.*

This chapter was published as:

Anna V. Kladova, Olga Yu. Gavel, Galina G. Zhadan, Valery L. Shnyrov, Sergey A. Bursakov. 2009 Zinc-, cobalt- and iron-chelated forms of adenylate kinase from the Gram-negative bacterium *Desulfovibrio gigas.* International Journal of Biological Macromolecules 45(5):524-31.

Abstract

Adenylate kinase from the sulphate-reducing bacterium *Desulfovibrio gigas* (AK_{gig}) has been characterized earlier as a Co^{2+}/Zn^{2+}-containing enzyme that is an unusual characteristic for adenylate kinases from Gram-negative bacteria, in which these enzymes are normally devoid of metal ions. AK_{gig} was overexpressed in *E. coli* and homogeneous Co^{2+}-, Zn^{2+}- and Fe^{2+}-forms of the enzyme were obtained under *in vivo* conditions. Their structural stability, spectroscopic and kinetic properties were compared. The thermal denaturation of Co^{2+}- and Zn^{2+}-forms of AK_{gig} was studied as a cooperative two-state process, sufficiently reversible at pH 10, which can be correctly interpreted in terms of a simple two-state thermodynamic model. In contrast, the thermally induced denaturation of Fe^{2+}-AK_{gig} is irreversible and strongly dependent upon the scan rate, suggesting that this process is under kinetic control. Practically identical contents of secondary-structure elements were found for all the metal-chelated-forms of AK_{gig} upon analysis of circular dichroism data, while their tertiary structures were significantly different. The peculiar tertiary structure of Fe^{2+}-AK_{gig}, in contrast to Co^{2+}- and Zn^{2+}-AK_{gig}, and the consequent changes in the physico-chemical and enzymatic properties of the enzyme are discussed.

Introduction

Adenylate kinase (AK, ATP:AMP phosphotransferase, EC 2.7.4.3), a member of the nucleoside monophosphate kinase family, is a small monomeric protein that mediates the reversible transfer of phosphate groups between adenine nucleotides, which are the main substrates, co-factors, or allosteric effectors in a series of key metabolic reactions [7].

Like many nucleotide-binding proteins, AK belongs to the α/β class, with a five-stranded β-sheet surrounded by several α-helices [98]. The formation of the ternary complex stabilizes the enzyme in a form where the mobile small LID and AMP-binding sub-domains close over the remaining CORE region. This rearrangement of the two mobile sub-domains is necessary for the accommodation of the nucleotides in an optimal catalytic geometry, and the resulting closed enzyme conformation provides a solvent-free environment for phosphoryl transfer [18].

Generally, the AK from Gram-positive bacteria contain a Cys-X_2-Cys-X_{16}-Cys-X_2-Cys/Asp structural motif in the LID domain that is responsible for the binding of zinc ion [13, 20, 22], whereas the AK from Gram-negative bacteria are usually devoid of metal ions, since their Cys residues are substituted by another four highly conserved amino acids - His, Ser, Asp and Thr, respectively [23]. Nevertheless, exceptions are the AK from *Desulfovibrio gigas* and *Desulfovibrio desulfuricans* ATCC 24774, which contain either cobalt or zinc [24], the AK from *Paracoccus denitrificans*, overproduced in *E. coli* [15], which binds either zinc or iron, and the AK from *Chlamidia pneumoniae* and *Thermotoga neapolitana*, which contain zinc [25, 26]. Thus, to date three different metal ions -zinc, cobalt and iron- have been found to be present in the AK from a few Gram-negative bacteria.

Besides the somewhat rare presence of metal ions in the AK of several Gram-negative bacteria, attention has to be focused on the varieties of the metal-binding centres (Cys-$X_{2\div5}$-Cys/His-X_{14-19}-Cys-X_2-Cys/Asp) involved in different organisms [24] whose specific properties may be involved in metal selection.

Metal ions play a variety of roles in natural proteins, including nucleophilic catalysis, electron transfer, and the stabilization of protein structure. They also play a structural role in AK, as confirmed in several crystallographic studies [19, 20, 37]. Mutations in the LID domain lead to considerable differences in the overall stability of AK [23, 99, 100]. Zinc binding at the genetically engineered zinc-chelating site of *E. coli* AK affords the microorganism considerably higher thermal stability, with a T_m value of 61.6 °C *versus* 52.5 °C for the AK from the wild-type, with hydrogen bonding in the LID domain [23, 100]. Previous studies have also shown that zinc depletion reduces the T_m value of *D. gigas* by 5.3 °C [28]; that of *T. neapolitana* by 6.3 °C, and that of *Geobacillus Bacillus stearothermophilus* by 7.5 ºC [26, 29].

A method for the production chimeras by exchange of certain parts of thermophilic and mesophilic organisms has been applied to confirm their main responsibilities as regards the activity and stability of AK [30]. This, together with mutagenesis studies, has shown that the CORE of AK is responsible for the structural stability, while dynamics of the LID and AMP_{bind} domains have been suggested to be related to catalysis [18, 30, 37, 101]. DSC results show that the stabilities of the mesophilic and thermophilic AMP_{bind} and LID domains are similar, and hence their overall stabilities are limited by the stabilities of their CORE domains. Additionally, the results of activity assays clearly show that the two mobile domains themselves (the AMP_{bind} and LID domains) may control their own functional dynamics and may cause differences in activity. Bae and Phillips confirmed their suggestion that AK catalysis is regulated by the intrinsic properties of the moving domains [30].

Knowledge of structural stability and functional activity is important for understanding the binding mode and the putative role of different metal ions in AK. Thus, in the present work we describe a detailed investigation of the thermal stability of homogeneous Co^{2+}-, Fe^{2+}- and Zn^{2+}-forms of AK_{gig}, using different independent methods such as differential scanning calorimetry (DSC), UV-Vis-spectroscopy, circular dichroism (CD) and kinetic assays.

Materials and methods

Materials.

The reagents hexokinase, pyruvate kinase, lactate dehydrogenase, phosphoenolpyruvate, $NADP^+$, NADH, AMP, ADP, MgATP were from Sigma. Glucose-6-phosphate dehydrogenase was from Merck.

Gene Cloning and Expression Screening.

The gene coding for the AK of *D. gigas* (672-bp DNA fragment) (EMBL Nucleotide Sequence Database accession number FN424087) was amplified (annealing temperature 64 ºC) from *D. gigas* genomic DNA by polymerase chain reaction (PCR) with the appropriate upstream primer 5'-GGGGCTCGAGCA/TATGAACATCCTGATCTTCGGTCCGAACGGC-3' and the downstream primer 5'-CCCCGGATCCA/AGCTTTTAGGCAAGCTGGGCCAG-3'. The PCR fragments containing upstream *NdeI* and downstream *HindIII* restriction sites were cloned into the pMOS*Blue* vector (GE Healthcare) and the nucleotide sequence of the PCR product was verified by DNA sequencing. The *NdeI* and *HindIII* digestion product of the DNA fragment was then cloned into the expression vector pET-22b(+) (Novagen). The resulting plasmid pET-22b(+)/AK with the gene inserted was used for protein expression in *E. coli* strain BL-21(DE3) (Stratagene).

Protein Production.

Translation of the insert gene induced in mid-log phase ($A_{660\ nm} \approx 0.6 – 0.7$) by the addition of 1 mM isopropyl 1-thio-β-D-galactopyranoside (IPTG) to minimal M63B1 medium (0.1 M KH_2PO_4, 15 mM $(NH_4)_2SO_4$, 0.8 mM $MgSO_4$, 3 µM vitamin B_1, pH 7.4) supplemented with 0.4 % glucose [16] at 37 °C with vigorous shaking for 4 – 6 h depends on the type of AK to be expressed. The incubation temperature and the metal concentration in the medium were optimized in order to obtain homogeneous protein with a single metal. Typically, cells were grown in 1 L of M63B1 medium containing 100 µg/ml of ampicillin and the expression conditions were as follows: for Co^{2+}-AK_{gig}, 6 h and minimal medium supplemented with 160 µM $CoCl_2$; for Zn^{2+}-AK_{gig}, 4 h and 250 µM $ZnCl_2$; for Fe^{2+}-AK_{gig} - 4 h and 130 µM $FeCl_2$ at 37 °C.

After these incubation periods, cells were harvested by centrifugation at 5000 rpm for 30 minutes at 4 °C. Then, cells were resuspended in 20 mM Tris-HCl, pH 7.6, at a ratio of 1:4 (w/v), and disrupted by passing them through an EmusTex-C5 Homogenizer at 9000 psi. Phenylmethylsulphonyl fluoride (PMSF) at 1 mM concentration was added to the broken cells fraction as an inhibitor of serine proteases. The extract was centrifuged at 125000 g for 90 min at 4 ºC and the pellet was discarded. A clear supernatant containing the soluble fraction was then used for the purification of AK; it was processed immediately to avoid protein degradation.

Purification of recombinant AK from E. coli.

The AK of *D. gigas* overexpressed in *E. coli* was purified as described earlier [24, 102] in a two-step FPLC (Pharmacia) procedure on Blue Sepharose (Cibacron Blue 3G-A Sepharose CL-6B) fast flow and Superdex-75 gel filtration columns at 4 ºC. After the second column, the protein was eluted in 50 mM Tris/HCl buffer, pH 7.6, and 250 mM NaCl, after which it was concentrated, dialyzed, and kept frozen at -20 °C. The protein concentration was determined with the Bicinchoninic Acid Protein Assay Kit from Sigma.

Determination of protein purity and metal analysis.

Protein purity was determined by SDS-PAGE at 12.5 % (w/v), as described by Laemmli [103], in each purification step. The molecular mass standards from Bio-Rad were myosin (200 kDa), β-galactosidase (116.3 kDa), phosphorylase b (97.4 kDa), bovine serum albumin (66.2 kDa), ovalbumin (45 kDa), carbonic anhydrase (31 kDa), soybean trypsin inhibitor (21.5 kDa), lysozyme (14.4 kDa) and aprotinin (6.5 kDa). Protein staining was performed using R-250 Coomassie blue.

The quantification of metals was performed by ICP-AES analysis (Inductively Coupled Plasma-Atomic Emission Spectroscopy) on a Horiba Jobin-Yuon apparatus, model Ultima. Standard solutions containing cobalt, iron and zinc were supplied by Aldrich.

Measurement of the velocity of the forward reaction (AMP and MgATP as the substrates).

Measurement of the velocity of the forward reaction was performed by monitoring the oxidation of NADH at 340 nm by coupling with pyruvate kinase (PK) and lactate dehydrogenase (LDH). The reaction mixture contained 50 mM Tris-HCl, pH 7.6, 100 mM KCl, 0.25 mM $MgCl_2$, 0.2 mM NADH, 1 mM PEP, 15.5 U/ml of LDH and 25 U/ml of PK. The concentrations of AMP and MgATP were varied for the specific requirements of each experiment. The reaction was started by adding 30-50 ng of AK. One unit (U) is defined as 1 μmol of ADP (MgADP) generated per minute.

The rate of the backward reaction (MgADP and ADP as substrates).

The rate of the backward reaction was measured by following the reduction of $NADP^+$ at 340 nm in an enzyme solution coupled with hexokinase and glucose-6-phosphate dehydrogenase. The reaction mixture contained 50 mM Tris-HCl, pH 7.6, 100 mM KCl, 1 mM glucose, 8 mM $NADP^+$, 5 U of hexokinase, and 5 U of glucose-6-phosphate dehydrogenase. The concentrations of ADP and $MgCl_2$ were varied for the individual needs of each experiment. The reaction was started by adding 30-50 ng of AK. One unit is defined as 1 μmol of ATP generated per minute.

End-point kinetic assay (optimum temperature).

AK_{gig} (90 ng/ml) was incubated over a broad temperature range (4 °C - 40 °C) for 3 min in a buffer (total volume 280 μl) containing 100 mM $NaHCO_3$/NaOH, pH 10.0, and 10 mM MgATP, AMP and $MgCl_2$. The reactions were stopped by the addition of 1 ml of 1.2 M perchloric acid, kept on ice and centrifuged at 25000 g for 5 min. An 800-μl aliquot of the supernatant was neutralized with 350 μl of 2 M KOH in 230 mM Tris-HCl, pH 7.6. The mixture was centrifuged at 25000 g for 5 min and the 200 μl aliquot was used for ADP determination. The reaction mixture (total volume 1ml) contained 50 mM Tris/HCl buffer, pH 7.6, 2 mM $MgCl_2$, 100 mM KCl, 1 mM PEP, and 0.3 mM NADH. The reaction was started by adding 7.8 U of LDH and 12.5 U of PK. The samples were monitored at 340 nm for NADH oxidation. Blanks were obtained for each temperature point.

Differential scanning calorimetry.

Calorimetric scans were performed on a MicroCal MC-2D differential scanning microcalorimeter (MicroCal Inc., Northampton, MA) with cell volumes of 1.22 ml, as described previously [24, 104]. All solutions were degassed by stirring under a vacuum prior to scanning. An overpressure of 2 atm. of dry nitrogen was kept over the liquids in the cells throughout the scans. The reversibility of the thermal transitions was checked by examining the reproducibility of the calorimetric trace in a second heating of the sample immediately after cooling from the first scan. The molar excess heat capacity curves obtained by normalization with the protein concentrations and volume of the calorimeter cell were smoothed and plotted using the Windows-based software package (ORIGIN) supplied by MicroCal. Data analysis was

accomplished on the basis of the two limiting cases of Lumry-Eyring [105] model; namely, the two-state equilibrium folding/unfolding model ($N \overset{K}{\leftrightarrow} D$), where only the native (N) and denatured (D) states of the protein are significantly populated and their relative amounts at a given temperature are determined by the value of the equilibrium constant (*K*), and a simple two-state irreversible model ($N \overset{k}{\rightarrow} F$), in which only the native state (N) and the irreversibly denatured state (the final state: F) of the protein are significantly populated and where *k* is the first-order rate constant that changes with temperature according to the Arrhenius equation.

Circular dichroism.

The CD spectra of AK were recorded on a Jasco-715 spectropolarimeter, using a spectral band-pass of 2 nm and cell pathlengths of 1 mm in the far-ultraviolet range (195-250 nm) and of 10 mm in the near-ultraviolet range (250-320 nm). In these measurements, protein concentrations of ca. 0.1 and ca. 1 mg/ml were used, respectively. Four spectra were scanned for each sample at a scan rate of 20 nm/min and were then averaged. All spectra were background-corrected, smoothed, and converted to mean residue ellipticity $[\Theta] = 10\ M_{res}\ \Theta_{obs}\ l^{-1}\ p^{-1}$), where M_{res} is the mean residue molar mass; Θ_{obs} is the ellipticity (degrees) measured at wavelength λ; *l* is the optical pathlength of the cell (dm), and *p* is the protein concentration (mg ml^{-1}). Secondary structure analysis of the CD spectra in the far-ultraviolet range was performed using the CDPro software package [106].

Results and Discussion

Protein expression and purification.

We found that the type of growth medium and concentration of the metal in it have a considerable influence on the presence of the respective metal in AK. Several previous publications have reported reduced numbers of metal equivalents in AK from different sources [107]. Because complete metal occupation was a major aim in this work, the selection conditions for protein production were chosen based on the quantity of the only metal present at the binding centre. Thus, the best induction conditions for AK expression were established, as described in Materials and Methods. The yield of AK varied, depending on the type of metal supplied to the medium, and was ~3.5 mg of protein from 1 L of culture for Co^{2+}-AK, and ~9 mg of protein for the Zn^{2+}-AK and Fe^{2+}-AK forms. Metal determination in the Co^{2+}-AK_{gig}, Zn^{2+}-AK_{gig} and Fe^{2+}-AK_{gig} forms afforded a metal-to-protein ratio of approximately 1:1. The purity of the ~24.7 kDa AK along the purification steps determined by SDS-PAGE is shown in **Fig.1**.

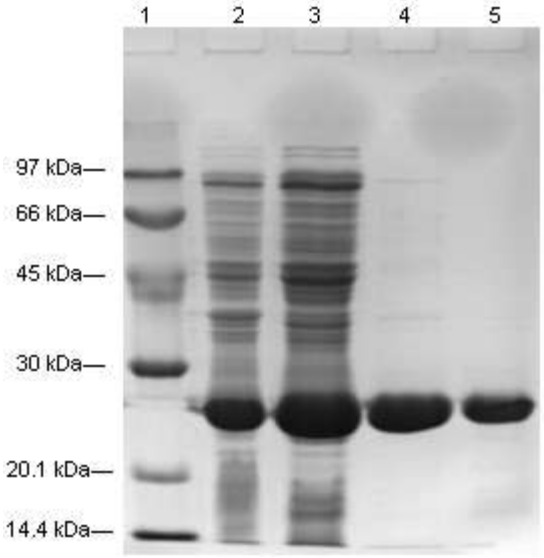

Fig. 1. **Gel-electrophoresis in all the purification steps of AK.** 1-LMW standard; 2-broken cells; 3-soluble fraction; 4- fraction after Blue Sepharose column; 5- fraction after Superdex-75 column.

Sequencing of the N-terminus MNILIFGPNGSGKGTQGNLVKDKYSLAHIE confirmed that the recombinant protein was identical to the AK from *D. gigas*.

UV-Vis spectra.

Co^{2+}-AK_{gig} is blue in colour and exhibits five maxima (**Fig. 2**) at 275, 340, 610, 650 and 690 nm (ε_{340} = 3250 $M^{-1}cm^{-1}$, ε_{605} = 547 $M^{-1}cm^{-1}$ ε_{650} = 830 $M^{-1}cm^{-1}$, ε_{690} = 950 $M^{-1}cm^{-1}$), in good agreement with the UV-Vis spectra of the native form of AK [24]. The peak at 340 nm corresponds to the $S^- \rightarrow Co^{2+}$ ligand-to-metal charge transfer (LMCT) band. Its value is related to the number of thiolate groups coordinated to the metal [108], and ranges from 900 to 1300 $M^{-1}cm^{-1}$ per $S^- \rightarrow Co^{2+}$ bond. Thus, for Co(II)-rubredoxin and Co(II)-thermolysin the charge-transfer band is generated at 350 nm, with $\varepsilon \approx 1200$ $M^{-1}cm^{-1}$ per bond [109] and 340 nm with $\varepsilon \approx$ 900 $M^{-1}cm^{-1}$ per bond [110], respectively. The presence of His in the cobalt-binding motif must shift this peak to higher energies (shorter wavelength). In the CoS_4, CoS_3N, CoS_2N_2 and $CoSN_3$ series, the wavelengths of the absorption maxima decrease steadily [108]. Cobalt (II) exhibits d-d absorption in the visible region at 610, 650 and 690 nm, which clearly confirm that cobalt is in tetrahedral coordination, with three sulphur atoms and one nitrogen atom.

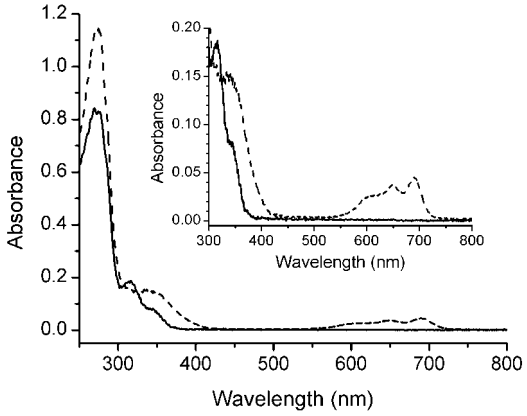

Fig. 2. Electronic absorption spectra of Fe^{2+}-AK (dashed line) (31 μM) and Co^{2+}-AK (solid line) (41 μM) in 50 mM Tris-HCl buffer pH 7.4.

Fe^{2+}-AK_{gig} exhibits three maxima at 275, 311 and 344 nm (ε_{311} = 5270 $M^{-1}cm^{-1}$, ε_{345} = 2390 $M^{-1}cm^{-1}$) (**Fig. 2**). The band at 311 nm and shoulder at 340 nm are due to the $S^- \rightarrow Fe^{2+}$ charge transfer, in good agreement with the UV-Vis spectrum of Fe^{2+}-AK from *Paracoccus denitrificans* [15].

The UV-Vis spectrum of Zn^{2+}-AK_{gig} exhibits a maximum at 275 nm. Zinc provides the LMCT band with sulphur atoms at 275 nm [111], which is hidden by the absorption of aromatic amino acid residues of the protein.

Kinetic parameters.

The kinetic properties of recombinant holo-forms of AK are shown in Table 1. Metal-chelated forms of AK_{gig} have much higher affinity for the substrates of the forward reaction with higher V_{max} values than those of the backward reaction. Similar differences between the V_{max} values of the forward and backward reactions have been reported for the AK from *E. coli* and yeast extract, while for the AK from *P. denitrificans* they are comparable [16].

Table 1. Comparative kinetic parameters of metal-chelated forms of AK_{gig}.[1]

protein	K_m(AMP), μM	K_m(MgATP), μM	V_{max} (AMP, MgATP), μmol/(min·mg)	K_m(ADP), μM	V_{max} (ADP) μmol/(min·mg)
Zn^{2+}-AK	46 ± 4	34 ± 3	1335	165 ± 25	980
Co^{2+}-AK	40 ± 4	49 ± 4	1310	247 ± 30	730
Fe^{2+}-AK	71 ± 4	76 ± 4	1220	128 ± 20	690

K_m (ADP) and V_{max} (ADP) were calculated according to the assumption that two molecules of ADP bind to the enzyme with the same affinity. The K_m for AMP and MgATP was determined at a single fixed concentration of co-substrates (50 μM).

[1]

The presence of metal ions in the LID domain affects the kinetic properties of AK_{gig}. Thus, the magnitude of K_m(AMP) and K_m(MgATP) of the forward reaction could be depicted in the following order: Fe^{2+}-AK_{gig}> Co^{2+}-AK_{gig}≈ Zn^{2+}-AK_{gig}, with very similar V_{max} values. The K_m(AMP) and K_m(MgATP) values are very similar within each holo-form. The kinetic parameters of Co^{2+}/Zn^{2+}-AK_{gig} for the forward reaction are very similar to those reported for AK_{col} [16, 23].

The K_m(ADP, MgADP) values for the backward reaction could be represented in the following order Co^{2+}-AK_{gig}>Zn^{2+}-AK_{gig}>Fe^{2+}-AK_{gig}. Thus, the iron form of AK_{gig} has the highest K_m values (or the lowest affinity) to the substrates of the forward reaction (MgATP and AMP) and the lowest ones for the substrates of the backward reaction (MgADP and ADP) as compared to the other two holo-forms.

Optimum temperature.

The CORE domain governs overall stability [13], but the issue is how the presence of metal, and its type, in the LID domain of the enzyme, might be responsible for the temperature dependence of the catalytic activity. The disparity in the optimal temperatures of Co^{2+}-, Fe^{2+}- and Zn^{2+}-AK_{gig} for their AK activity is shown in **Fig. 3**. All three temperature profiles have similar shapes, with maxima at 32 °C for Fe^{2+}-AK_{gig}, and 36 °C for Co^{2+}- and Zn^{2+}-AK_{gig}. Despite the relatively small difference in catalytic efficiency between the metal-containing forms, the results of this assay clearly show that the type of the metal in the LID mobile domain to some extent controls the temperature dependence of the catalytic activity.

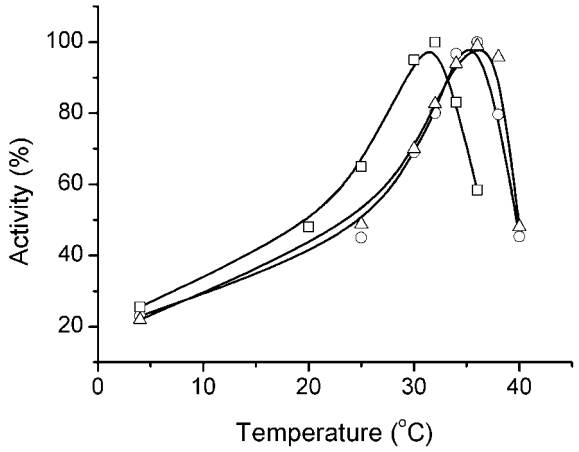

Fig. 3. Temperature dependence of the metal-chelated forms of AK from *D. gigas*: Co^{2+}-AK (circles), Fe^{2+}-AK (squares), Zn^{2+}-AK (triangles).

The differences in the kinetic properties of the holo-forms of AK studied can probably be explained in terms of the fact that LID-CORE hinges show dynamics related to LID movements

in catalysis [26, 112], where the opening of the AMP binding and LID domains is the rate limiting step Moreover, the capacity for self-control of functional dynamics by the LID domain itself [30] should also be taken into account. Together, all these aspects could lead to differences in the activities and optimum temperature of the forms studied.

Circular dichroism.

CD spectra in the far- and near-UV regions were studied with a view to detecting any differences in the secondary and tertiary structures of overexpressed metal-chelated forms of AK_{gig}.

A detailed secondary structure analysis of the far-UV CD spectra (**Fig. 4**) was performed using the CDPro software package [106]. The experimental data in the 185-240 nm range were subjected to treatment by three programs included in this software package, SELCON3, CDSSTR, and CONTINLL, using the SP43 reference set. The markedly lower root-mean-square deviation (rmsd) between the experimental data and the theoretical curves produced by the programs with this reference set was obtained with CONTINLL, and hence the results obtained with SELCON3 and CDSSTR were omitted. The results of this analysis (**Table 2**) show that the secondary structural elements of all the metal-chelated forms of AK_{gig} expressed are practically equal, but slightly differ from the native Co^{2+}/Zn^{2+}-AK_{gig} [28], which can be attributed to experimental error. Analysis of the secondary structure based on the method of cluster analysis [113] with the CLUSTER program included in the CDPro software package permits the AK_{gig} to be attributed to proteins of the α/β class.

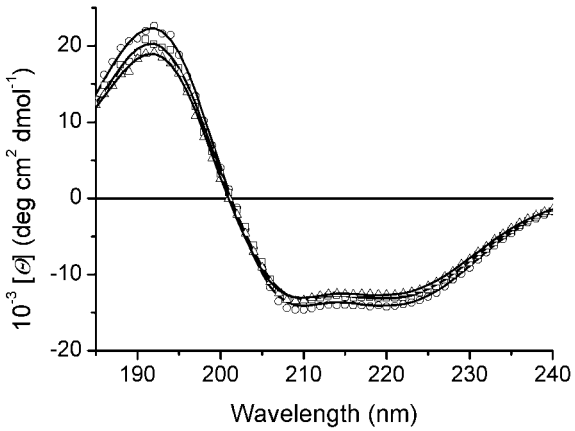

Fig. 4. Far-UV CD spectra of intact Co^{2+}- AK_{gig} (circles), Fe^{2+}- AK_{gig} (squares) and Zn^{2+} AK_{gig} (triangles) at pH 10 and a protein concentration of ~ 4 μM. The solid lines through the symbols are the best fit to the experimental data with the CONTINLL program, using SP43 as a reference set.

Table 2. Secondary structure elements (%) determined from analyses of CD spectra for holo-forms of AK_{gig} at pH 10.0.

	Secondary structure fractions (%)								α-Helical segments		β-Strand segments	
	α-Helices			β-Strands					N	L	N	L
Protein	Regular	Distorted	Total	Regular	Distorted	Total	β-Turns	Unordered	α	α	β	β
Co^{2+}-AK	22	16	38	8	7	15	20	27	8.7	9.6	7.6	4.3
Fe^{2+}-AK	22	15	37	8	7	15	19	29	8.6	9.6	8.4	4.0
Zn^{2+}-AK	21	16	37	8	7	15	19	29	8.8	9.4	8.1	4.0

The numbers (N) and average lengths (L) of α-helix (α) and β-strand (β) are given

The near-UV CD of proteins arises from the environments of aromatic amino acid side chains. Each aromatic amino acid develops a characteristic wavelength profile; thus, tryptophan has a peak between 280 and 300 nm; tyrosine has a peak between 270 and 290 nm, and phenylalanine has a sharp fine structure between 250 and 270 nm. Although the near-UV CD spectra of proteins are not readily amenable for detailed interpretation in terms of tertiary structural features [114] they can provide very useful fingerprints for comparisons of tertiary structures among related proteins.

In contrast to those obtained in the far-UV region, the near-UV CD spectra of all holo-forms of overexpressed AK_{gig} are markedly different (**Fig. 5**). In all the holo-AK_{gig} studied, the contributions of phenylalanine and tryptophan residues are almost the same, while the contribution of tyrosine residues is very different. Thus, for the Co^{2+}-form of AK_{gig} the negative minimum is observed at 278-280 nm; for the Zn^{2+}-form this band is red-shifted to 282 nm, and finally for the Fe^{2+}-form this band displays a strong red shift to the 285-286 nm region, with two-fold amplitude. The contributions of tryptophan and phenylalanine residues show no shifts, regardless of the type of the metal. Thus, the band arising from the tryptophan residue at 293-294 nm is almost equal for all these forms, where amplitude is the highest for the Co^{2+}-form and the lowest for the Fe^{2+}-form. The Fe^{2+}-AK_{gig} also has bands that can be attributed to the presence of iron (314, 328 and 349 nm), while the Co^{2+}-AK_{gig} has bands at 336, 356, 390 and 694 nm due to the presence of cobalt.

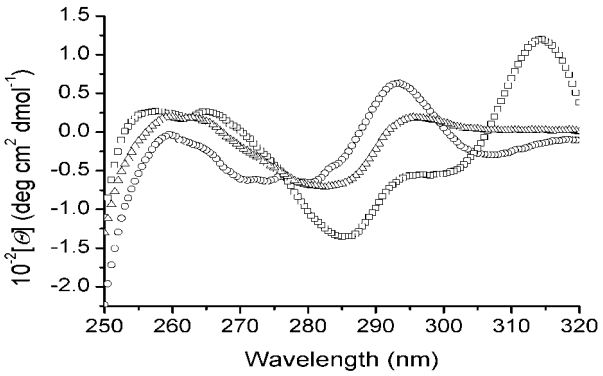

Fig. 5. Near-UV CD spectra of Co^{2+}-AK_{gig} (circles), Fe^{2+}-AK_{gig} (squares), Zn^{2+}-AK_{gig} (triangles) at pH 10 and a protein concentration of ~ 40 μM.

According to these results, the CD spectra in the near-UV region of Co- and Zn^{2+}-AK_{gig} show a similar organization of tertiary structures, while Fe^{2+}-AK_{gig} differs in this organization.

Differential scanning calorimetry.

Figure 6 shows the temperature dependence of the excess molar heat capacity of the cobalt and zinc forms of AK_{gig} in 100 mM $NaHCO_3$/NaOH buffer at pH 10. This pH value was not chosen randomly, since at this pH AK exhibits maximum reversibility, permitting analysis of its denaturation via thermodynamic models [28]. The fitting of the experimental data to the simplest two-state unfolding model afforded excellent results (see lines through the data points in **Fig. 6**). The highest-likelihood values for the thermodynamic parameters obtained from the fittings are shown in **Table 3**.

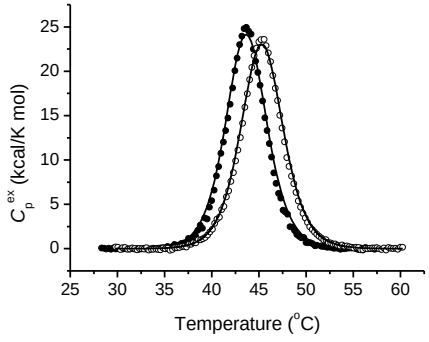

Fig. 6. Temperature dependence of the excess molar heat capacity of Co^{2+}-AK_{gig} (solid circles) and Zn^{2+}-AK_{gig} (open circles) in 100 mM $NaHCO_3$/NaOH buffer, pH 10. The scan rate was 1 K/min. Solid lines represent the best fits of the experimental data to the two-state equilibrium model as implemented in the Origin software package. The enzyme concentration was ~ 30 μM.

Table 3. Parameters characterizing the thermal denaturation of AK_{gig} at pH 10.0[2].

AK	T_m (^oC)	ΔH (T_m) (kcal/mol)	ΔG(25^oC) (kcal/mol)	T_s (^oC)	ΔG(T_s) (kcal/mol)
Zn^{2+}-AK	45.3	134.8	7.3	-15.4	13.3
Co^{2+}-AK	43.7	137.1	7.0	-17.9	13.8
Fe^{2+}-AK	45.0	127.8	6.8	-12.9	12.0

[2] The standard deviation for T_m values is ±0.2 K; the enthalpy of the denaturation was determined with a standard deviation of ±5%; free energy change for AK denaturation at any temperature was calculated, using the modified Gibbs-Helmholtz equation: $\Delta G(T) = \Delta H(T_m)\,(1 - T/T_m) - \Delta C_p\,[(T_m - T) + T\ln(T/T_m)]$; $\Delta C_p = 2.0 \pm 0.2$ kcal K^{-1} mol^{-1} was obtained from the difference in heat capacity between the native and denatured states of the protein at the transition mid point and T_s, the temperature of maximum stability, was calculated with equation: $T_s = T_m \exp[-\Delta H(T_m)/(T_m\,\Delta C_p)]$ [115]. T_m and $\Delta H(T_m)$ values for Fe^{2+}-form of AK were obtained upon extrapolation of the transition parameters to the infinitive heating rate [116-118].

The iron-form of AK_{gig} exhibits different properties. Judging from the absence of the transition upon rescanning the sample, the thermal denaturation of this form of AK would be completely irreversible. **Fig. 7** shows the corrected calorimetric traces for Fe^{2+}-AK_{gig} in 100 mM $NaHCO_3$/NaOH buffer, pH 10.0, at three different scan-rates. It is evident from this figure that T_m is dependent upon the scan-rate and that the transition peaks are skewed toward the low-temperature side of the transition, as expected for a transition under kinetic control.

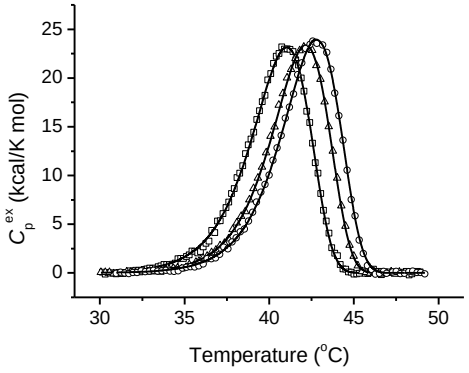

Fig. 7. Temperature dependence of the excess molar heat capacity of Fe^{2+}-AK_{gig} at scan rates of 0.5 K/min (squares), 1 K/min (triangles), and 1.46 K/min (circles) in 100 mM $NaHCO_3$/NaOH buffer, pH 10. Solid lines represent the best fit to each experimental curve using **Eq. 1**. The enzyme concentration was 28 μM.

Irreversibility in protein denaturation typically results from accompanying side processes, such as autolysis, chemical alteration of residues, or aggregation [119], which lock the protein in a final state, after which it is unable to fold back to the native structure; this hampers equilibrium thermodynamic analysis. In this case, the DSC data must be interpreted using kinetic models to determine the parameters of the denaturation and their temperature-dependence. The realistic model of protein denaturation in this case would include two steps: reversible unfolding and irreversible alteration of the unfolded state to produce the final denatured state. This scheme,

usually known as the Lumry-Eyring model [105] in the case of monomeric proteins, can be depicted as $N \underset{k_{-1}}{\overset{k_1}{\leftrightarrow}} U \xrightarrow{k_d} F$, where *N*, *U* and *F* are native, partially unfolded, and denatured protein forms, respectively, and k_1, k_{-1} and k_d are the rate constants for the corresponding reactions. However, use of the complete Lumry-Eyring model for quantitative description of thermally induced transitions is difficult because the corresponding system of differential equations does not have an analytical solution at varying temperatures. It is therefore necessary to evaluate simpler mathematical models that are particular cases of the complete Lumry-Eyring model. In the present work, we used the model that includes only one irreversible step, assuming that protein denaturation is rapid in comparison with the process of partial unfolding, i.e. $k_d \gg k_1$ and $k_d \gg k_{-1}$. This means that, kinetically, the thermally induced denaturation follows the "all-or-not" law: $N \xrightarrow{k} F$. The excess heat capacity functions obtained for Fe^{2+}-AK_{gig} in this case were analyzed by non-linear least-squares, fitting the data to the equation:

, (1)

where $\nu = dT/dt$ (K min^{-1}) is a scan-rate value; ΔH is the difference in enthalpy between the denatured and native states; E_A is the activation energy of the denaturation process; *R* is a general gas constant, and T^* is the temperature at which *k* is equal to 1 min^{-1}, either individually or globally, using the scan rate as an additional variable. The results of the fitting are shown in **Fig. 7** (solid lines) and Table 4. As can be seen, when fitting was carried out both separately on the individual experimental curves and simultaneously on all the curves, a good approximation was achieved. Attempts to include different irreversible models for Fe^{2+}-AK_{gig} denaturation - the Lumry-Eyring model, with a fast equilibrating first step, and the model that includes two consecutive irreversible steps [120, 121] - did not improve the goodness of fit, indicating that the two-state irreversible model is sufficient to quantitatively describe the kinetics of Fe^{2+}-AK_{gig} denaturation.

Table 4. Arrhenius equation parameter estimates for the two-state irreversible model of the thermal denaturation of Fe^{2+}-AK_{gig} at pH 10.

Parameter	Temperature scan rate (K/min)			
	0.5	1.0	1.46	Global fitting
ΔH, kcal/mol	106.5	108.5	110.1	
T^*, ^oC	43.2	43.1	43.1	43.1
E_A, kcal/mol	114.9	118.3	116.7	117.0
r	0.9996	0.9997	0.9997	0.9994

The correlation coefficient (r) was calculated as  , where y_i and y_i^{calc} are respectively the experimental and calculated values of C_p^{ex}; y_i^m is the mean of the experimental values of C_p^{ex}, and n is the number of points.

It is clear that equilibrium thermodynamics cannot be applied directly in the analysis of Fe^{2+}-AK_{gig} denaturation because it is controlled kinetically. However, it is possible to obtain useful thermodynamic information upon extrapolation of the transition parameters to the infinite heating rate [116]. The thermodynamic parameters thus obtained for the thermal denaturation of Fe^{2+}-AK_{gig} at pH 10 are shown in Table 4. It can be seen that the thermal stability of the Fe^{2+}-form of the enzyme is slightly lower than the Co^{2+}-AK_{gig} and Zn^{2+}-AK_{gig}. Moreover, these data support our conclusion about differences in the organization of the tertiary structure of Fe^{2+}-AK_{gig} due to changes in the value of the temperature of maximum stability (T_s) as the value testifying to the changes in hydrophobicity of this form [122], which could be the reason for the irreversibility of the thermal transition.

In this work we have reported and compared the spectroscopic, kinetic and thermodynamic properties of the Co^{2+}-, Zn^{2+}- and Fe^{2+}- holo-forms of AK_{gig}. AK_{gig} is well able to accommodate either metal, Co^{2+} or Zn^{2+}, suggesting that it is relatively insensitive to the detailed stereochemistry of the coordination of these metals. However, we found that Fe^{2+}-AK_{gig} has peculiar properties as compared with the zinc- and cobalt-containing enzymes. As mentioned above, the thermal unfolding of native Zn^{2+}/Co^{2+}-AK_{gig} is a cooperative two-state process, and is sufficiently reversible only in the 9–11 pH range, which can be correctly interpreted in terms of a simple two-state thermodynamic model [28]. The pH affects the state of ionisation of basic and acidic amino acids, which may alter ionic bonds and may change the shape of the enzyme, being favourable for Zn^{2+}- and Co^{2+}-AK_{gig}. However, as has been seen in the present work the iron-containing enzyme does not develop the same structural and catalytic properties. It is significant that metal replacement in the LID domain from the Co^{2+}/Zn^{2+}-AK_{gig} to the Fe^{2+}-AK_{gig} results in significant changes in the tertiary structure of the whole protein molecule observed in the near-

UV CD spectra and, as a result, leads to changes in the thermal denaturation process from reversible to irreversible, with a slight reduction in thermal stability observed for Fe^{2+}-AK_{gig}. The temperature of maximum activity for Fe^{2+}-AK_{gig} was found to be four degrees lower than that of Co^{2+}/Zn^{2+}-AK_{gig}. The kinetic parameters of holo-AK are significantly different. Thus, Fe^{2+}-AK_{gig} has the lowest affinity for the substrates of the forward reaction, while its affinity for the substrates of the backward reaction is the highest.

Accordingly, even subtle modifications of the LID domain with different types of metal lead to considerable changes in the physico-chemical properties of the whole enzyme. This again confirms the importance of the structural metal-binding motif and its involvement in the maintenance of the overall structure and biochemical properties of AK.

Acknowledgments

This work was supported in part by the Fundação para a Ciência e a Tecnologia (FCT) project PPCDT/POCI/QUI/59119/2004 (Portugal), Acçoes Integradas Luso Espanholas E-62/06 (Portugal-Spain), and FCT grants SFRH/BPD/28380/2006 (OYuG) and SFRH/BD/24744/ 2005 (AVK). We are thankful to Carla Rodrigues for technical help with the ICP-AES analyses (Inductively Coupled Plasma-Atomic Emission Spectroscopy).

Chapter 3

Cobalt, zinc and iron forms of adenylate kinase (AK) from the sulphate-reducing bacteria *Desulfovibrio gigas*: purification, crystallization and preliminary X-ray diffraction analysis.

This chapter was published as:

A.V. Kladova, O.Yu. Gavel, A. Mukhopaadhyay, D.R. Boer, S. Teixeira, V.L.Shnyrov, I. Moura, J.J.G. Moura, M.J. Romão, J. Trincão, S.A. Bursakov. 2009. Cobalt, zinc and iron forms of adenylate kinase (AK) from the sulphate-reducing bacteria *Desulfovibrio gigas*: purification, crystallization and preliminary X-ray diffraction analysis. Acta crystallographica. Section F, Structural biology and crystallization communications. 65(Pt 9)**:**926-929.

Abstract

Adenylate kinase (AK, ATP:AMP phosphotransferase, EC 2.7.4.3) is involved in the reversible transfer of the terminal phosphate group from ATP to AMP. AK contribute to the maintenance of a constant level of cellular adenine nucleotides, which are necessary for the energetic metabolism of the cell. Three metal ions cobalt, zinc and iron (II) have been reported to be present in AK from some Gram-negative bacteria. Native zinc-containing AK_{gig} was purified to homogeneity and crystallized. The crystals diffracted to beyond 2.1 Å. Furthermore, cobalt- and iron-containing crystal forms of recombinant AK were also obtained and diffracted to 2.0 and 3.0 Å resolution, respectively. Zn^{2+}- and Fe^{2+}-AK_{gig} crystallized in space group C2, a monomer was present in the asymmetric unit for both the Zn^{2+}- and Fe^{2+}-AK_{gig} forms and a dimer was present for the Co^{2+}-AK form. The structures of the three metal forms of AK_{gig} will provide new insights into the role and selectivity of the metal in these enzymes.

1. Introduction

Adenylate kinases (AK, ATP:AMP phosphotransferase, EC 2.7.4.3) catalyze the reaction: Mg^{2+}ATP+AMP↔Mg^{2+}ADP+ADP. Like most nucleotide-binding proteins, AK belong to the α/β class of proteins (a five-stranded β-sheet surrounded by several α-helices) [98]. AK comprises three domains: the CORE, which contains the P-loop that plays an important role in binding of the triphosphate group of ATP, the AMP-binding domain, and the LID [35]. The AMP-binding domain contributes to the binding of AMP, closing over bound AMP. The LID domain is well exposed to the solvent and undergoes a large shift during catalysis and upon substrate binding, closing over the active site and protecting the MgATP/AMP-ternary complex from bulk water, facilitating phosphoryl transfer and preventing hydrolysis [18]. Motions can also be observed for substrate-free AK and follow the direction of the catalytically competent conformation [123].

AK from Gram-positive bacteria usually contain the Cys-X_2-Cys-X_{16}-Cys-X_2-Cys/Asp structural motif in the LID domain that is responsible for the zinc ion binding [13, 20, 22]. Gram-negative bacteria are usually devoid of metal ions as the cysteine residues are substituted by other highly conserved amino acids - His, Ser, Asp and Thr. Nevertheless, the following exceptions were reported: AK from *Desulfovibrio gigas* (metal-chelating motif is ^{129}Cys-X_5-Hys-X_{15}-Cys-X_2-Cys) and *Desulfovibrio desulfuricans* ATCC 27774 that contain either cobalt or zinc [24] , recombinant AK from *Paracoccus denitrificans*, overproduced in *E. coli* (^{126}Cys-X_2-Cys-X_{16}-Cys-X_2-Cys) [15, 16], that binds either zinc or iron and zinc-containing AK from *Thermotoga neapolitana* (^{134}Cys-X_2-Cys-X_{16}-Cys-X_2-Cys) and *Chlamidia pneumoniae* (^{133}Cys-X_2-Cys-X_{12}-Cys-X_2-Cys) [25, 26]. The motif Cys-X_5-His-$X_{14\text{-}19}$-Cys-X_2-Cys is also present in the AK from other *Desulfovibrio* and *Streptomyces* and may also capture metal ions [24].

Thus, three different metal atoms - zinc, cobalt and iron - were found in AK from some Gram-negative bacteria.

In this work we report the purification, crystallization and preliminary X-ray characterization of the native zinc- and overexpressed cobalt- and iron-containing forms of AK from *D. gigas*. The diffraction data were collected for Co^{2+}-, Zn^{2+}- and Fe^{2+}-AK_{gig} to 2.0, 2.1 and 3.0 Å resolution, respectively. These data will allow the structure determination of all three holo-AK that will help elucidate the metal-coordination sphere and its role in the folding of the LID domain and may shed some light on the understanding of thermodynamic properties of AK_{gig} [28].

2. Materials and methods

2.1 Purification

D. gigas cells were grown in a 400 l fermenter (Bacterial Chemistry Lab, Dr. René Toci at the C.N.R.S., Marseille, France). *D. gigas* cells were grown under anaerobic conditions in a basal medium as described by LeGall et al. [124], using a lactate/sulphate medium. Cells were harvested at the beginning of the stationary phase, resuspended in 10 mM Tris/HCl buffer at pH 7.6 in a 1:4 (w/v) ratio, and passed through an EmusTex-C5 Homogenizer at 75 kPa. 1 mM Phenylmethylsulphonyl fluoride (PMSF) was added to the homogenate as an inhibitor of serine proteases**.** The extract was centrifuged at 15 000 g for 65 min, after which the pellet was discarded. The supernatant was subjected to further centrifugation at 180 000 g for 90 min at 277 K in order to eliminate the membrane fraction. A clear supernatant, containing the soluble fraction, was then used for the purification of AK, which was processed immediately.

The gene coding for the AK of *D. gigas* (670bp DNA fragment; EMBL accession No. FN424087) was amplified (annealing temperature 337 K) from *D. gigas* genomic DNA by polymerase chain reaction (PCR) with the appropriate upstream primer 5'-GGGGCTCGAGCA/TATGAACATCCTGATCTTCGGTCCGAACGGC-3' and downstream primer 5'-CCCCGGATCCA/AGCTTTTAGGCAAGCTGGGCCAG-3'. The PCR fragment containing upstream *NdeI* and downstream *HindIII* restriction sites were cloned into the pMOS*Blue* vector (GE Healthcare) and the nucleotide sequence of the PCR product was verified by DNA sequencing. The *NdeI* and *HindIII* digestion product of theDNA fragment was then cloned into the expression vector pET-22b(+) (Novagen). The resulting plasmid pET-22b(+)/AK with the gene inserted was used for protein expression in *E. coli* strain BL21(DE3) (Stratagene).

The cells were grown at 310 K in minimal media M63B1 (0.1 M KH_2PO_4, 15 mM $(NH_4)_2SO_4$, 0.8 mM $MgSO_4$, 3 μM B_1 vitamin, pH 7.4) supplemented with 0.4 % glucose [16]. The time of incubation and the metal ion concentration in the medium were optimized to the purpose of homogeneous protein production (with the metal:protein ratio of 1:1). Expression was induced with isopropyl-beta-D-thiogalactopyranoside (IPTG) to a final concentration of 1 mM and appropriate concentration of metal ion when the culture reached an OD_{600} of 0.6. For Co^{2+}-AK_{gig} the optimal conditions were 160 μM of $CoCl_2$ and 6 hours of incubation; for Zn^{2+}-AK_{gig}, 250 μM of $ZnCl_2$ and 4 hours of incubation; for Fe^{2+}-AK_{gig}, 130 μM $FeCl_2$ and 4 hours of incubation.

Purification of the native and recombinant AK_{gig} was performed as described previously [28] by a two-step procedure involving FPLC chromatography (Pharmacia) on a Blue Sepharose fast flow column followed by gel filtration on a Superdex-75 column. Both purification steps were performed aerobically at 4 °C. Specific activities of enzymes were determined at each step along the purification process [24].

The purity of the protein was determined by SDS-PAGE at 12.5 % (w/v) as described by Laemmli [103] at each purification step.

The quantification of metals was performed by ICP-AES analysis (Inductively Coupled Plasma-Atomic Emission Spectroscopy) in a Horiba Jobin-Yvon apparatus model Ultima with standard solutions (Aldrich) containing cobalt, iron and zinc ions.

2.2. Crystallization, data collection and processing

After purification, the buffer was exchanged to 20 mM Tris/HCl pH 7.6 and the protein was concentrated to ~10 mg ml^{-1}.Crystallization trials of the AK_{gig} were performed using the hanging-drop vapour-diffusion method using 2 µl drops (with a protein:well solution ratio of 1:1, 1:2 and 1:3) over 700 µl of well solution. Initial crystallization conditions were screened using an in-house modified version of the sparse-matrix method of Jancarik & Kim [125] in combination with the commercial Crystal Screen and Crystal Screen 2 from Hampton Research (California, USA) at 277 and 293 K. Crystallization conditions were improved by screening additives and varying the protein and precipitant concentrations.

Multiple data sets were collected either on an in-house Cu-K*α* rotating-anode generator or at the European Synchrotron Radiation Facility (ESRF, Grenoble, France). Crystals were flash-cooled directly in liquid nitrogen and stored or transferred to a gaseous nitrogen stream (100 K) using Paratone oil as a cryoprotectant. The best data set was collected on beamline ID14-3 at the ERSF using an ADSC Quantum-4R detector. The data were processed using MOSFILM v.7.0.1 and SCALA from the CCP4 package v.6.0.2 [126].

3. Results and discussion

Native zinc/cobalt- containing AK_{gig} was purified to homogeneity and crystallized. AK from *Desulfovibrio* strains were the first AK found to contain cobalt [24, 28].

The best crystallization conditions were 0.2 M tartrate Na/K, 0.1 M MES (pH 6.5) and 20 % PEG 2K or 8K (the protein:well solution ratio in the drop was 1:1, 1:2 or 1:3 with the final drop volume of 4, 6 or 8 µl) using a protein stock concentration of ~10 mg·ml^{-1} at 277 K. Crystals grew to about 0.30×0.07× 0.07 mm (**Fig. 1**).

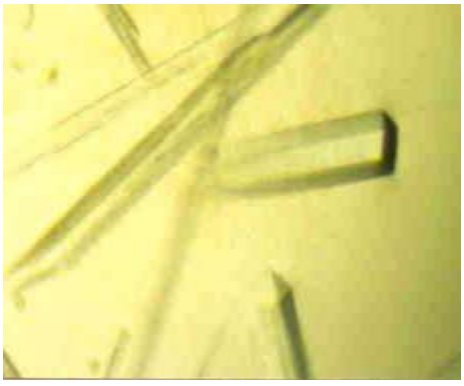

Fig. 1. Crystals of native AK from *D. gigas* (aprox. size 0.30 × 0.07 × 0.07 mm)

Cobalt and iron-containing AK_{gig} were overexpressed in *E. coli* cells grown in controlled media, in order to ensure full metal occupancy. The 1:1 ratio of metal to protein was assayed by metal analysis. Recombinant AK_{gig} were crystallized in similar conditions as for the native protein. The Co^{2+}-, Zn^{2+}- and Fe^{2+}-AK_{gig} crystals diffracted to beyond 2.0, 2.1 and 3.0 Å, respectively (**Fig. 2**).

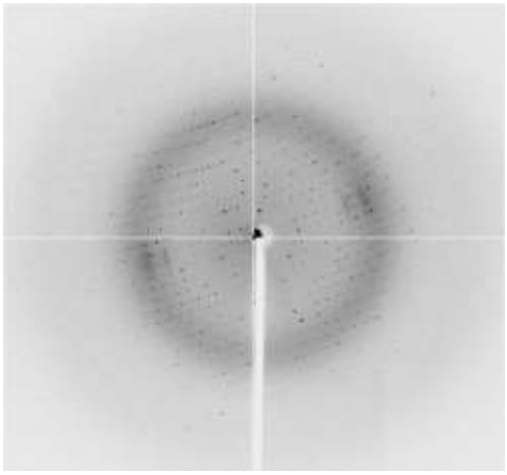

Fig 2. Diffraction pattern of the *D. gigas* AK crystal (the resolution at the edge is 1.5 Å) obtained on beamline ID14-3 (ESRF).

Zn^{2+}-AK_{gig} and Fe^{2+}-AK_{gig} crystallized in space group *I222*, with similar unit cell dimensions, whereas Co^{2+}-AK_{gig} crystallized in space group *C2* (**Table 1**). A full 180° data set was collected for each crystal, with 1° oscillation per image. The calculated Matthews coefficient [127] for Zn^{2+}- Co^{2+}- and Fe^{2+}-AK_{gig} crystals is 3.59, 2.31 and 3.46 $Å^3$ Da^{-1}, respectively, assuming the presence of a monomer in the asymmetric unit both for the Zn^{2+}-AK_{gig} and Fe^{2+}-AK_{gig} forms and a dimer for the Co^{2+}-AK_{gig} form. Data collection and processing statistics are shown in **Table 1**.

X-ray fluorescence scans were performed for each crystal form, which allowed confirming the nature of the present anomalous scatterer. MAD datasets were collected for each crystal at three wavelengths corresponding to the peak, inflection point and a remote wavelength for each atom. These datasets are now being used to obtain the structures of each form of the enzyme. Comparison of these structures will help understand the biophysical and biochemical data available as well as elucidate on the role of the metal present in these enzymes.

Table 1. Data collection statistics.

Data set	Zn^{2+}-AK_{gig}			Co^{2+}-AK_{gig}	Fe^{2+}-AK_{gig}
	peak	inflection	remote		
X-ray source	ID14-3			ID29	ID29
Crystal data					
Crystal system	Orthorhombic			Monoclinic	Orthorhombic
Unit-cell parameters					
a (Å)	39.39			131.53	38.80
b (Å)	119.44			39.51	119.16
c (Å)	149.59			94.30	146.71
α (°)	90			90	90
β(°)	90			109.43	90
γ(°)	90			90	90
Max. resolution (Å)	1.8			2.0	3.0
Mosaicity	0.73			0.63	0.73
Molecules per ASU	1			2	1
Matthews coefficient ($Å^3$ Da^{-1})	3.59			2.31	3.46
Solvent content (%)	65.5			48.3	64.3
Data collection and processing					
Space group	I222			C2	I222
Resolution limits (Å)	25.0–1.8	25.0–1.8	25.0–1.8	44.5–2.0	59.5–3.0
Wavelength (Å)	1.2852	1.2855	1.2825	1.6064	1.7266
No. of observed reflections	202932 (17350)	184103 (14708)	195516 (17373)	109104 (16014)	25156 (3637)
No. of unique reflections	33146 (4618)	33841 (4649)	33272 (4723)	31103 (4417)	6444 (918)
Redundancy	6.1	5.4	5.9	3.5	3.9
$R_{p.i.m.}$ †	0.063 (0.447)	0.069 (0.539)	0.049 (0.414)	0.058 (0.327)	0.078 (0.246)
Completeness (%)	99.6 (97.3)	99.3 (95.5)	99.8 (99.1)	97.7 (94.4)	91.3 (92.0)
Anomalous completeness (%)	97.8 (87.6)	95.6 (78.9)	97.6 (89.2)	—	—
$\langle I/\sigma I \rangle$	11.0 (1.7)	9.4 (1.4)	12.4 (2.0)	9.0 (2.1)	15.0 (5.1)

† Precision-indicating merging R factor:  , with *N* being the number of times a given reflection *hk*l was observed; $I_i(hkl$ is the ith observation of reflection *hkl* [128].

Acknowledgments

This work was supported in part by Fundacão para a Ciência e Tecnologia POCI/QUI/59119/2004, by CRUP - Acções Integradas Luso-Esp. E-62/06 projects and FCT grants SFRH/BD/24744/2005 (AVK), SFRH/BPD/28380/2006 (OYuG), SFRH/BPD/30142/2006(AM).

Chapter 4

Metal containing adenylate kinase from *Desulfovibrio gigas*: crystal structure of a novel metal containing adenylate kinase from Gram-negative bacteria

This chapter was prepared for publication as:

A. Mukhopaadhyay, A.V. Kladova, S.A. Bursakov, O. Yu. Gavel, J. Trincão, I. Moura, J.J.G. Moura, M.J. Romão. 2010. Metal containing adenylate kinase from *Desulfovibrio gigas*: Crystal structure of a novel metal containing adenylate kinase from Gram-negative bacteria

Abstract

Adenylate kinases (AK) from Gram-negative bacteria are usually devoid of metal ions in their LID domain. So far, three metal ions have been reported in AK from Gram-negative bacteria. Crystal structures of substrate free AK from *Desulfovibrio gigas* (AK_{gig}) with three different metal ions (Zn^{2+}-, Co^{2+}- and Fe^{2+}-AK_{gig}) bound in its LID domain have been determined by X-ray crystallography to resolutions 2.1, 2.0 and 3.0 Å, respectively. The zinc and iron forms of the enzyme crystallized in the space group *I222*, whereas the cobalt form crystals were *C2*. The presence of the metals was confirmed by calculation of anomalous difference maps and by X-ray fluorescence scans. The work presented here is the first report of a structure of a metal containing from a Gram-negative AK. Native Co^{2+}/Zn^{2+} enzyme was crystallized, but only zinc was detected in its LID domain. Co^{2+}- and Fe^{2+}-AK_{gig} forms were obtained by overexpressing the protein in *E. coli* grown in minimal medium supplemented with the appropriate MCl_2 (where M is Co^{2+}, Zn^{2+}, Fe^{2+}). Zn^{2+}- and Fe^{2+}-forms of AK_{gig} crystallized as monomers in the asymmetric unit, whereas the Co^{2+}-AK_{gig} crystallized as a dimer. However, all three crystal structures are very similar to each other with the same LID domain topology, with the only change being the presence of different metal atoms in it. In the absence of any substrate, the LID domain of all holo forms of AK_{gig} was present in a fully open conformational state. Normal mode analysis was performed and fluctuation of the LID domain along the catalytic pathway was predicted.

Introduction

Adenylate kinase (ATP:AMP phosphotransferase, EC 2.7.4.3; AK) is an essential catalyst for bacterial growth and multiplication. It is involved in the reversible transfer of the terminal phosphate group from Mg^{2+}ATP to AMP with high energy turnover: Mg^{2+}ATP + AMP↔Mg^{2+}ADP + ADP [7]. AK belongs to a family of enzymes essential to life [11], and is highly abundant.

AK belong to the α/β class (a five stranded β- sheet surrounded by several α-helices) [17, 20, 98]. They are composed of three main regions: LID, CORE and AMP-binding domains. The LID and AMP-binding regions participate in the isolation of the substrates and therefore undergo significant conformational changes during catalytic reaction [35]. Two mobile domains themselves (the AMP_{bind} and LID domains), not their hinges or the counterweight loops, control the temperature dependence of the catalytic activity [129]. AK are generally monomeric, but also dimeric [130, 131] and trimeric [132] structural forms are known. Simultaneous coexistence of monomeric and dimeric forms and supramolecular assembly of AK were also shown [133, 134].

AK are divided into two groups: the short and long forms, which differ in a 20-30 amino acid residue insertion in the LID domain [17, 20]. Mammalian AK is usually of the short form (both cytosolic and nuclear AK), whereas the long AK are found in most bacteria, yeast and mitochondria. In short AK, the LID domain is reduced to a small irregular loop of less than 11 amino acids. However, the rest of the primary structure, the overall fold, and the side chains involved in nucleotide binding and catalysis are conserved among the short and long variants.

AK from Gram-positive bacteria usually contain zinc ion. The structural motif responsible for zinc binding is Cys-X_2-Cys-X_{16}-Cys-X_2-Cys/Asp [13, 20, 22]. The sulphur positions of the four Cys side chains of Gram-positive bacteria are geometrically optimized to bind the putative zinc ion [19]. In AK from Gram-negative bacteria cysteine residues are substituted by four highly conserved amino acids – His, Ser, Asp and Thr, respectively, suggesting that these residues might play essential roles [23]. The crystal structure of the AK from *E. coli* (AK_{col}) shows that the LID domain forms a single distorted antiparallel β-sheet, two turns and one loop structure [18]. The four amino acids mentioned (His, Ser, Asp and Thr) lie on distorted the β-sheet, and are involved in the formation of a hydrogen-bond network that stabilizes the LID structure. In AK from Gram-positive bacteria, zinc seems to stabilize the LID domain more readily than does the hydrogen network present in Gram-negative bacteria and all of the eukaryotic long-form AK determined so far [19, 20]. Presence of metal in the LID domain may cause considerable differences in overall stability of AK and its removal leads to partial or complete loss of catalytic activity [23, 24, 26, 28, 99, 129].

The following exceptions have been reported for metal-containing AK from Gram-negative bacteria: AK from *Desulfovibrio gigas* (metal-chelated motif is ^{129}Cys-X_5-His-X_{15}-Cys-X_2-Cys) and *Desulfovibrio desulfuricans* [24], that contain either cobalt or zinc, AK from *Paracoccus denitrificans* (^{126}Cys-X_2-Cys-X_{16}-Cys-X_2-Cys) overproduced in *E. coli*, that binds either zinc or iron [15], AK from *Chlamydia pneumoniae* (^{133}Cys-X_2-Cys-X_{12}-Cys-X_2-Cys) and *Thermotoga neapolitana* (^{134}Cys-X_2-Cys-X_{16}-Cys-X_2-Cys), which contain zinc [25, 26]. Thus, up to now, only three metal ions, cobalt, zinc and iron, were found in AK from Gram-negative bacteria.

To investigate the role of these three metal ions, and their influence in activity and structural stability in AK from Gram-negative bacteria, AK was overproduced in *E. coli* and homogeneous Co^{2+}-, Zn^{2+}- and Fe^{2+}- forms of AK were obtained (with the metal/protein ratio is 1/1). Herein, we report the crystal structures of substrate-free Co^{2+}-AK, Zn^{2+}-AK and Fe^{2+}-AK_{gig} forms at 2.0, 2.1 and 3.0 Å resolutions, respectively.

Crystallization

Crystals were grown at 4°C using the hanging drop vapor diffusion method. The best crystallization conditions were 0.2 M tartrate Na/K, 0.1 M MES (pH 6.5) and 20% PEG 2K or 8K (the protein:well solution ratio in the drop was 1:1, 1:2 or 1:3 with the final drop volume of 4, 6 or 8 µl) using a protein stock concentration of ~10 $mg.ml^{-1}$. The crystals were cryoprotected by soaking at 277K in mother liquor containing 15-30 % glycerol. The crystals were then flash cooled in a stream of nitrogen gas at 100 K.

Fluorescence scan, diffraction data, structure analysis and refinement

Diffraction data were collected at beam lines at ESRF (Grenoble, France) using either a Quantum 4 or a 315R CCD detector (ADSC). All the data sets were processed and scaled using MOSFLM and SCALA from the CCP4 suite [126, 135, 136]. Details of data collections and processings are presented in **Table 1**. Due to difficulties in obtaining a MR solution using models of AK from other organisms, the structure of Zn^{2+}-AK_{gig} was solved by MAD using the bound zinc as the anomalous scatterer. A single crystal was used to collect data to 2.10 Å at the zinc peak, at the edge and at a remote wavelength. The crystal belongs to space group *I222*. Fluorescence scans were performed with the crystals of Co^{2+}- AK_{gig} and Fe^{2+}-AK_{gig} to confirm the presence and type of metal ion in the crystals (**Fig. 1**).

Three data sets were collected for Co^{2+}-AK at the cobalt peak (λ=1.6029Å), at the edge (λ=1.6064Å) and at the remote wavelength (λ=1.5979Å), respectively, with a φ rotation of 1° per image. The dataset collected at the edge was used for structure solution. Structure was solved by

Table 1. Data-collection statistics (values in the parenthesis are for the highest resolution shell).

Dataset	Zn^{2+}-AK_{gig}	Co^{2+}-AK_{gig}	Fe^{2+}-AK_{gig}
Xray source	ID-14-3	ID-29	ID-29
Crystal data			
Crystal system	Orthorombic	Monoclinic	Orthorombic
Unit cell parameters	a=39.39 b=119.44 c=149.59 α=90.0 β=90.0 γ=90.0	a=131.53 b=39.51 c=94.30 α=90.0 β=109.43 γ=90.00	a=38.80 b=119.16 c=146.71 α=90.0 β=90.0 γ=90.0
Max. resolution (Å)	1.78	2.00	3.00
Mosaicity	0.73	0.63	0.73
Molecules per ASU	1	2	1
Matthews coefficient ($Å^3$ Da^{-1})	3.59	2.31	3.46
Solvent content (%)	65.5	48.3	64.3
Data collection and processing			
Space group	*I222*	*C2*	*I222*
Resolution limits (Å)	20-1.78	44.49-2.00	59.55-3.00
Wavelength (Å)	1,2825	1.6064	1.7266
No. of observer reflections	205787 (16293)	109104 (16014)	25156 (3637)
No. of unique reflections	34120 (4707)	31103 (4417)	6444 (918)
Redundancy	6.0	3.5	3.9
R_{pim}	0.069 (0.49)	0.058 (0.327)	0.078(0.246)
Completeness (%)	99.2 (95.3)	97.7(94.4)	91.3(92.0)
$\langle I/\sigma I \rangle$	10.2 (1.6)	9.0(2.1)	15(5.1)

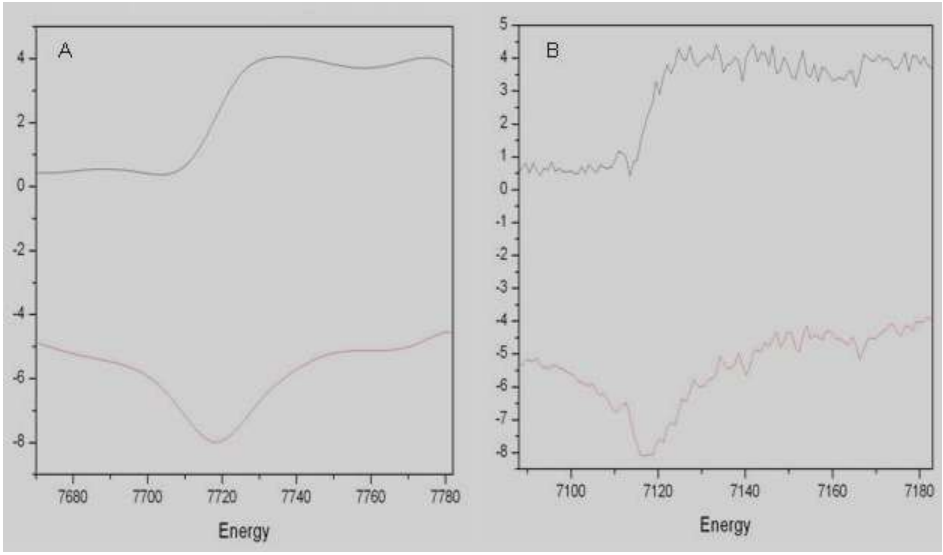

Fig. 1 Fluorescence scan of Co^{2+}-AK_{gig} (A) and Fe^{2+}-AK_{gig} (B), respectively.

Table 2. Refinement parameters and statistics.

	Zn^{2+}-AK	Co^{2+}-AK	Fe^{2+}-AK
Resolution	93.33 – 1.80	44.45 – 2.00	90.00 – 3.00
Reflections used	31475	28920	6147
R_{work}[a] (%)	19.55	21.35	19.98
R_{free}[b] (%)	23.09	27.82	26.56
Mean protein B factors ($Å^2$)	24.414	26.0	68.0
Ramachandran plot[d] Residues other than Gly and Pro in :			
Most favoured region (%)	99.10	97.06	88.99
Additional allowed region (%)	0.90	3.98	9.58
Disallowed regions (%)	0	0.23	1.83

[a] R_{work} = Σ ||F_{calc}| - |F_{obs}||/ Σ |F_{obs}| x 100, where F_{calc} and F_{obs} are the calculated and observed structure factor amplitudes, respectively.
[b] R_{free} is calculated for a randomly chosen 5% of the reflections for each dataset
[c] R_{map} is the R-factor for the map calculated by the EDS server (http://eds.bmc.uu.se/eds) for the final PDB coordinates
d Calculated using MolProbity

molecular replacement by PHASER [137] using Zn^{2+}-AK_{gig} as a search model. The data in the resolution range 44.45 – 2.00 Å were used for molecular replacement. The best solution was obtained in *C2* space group with two molecules in the asymmetric unit. First restrained refinement, after the density modification, with 44.45 – 2.00 Å data using REFMAC 5.2.0019 [138] resulted in R = 0.313 and R_{free} = 0.320. For Fe^{2+}-AK, 180 images were collected, with φ rotation of 0.6° per image, at the Iron edge (λ=1.7266Å). The structure was also solved by molecular replacement by PHASER [137] using the data in the resolution range 59.58 – 3.00 Å. The best solution was in *I222* space group with a single molecule in the asymmetric unit. First restrained refinement, after the density modification, with 90.00 – 3.00 Å data using REFMAC 5.2.0019 yielded with R = 0.307 and R_{free} = 0.310. Iterative model building with COOT [139], guided by $2F_0$-F_c and F_0-F_c maps, together with restrained refinement in REFMAC 5.2.0019 [138], initially, and then with restrained refinement including TLS resulted in good final models

for all the structures. The final model Co^{2+}-AK_{gig} include amino acid residues 1-223, water molecules and two molecules of tartaric acid from the cryoprotectant solution. The TLS refinement was done by treating the whole protein as a single TLS entity. The final refinement statistics are presented in **Table 2**. One glycerol molecule was found in the asymmetric unit in both Zn^{2+}-AK_{gig} and Fe^{2+}-AK_{gig}. The region 206-223 is partially disordered with no visible density for residue 209. The residues with disordered side chains were stubbed at Cβ keeping the label same. We could only locate 7 water molecules in the final Fe^{2+}-AK_{gig} structure. We included 10 separate TLS entities in the final TLS restrained refinement.

Results and discussion

Structural overview

The crystal structures of Zn^{2+}-AK_{gig} from native Zn^{2+}/Co^{2+} -containing AK_{gig} [24] and recombinant Co^{2+}-AK_{gig} and Fe^{2+}-AK_{gig} were determined at 2.1, 2.0 and 3.0 Å resolution, respectively. A summary of data collection and refinement statistics is presented in **Table 1** and **Table 2.** Zn^{2+}-AK_{gig} and Fe^{2+}-AK_{gig} crystallized as monomers in the asymmetric unit in space group *I*222, whereas Co^{2+}-AK_{gig} crystallized in space-group *C*2 as a dimer in the asymmetric unit. Superposition of the three structures yields root mean square derivation (rmsd) values of 0.10 (Zn^{2+}-AK_{gig} vs Co^{2+}-AK_{gig}) and 0.37 Å (Zn^{2+}- AK_{gig} vs Fe^{2+}-AK_{gig}), respectively indicating that all three holo-forms of AK have almost identical structures. The most striking observation is that replacement of metal ion has no visible effect on the structure compared to the wild-type.

Like the other AK structures, Zn^{2+}-, Co^{2+}- and Fe^{2+}-AK_{gig} contain the characteristic LID (residues 125-163) and the CORE domain (residues 1-124 and 164-223), which also includes the AMP binding region. The LID domain harbours the ^{129}Cys-X_5-His-X_{11}-Cys-X_2-Cys-motif, which is responsible for the metal binding in a tetrahedral fashion in AK_{gig}. The CORE domain encloses the AMP binding region (residues 31-60). It is composed of a five-stranded beta sheet that are surrounded by seven alpha helices. Two alpha helices (residues 116-123 and residues 165-173) connect the LID and the CORE domains and function as a hinge. Zn^{2+} and Fe^{2+}-AK_{gig} have one molecule of glycerol and Co^{2+}-AK_{gig} has one molecule of tartaric acid bound in the CORE domain near the residues 10-14. These solvent molecules are strongly bound to the Arg124 residue of the connecting alpha helices or “hinge” and to the backbone nitrogen atom of Gly10 and Gly12, respectively. These interactions might help to stabilize this particular conformation of the enzyme. B-factor distributions of these structures show that the residues in the LID domain are in the same range of the rest of the structure, showing that it is in a well-defined position.

To confirm the character of the metal ions, anomalous data were collected for both the Zn^{2+} and the Co^{2+} containing AK_{gig} at three different wavelengths, corresponding to the Zn^{2+} or Co^{2+} absorption peak, edge and to a remote wavelength, respectively. Incorporation of Co^{2+} was verified with a fluorescence scan spanning across both the zinc and the cobalt edges. A clear signal was found for the cobalt whereas no zinc was detected. (**Fig. 1A**). To further confirm that the incorporated metal was indeed cobalt, an anomalous map was calculated using MAD data sets collected at the cobalt absorption peak and edge (1.6029 Å with an anomalous signal for cobalt f" 4.0 e whereas the signal for zinc is 0.7 e at this wavelength). The next data set was collected at the cobalt edge with anomalous signal f" 2.2 e. The anomalous map was calculated from both data sets (**Fig. 2**). Both data sets showed a strong anomalous peak corresponding to cobalt atom in the metal binding site. This peak was noticeably weaker at the remote wavelength. For the confirmation of the iron in Fe^{2+}-AK_{gig} the same procedure was done at the respective peak and edge wavelengths (**Fig. 1B**).

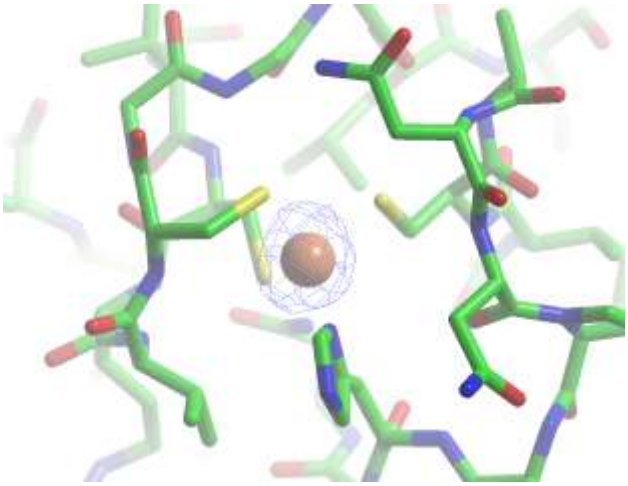

Fig. 2 Anomalous map for Co^{2+}-AK_{gig} calculated at 4 σ above the cobalt edge.

LID domain and metal coordination

The AK family is divided into two types based on the polypeptide chain length, with the longer variants evidencing a larger LID domain with an insertion of 20-30 residues [140]. The short AK conserve their catalytic activity despite the reduced LID domain (less than 11 residues), but seem to lose the high specificity for ATP [141]. The AK_{gig} is of the first type, with a longer LID domain that consists of 28 residues (residues 125 – 163). The distance between the LID and CORE domain is 12.35 Å (distance between Cα of Arg126 and Gly12). In all other structurally characterized AK with or without substrate, LID and CORE domains are not that far apart from each other. This indicates that these structures of AK_{gig} are in a fully open state. The Arg126 and Arg164 residues, which are located in the hinges, take part in the LID and mediate

catalysis because of their electrostatic interactions with phosphate groups of substrates. When the substrate is present these two arginines drag the LID domain closer to the CORE domain [20]. The conformation of the LID domain is more open in our structures compared to substrate bound AK. These crystal structures show that the LID domain is stabilized by strong backbone hydrogen bond interactions and few attractive hydrogen bond interactions between the side chains. The residues involve in the hydrogen bonding network are Asn137, Arg127, Asn138, Ile144, Ile128 and Ser159. Apart from that several non-bonded interactions between the residues of the LID domain and the CORE domains and also with its symmetry mates contribute to the stabilization of the open conformation in the crystal. These strong non bonded interactions along with the metal chelation in the LID domain enhance the thermal stability of the enzymes and also give it the structural integrity so that it can move as solid block into the ATP binding pocket at the time of catalysis [23]. The LID domains of the holo-AK_{gig} and AK from *E. coli* (AK_{col}) are very similar. Therefore, the role of metal atom inside is only structural. However, as it was shown previously [28], the metal atom inside the LID domain provides thermal stabilizing effect to the protein. The T_m values for apo- and holo- forms at pH 10 were 39.7 and 48.8 °C, respectively.

The LID domain shares the same topology as a zinc finger domain, present in other zinc containing AK [20]. The metal ions (Co^{2+} or Zn^{2+} or Fe^{2+}) are tetrahedrally coordinated to the 26 residues long sequence ^{129}Cys-X_5-His-X_{11}-Cys-X_2-Cys. The metal ion is located in an identical position in each structure. The distance between the ligating atoms and metal ion are in the range 2.13 – 2.42 Å for zinc, 2.00 – 2.42 for cobalt and 1.98 – 2.60 Å for iron ions respectively. The overall topology and conformation of the LID domain remains unchanged in all the structures. This observation also supports the idea that the bound metal atoms in AK of Gram-negative bacteria are structural in nature, not catalytic. The substitution of Zn^{2+} ion from the zinc finger motif by the redox metal atoms like Fe^{2+}, Co^{2+}, Ni^{2+} have already been reported [142], where the redox metal atoms showed lesser affinity than Zn^{2+}.

CORE domain

The CORE domain is connected to the LID by residues 116-123 and 165-173. The latter are part of the counterweight loop, which is believed to control the movement of the LID domain during catalysis. This CORE domain mainly consists of a five stranded beta sheet surrounded by 5 helices that keep the integrity of the tertiary structure of the enzyme. A Walker motif [143] with conserved sequence G-X-X-G-X-G-K is present in the N-terminal region. This represents the phosphate binding loop characteristic of all AK. Gilles et. al. have proposed that the sequence Gly84-Phe85-Pro86-Arg87 (GFPR) present in the CORE domain plays a crucial role in

stabilizing the tertiary structure of the enzyme [22]. The Pro86 residue was also in a cis conformation similar to the other structurally characterized AK (**Fig. 3**). A major difference between these structures and the structures of substrate bound AK is in the region of residues 31-63. In the substrate bound structures this region rotated towards the CORE domain by as much as 5 Å.

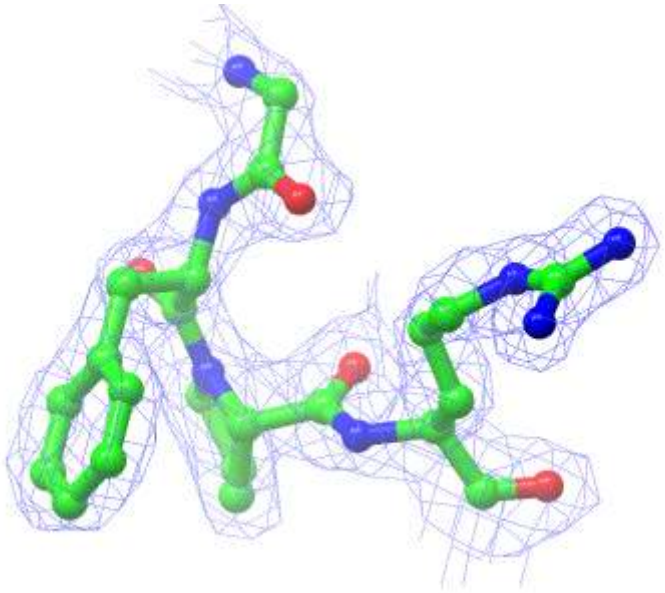

Figure 3. Electron density around the unique four residues in the CORE. Gly84-Phe85-Pro86-Arg87 and Pro86 is in cis conformation in Co^{2+}-AK_{gig}.

Dimer formation and crystal packing

Experimental results show that the wild type Zn^{2+}-AK and the other two forms, Co^{2+}-AK and Fe^{2+}-AK, are usually found as monomers in solution. Mass spectrometric data shows a small peak corresponding to dimer formation. This indicates that the enzyme can dimerize in solution. Co^{2+}-AK was crystallized as a non-crystallographic dimer (*C2* space group). Crystal packing forms two main contact surfaces: *face to face* (**Fig. 4A**) and *back to back* (**Fig. 4B**). The non-accessible surface area in the interface of the face to face dimer is ~1010$Å^2$, almost double the back to back dimer ~ 606 $Å^2$. The *back to ba*ck dimer is stabilized by 6 hydrogen bonds and 6 salt bridge interactions, and involves residues 50 - 55 and 172 - 185 (**Fig. 4B**). In the *face to face* dimer, most of the interactions take place through the LID domain and residues 10 - 15 of one molecule and the corresponding residues in its symmetry mate (-x, y, -z) (**Fig. 4A**). This dimer is held by 15 strong hydrogen bond interactions.

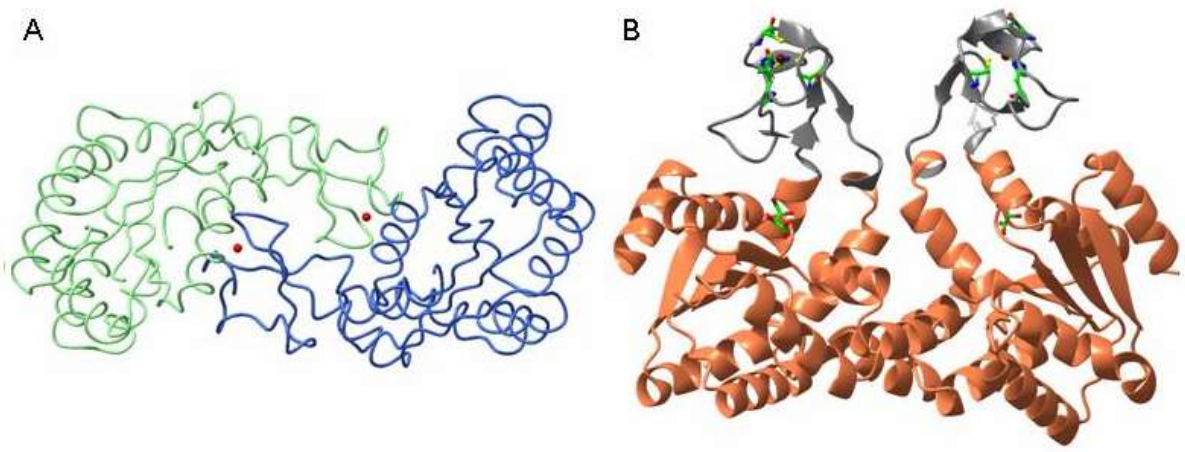

Fig. 4 *Face to face* (A) and *back to back* (B) dimer formation in AK_{gig}.

The electrostatic surfaces reveal a highly charged patch on the LID domain, where the *face to face* interactions occur and also where it binds the substrate during catalysis. The back of the enzyme is mainly non-charged (**Fig. 5**).

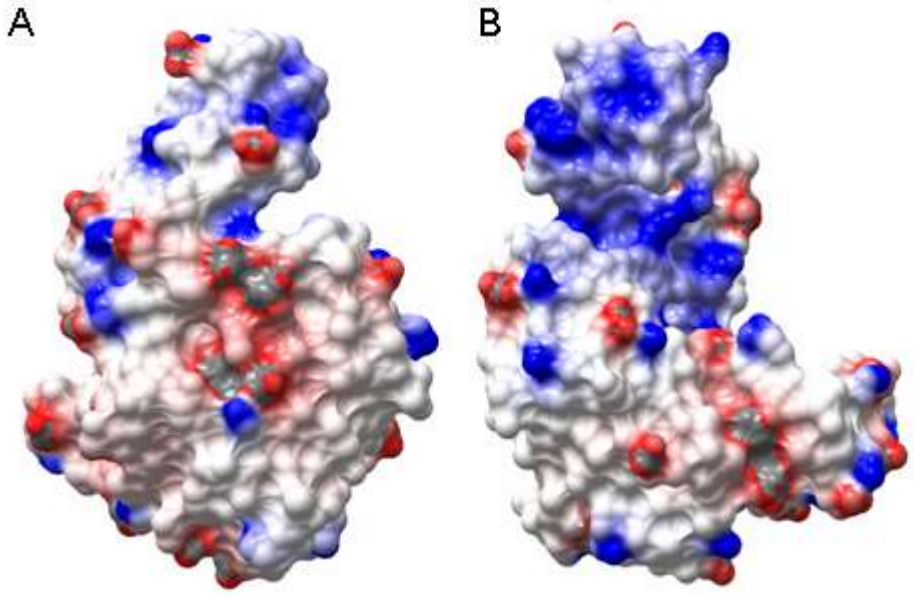

Fig. 5 Electrostatic surface showing the back of the enzyme (A) and the face of the enzyme (B). The blue and red colours corresponds to the positively and negatively charged residues, respectively

The Fe^{2+}-AK_{gig} and Zn^{2+}-AK_{gig} have almost similar tertiary structure like Co^{2+}-AK_{gig}. Due to the different space group (*C2* and *I222* respectively) they have slightly different crystal packing and different solvent content (Mathew coefficients for Zn^{2+}-AK_{gig}, Co^{2+}-AK_{gig} and Fe^{2+}-AK_{gig} are 3.59, 2.31 and 3.46, respectively). Fe^{2+}- and Zn^{2+}-AK_{gig} also form the *face to face* and *back to back* dimer with their crystallographic symmetry mates (-x+1, y, -z and –x+1, y, -z respectively). Identically to the Co^{2+}-AK, the *face to face* dimer is more stable, with 14 hydorgen

bonds involving the LID domain and almost twice the non-accessible surface area in the interfaces of the dimers compared to the *back to back* one, which is stabilized only by 6 hydrogen bonds and 6 salt bridge interactions. This stable crystal packing and the strong hydrogen bonding interactions in the *face to face* dimer can be mainly attributed to the conformation of the LID domain. Due to these interactions, the LID is stabilized in the open conformation. Zn^{2+}- and Fe^{2+}-AK_{gig} also form a tetramer due to the crystal packing. Two dimers (*face to face* and *back to back*) and the rotational symmetry mate (x, -y, -z) are involved in this oligomer formation (**Fig. 6**).

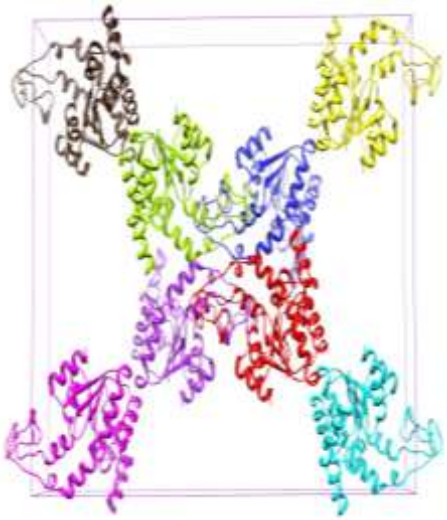

Fig. 6 Crystal packing in the unit cell of the Zn^{2+}-AK_{gig} showing the tetramer. Symmetry codes involved are –x+1, y, -z; -x+1, y, -z; x, -y, -z; x-1/2,-y+1/2,-z+1/2.

NMA study of the LID domain

To check the dynamics of the LID and AMP binding domains normal mode analysis was performed, providing a good idea of the directionality of the dynamic motion around the hinge region. The lowest frequency modes obtained from the normal mode analysis give good correlation of the experimentally observed changes in conformation [144, 145]. The LID domain and the AMP binding region in the CORE domain are directly involved in the dynamic event in the time of catalysis. They close over the enzyme's ATP and AMP binding sites, respectively. Several crystal structures of the enzyme from various organisms show a large conformational change of the enzyme mainly in these two regions. Computational pathway analysis of ligand–free AK_{col} [146, 147] and the crystal structures of the conformational substates of *A. aeolicus* along this pathway towards the closed form have shown the changes in these two specified regions along the reaction pathway [123]. We have performed the NMA study to check the dynamics of these domains and also to find out whether the metal atoms have any effect in the dynamic motion of the LID domain. The lowest frequency mode calculated using the EL NEMO server for NMA analysis [148] shows 48 % of this mode to the direction towards the closed

conformation of the enzyme (**Fig. 7**). We found out that in all structures LID domain shows the same directionality. The largest distance fluctuations for the residues have found in the LID domain and AMP binding region. These findings confirm that the LID domain can move as a rigid body during catalysis without getting affected by the presence of the metal ion.

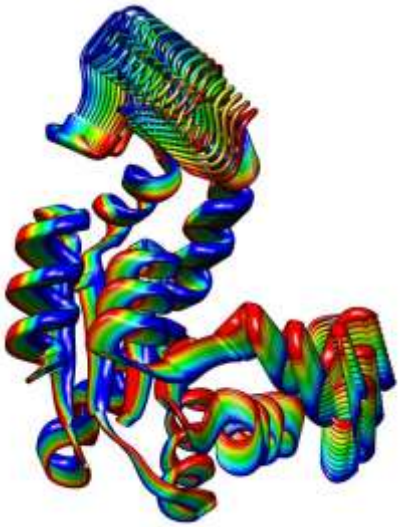

Fig. 7 Lowest frequency mode from the NMA showing the dynamic fluctuation of the LID domain along the reaction pathway

Structural comparison with other AK

So far several crystal structures of AK have been reported from several other organisms. A comparison of Zn^{2+}-AK_{gig} with members of each family of AK shows, as expected, that it has more similarities with those that harbour metal atoms in the LID domain. The CORE domain is strikingly similar in all the structures. The topology of the LID domain and AMP binding region shows most resemblances with the structures of enzymes that are devoid of any substrate. A search in the DALI server [149] revealed the human AK isoform 2 (2c9y pdb code) as the closest structure available in the PDB. This AK also belongs to the long LID domain group. Since all three structures have very similar overall structures, we will use only Zn^{2+}-AK_{gig} in the following discussion. Zn^{2+}-AK_{gig} and human AK isoform 2 (AK2) share 28 % sequence identity and their superposition yields an rmsd of 2 Å (**Fig. 8**). The main difference of these two AK isoforms is the lack of metal atom in the LID domain. Human AK2 enzyme also belongs to the long form. The superposition of the CORE domains of these two protein structures indicates similar secondary structure, but there is a significant change in the conformation of the LID domain. Since AK2 has a substrate bound, the LID domain is in the closed conformation. Superposition of the LID domains shows these are highly homologous apart from the metal binding region. Instead of the three cysteines and histidine residues that are present in Zn^{2+}-AK_{gig}, AK2 has arginine, histidine, aspartate and threonine that are incapable of metal binding. These four

residues are involved in a strong hydrogen bond network that holds the LID domain together. Comparison of the Zn^{2+}-AK_{gig} with the apo-form of AK from *E. coli* also shows similarities between the two structures. The CORE and AMP binding region have almost similar secondary structure features. As expected, the LID domain of the Zn^{2+}-AK_{gig} is in a more open conformation due to the strong crystal packing interactions and has a different topology due to the presence of the metal ion.

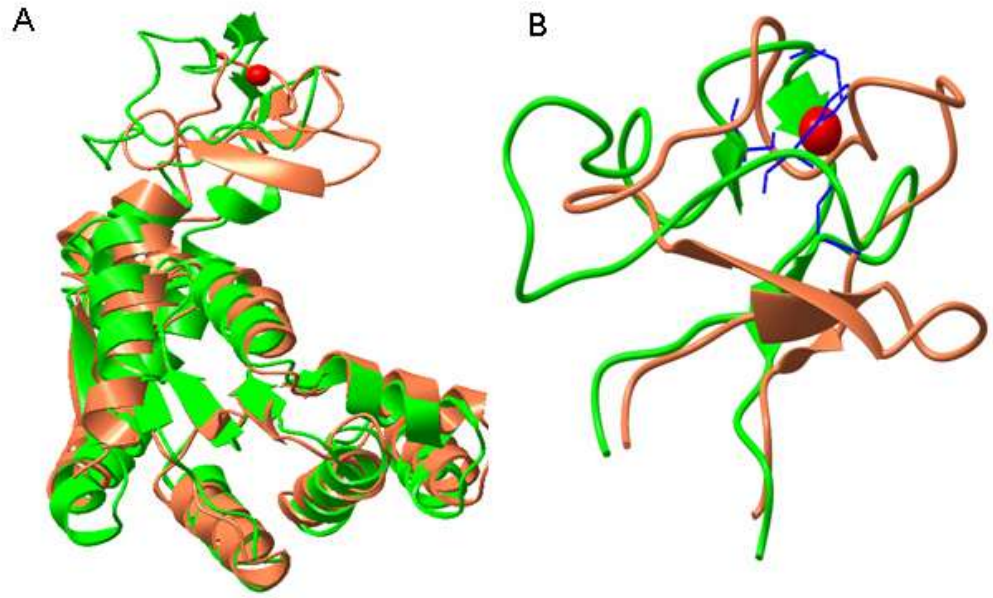

Fig. 8. (A) Superposition of Zn^{2+}-AK_{gig} (green) and human AK2 (coral). (B) Superposition of the LID domain of Zn^{2+}-AK_{gig} and human AK2.

Three other structures of AK from Gram-negative bacteria have been reported. They are from *Aquiflex aeolicus* (AK_{aeol}) [123], *Methanococcus voltae* (AK_{vol}) [14] and *Sulpholobus acidocalduris* (AK_{ac}) [132]. But none of them have metal atom in their LID domain. Both *M. voltae* and *S. acidocaldirus* are distantly related to the other adenylate kinases. Both *M. voltae* and *S. acidocaldirus* AK are distantly related to the other AK. They are trimeric in solution, and contain a central beta sheet and a short LID domain. Therefore, only a comparison study with the enzyme from *A. aeolicus* was performed. The structure of the apo-form of AK from *A. aeolicus* (AK_{aeol}) showed three molecules in the asymmetric unit, each with a different conformation of the LID domain. Superposition of Zn^{2+}-AK_{gig} with AK_{aeol} in the most open conformation yields an rmsd of 2.18 Å (Cα atoms) (**Fig. 9**). These proteins share 34 % sequence identity. Both of them have the walker motif, G-X-X-G-X-G-K-, present in the N terminal region of the enzyme. A 4 residue long structural motif -G-F-P-R- is present in their CORE domain. The arginine residues (Arg126 and Arg 164) in the hinge are also present in the both structures. The distance between Cα atom of one of the arginine residues present in the hinge and Cα atom of one of the glycine residues from the Walker motif of CORE domain can be considered as the extent of

opening of the LID domain. The arginine residues of the hinge and the Walker motifs are conserverd in almost all AK with long LID domain.

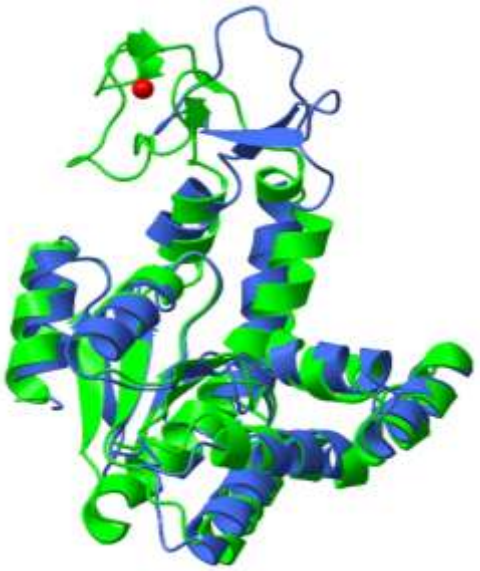

Figure 9. Superposition of Zn^{2+}-AK_{gig} (green) and apo form of *A. aeolicus* (light blue).

The topology of the LID domain is also different in Zn^{2+}-AK_{gig} where two reverse turns allow the zinc binding residues to be placed at the correct positions. The AMP binding regions of the CORE domain are very similar. The LID domain in the substrate bound structure of AK_{aeol} in the closed conformation and the distance between the LID and CORE domain is 10.58 Å whereas in open conformation they are 15.37 Å apart. The "hinge" arginine residues (Arg126 and Arg 164) have almost 5 Å towards the substrate, accompanied by the the LID domain. The AMP binding domain (corresponding residues 31-65 in Zn^{2+}-AK_{gig}) is also in close conformation in the substrate bound form of AK_{aeol} than AK_{gig}.

We also compared the structural features of Zn^{2+}-AK_{gig} with other zinc containing AK from Gram-positive bacteria. From the structures we have examined, to perform a comparison study we have chosen the AK from *Basillus globisporus* (AK_{glo}) [13], *Bacillus subtillis* (AK_{sub}) and *Bacillus stearothermophillus* (AK_{ste}). Like the AK_{gig} these also have the LID domain and the AMP binding domain that close during the time of catalysis. The secondary structures of them are very similar in spite of the fact that the sequence identity is only ~30 % and presence of different zinc-binding sites (**Fig. 10**).

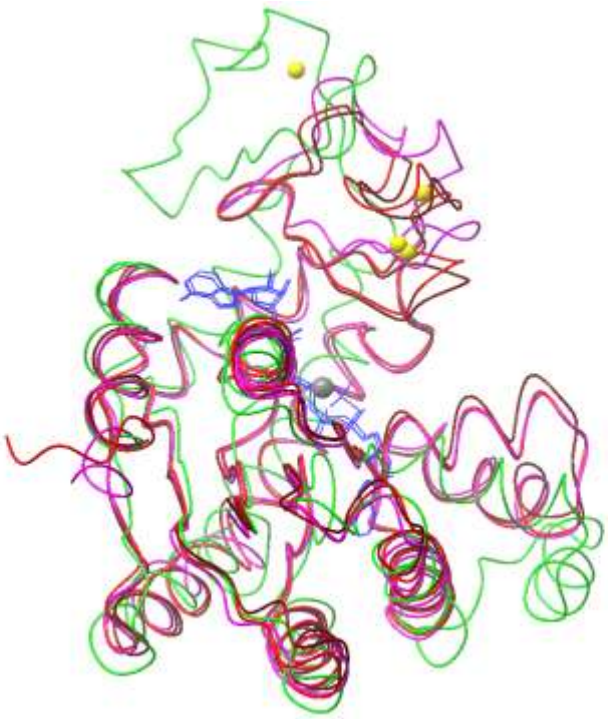

Fig. 10. Superposition of four structures of AK_{gig} (green), AK_{glo} (red), AK_{ste} (magenta) and AK_{sub} (brown), respectively.

Like AK_{glo} and AK_{sub}, in Zn^{2+}-AK_{gig} the zinc atom is also bound to 3 Cys and one other residue. All these enzymes share almost identical secondary structures in the CORE domain. The main difference is, apart from Zn^{2+}-AK all other enzymes were crystallized with AMP. So as expected, Zn^{2+}-AK_{gig} has indeed the LID and AMP binding domains are in fully open conformation as compared to the other three enzymes (**Fig. 10**). The equivalent regions to residues 31-65 in the other three AK bind to the AMP and come closer to the CORE domain in a closed confirmation. Due to the absence of substrate, the LID domain in AK_{gig} is also more open than these three structures. Nevertheless, the topology of the LID domain is very similar. All of them have these two reverse turns, a characteristic feature of the zinc containing AK from Gram-negative bacteria [23] to facilitate the zinc coordination. The corresponding arginine residues (Arg 124 and Arg 166) in these three enzymes also have almost 4 Å shift in the substrate bound condition compare to Zn^{2+}-AK_{gig} and as a consequence the shift in the LID domain towards close conformation (**Fig. 10**).

Chapter 5

Purification, crystallization and preliminary X-ray diffraction analysis of adenosine triphosphate sulfurylase (ATPS) from the sulfate-reducing bacterium *Desulfovibrio desulfuricans* ATCC 27774

This chapter was published as:

Olga Yu. Gavel, Anna V. Kladova, Sergey A. Bursakov, João M. Dias, Susana Texeira, Valery L. Shnyrov, José J. G. Moura, Isabel Moura, Maria J. Romão and José Trincão.2008. Purification, crystallization and preliminary X-ray diffraction analysis of adenosine triphosphate sulfurylase (ATPS) from the sulfate-reducing bacterium *Desulfovibrio desulfuricans* ATCC 27774. Acta crystallographica. Section F, Structural biology and crystallization communications 64(Pt 7):593-5.

Abstract

Native Zn^{2+}/Co^{2+}-containing ATP sulfurylase (ATPS; EC 2.7.7.4; MgATP: sulfate adenylyltransferase) from *Desulfovibrio desulfuricans* ATCC 27774 was purified to homogeneity and crystallized. The orthorhombic crystals diffracted to beyond 2.5 Å resolution and the X-ray data collected should allow the determination of the structure of the zinc-bound form of this ATPS. Although previous biochemical studies of this protein indicated the presence of a homotrimer in solution, a dimer was found in the asymmetric unit. Elucidation of this structure will permit a better understanding of the role of the metal in the activity and stability of this family of enzymes.

1. Introduction

ATP sulfurylases (ATPS; EC 2.7.7.4; MgATP:sulfate adenylyltransferases) are ubiquitous enzymes that catalyze the transfer of the adenylyl group from ATP to inorganic sulfate, yielding adenosine-5'-phosphosulfate (APS) and pyrophosphate (PP_i), MgATP + $SO_4^{2-} \leftrightarrow MgPP_i$+ APS. The APS produced in this reaction has a high-energy mixed phospho– sulfo anhydride bond that is used for sulfate activation and reduction in the cell.

ATPS are widely distributed in nature and have been found in virtually all types of organism [51, 150] since they were first characterized [151, 152]. Several different physiological roles have been proposed for ATPS in different species [50, 69], including sulfate assimilation, sulfate reduction and pyrophosphate recycling.

Two completely different unrelated types of ATP sulfurylase have been distinguished: heterodimeric [51] and monomeric or homooligomeric ATP sulfurylase, with molecular weights ranging from 38 to 69 kDa per monomer [75, 76]. The size variations arise from APS kinase or PAPS-binding allosteric domains residing on the same polypeptide chain [50, 67, 69, 75, 76].

The ATP sulfurylase from *Desulfovibrio desulfuricans* ($ATPS_{des}$) and *D. gigas* ($ATPS_{gig}$) were identified for the first time as Co^{2+}/Zn^{2+} containing metalloproteins [97]. Both enzymes were purified as homotrimers, with monomeric molecular weights of ~47 kDa and ~49 kDa, respectively.

Several crystal structures of ATP sulfurylase have been reported, including those of hexameric ATP sulfurylase from *Pn. chrysogenum* [81, 90] and *S. cerevisiae* [70, 71, 153, 154], dimeric ATPS from *Riftia pachyptila* [155] and *T. thermophilus* HB8 [87, 156] and the human dimeric ATPS–APS kinase complex PAPS synthetase [65]. All these ATP sulfurylases, with the exception of that of *S. cerevisiae* [70, 154], were crystallized from proteins cloned and expressed in *E. coli*.

The structure of the dimeric ATP sulfurylase from *T. thermophilus* HB8 ($ATPS_{th}$) showed the presence of one zinc ion per subunit [87]. The structure revealed that the zinc is distant from the active site and is close to the dimer interface, suggesting that it plays a structural role, possibly in multimerization of the enzyme. Sequence alignment of ATPS from *D. desulfuricans*, *D. gigas* and *T. thermophilus* suggests a similar role for the metal in these proteins. This would indicate that $ATPS_{des}$ and $ATPS_{gig}$ could also exist and function as dimers. In $ATPS_{th}$, the metal is coordinated by three cysteine residues and a histidine, all of which are conserved in the *Desulfovibrio* strains.

Here, we report the purification, crystallization and X-ray characterization of the native zinc-containing form of ATPS from *D. desulfuricans* ATCC 27774. Diffraction data were collected to

2.5 Å resolution. These data will allow the determination of the structure of the zinc-bound form of ATP sulfurylase from *D. desulfuricans* ($ATPS_{des}$). The structure will help to elucidate the role of the metal, as well as provide some insights on how cobalt/zinc selection might affect the activity and stability of the protein.

2. Materials and methods

2.1. Purification

D. desulfuricans ATCC 27774 cells were grown under anaerobic conditions in the medium described by Liu & Peck (1981) using nitrate as a terminal electron acceptor [5]. Cells were harvested at the beginning of the stationary phase and were resuspended in 10 mM Tris/HCl buffer pH 7.6 containing 1 mM PMSF at a ratio of 1:1(w:v). The cells were lysed using a French press (62 MPa). The extract was centrifuged at 15 000g for 65 min and then at 180 000g for 75 min in order to eliminate the membrane fraction. The purification procedure was adapted from that published previously [97] and included four chromatographic steps: ion exchange on DEAE-52 cellulose and Source 15Q (Pharmacia), molecular-weight exclusion on Superdex 200 (Pharmacia) and adsorption chromatography on hydroxyapatite (BioRad). All purification procedures were performed aerobically at 277 K. Specific activities were determined at each step in the purification process [97]. The purity of the final preparation of $ATPS_{des}$ and subunit identification were confirmed by SDS–PAGE and N-terminal sequencing. The active $ATPS_{des}$ exhibited specific activities of 22.5±0.8 units mg^{-1} in the reverse direction and 28.9±0.8 units mg^{-1} in the forward direction (as determined by molybdolysis). Metal analysis (determined by ICP analysis performed on a Jobin–Yvon (Ultima) instrument) indicated the presence of approximately one metal atom per subunit. ATPS was aliquoted at a final protein concentration of 10 mg ml^{-1} in 10 mM Tris/HCl buffer pH 7.5 and was stored at 190 K for initial crystallization trials.

2.2. Crystallization, data collection and processing

Crystallization trials of the $ATPS_{des}$ were performed using the hanging-drop vapour-diffusion method using 2 µl drops (with a protein:well solution ratio of 1:1) over a well containing 700 µl well solution. Initial crystallization conditions were screened using an inhouse modified version of the sparse-matrix method of Jancarik & Kim (1991) in combination with the commercial Crystal Screen and Crystal Screen 2 from Hampton Research (California, USA) at 277 and 293 K. Crystallization conditions were improved by screening additives and varying the protein and precipitant concentrations.

Multiple data sets were collected either on an in-house Cu K_α rotating-anode generator or at the European Synchrotron Radiation Facility (ESRF, Grenoble, France). Crystals were flash-cooled directly in liquid nitrogen and stored or transferred to a gaseous nitrogen stream (100 K) using Paratone oil as a cryoprotectant. The best data set was collected on beamline ID14-3 at the ESRF using an ADSC Quantum-4R detector. The data were processed using *MOSFLM* v.7.0.1 and *SCALA* from the *CCP4* package v.6.0.2 [126].

3. Results and discussion

$ATPS_{des}$ was purified to homogeneity and crystallized. The best crystallization conditions were 3 M ammonium sulfate, 100 mM Tris/HCl pH 7.5 with 10%(v/v) MPD as an additive (the protein:well solution:MPD ratio was 1:1:0.2 and the final drop volume was 2.4 µl) using a protein concentration of ~10 mg ml^{-1} at 277 K. Crystals grew to dimensions of about 0.2×0.1×0.05 mm (**Fig. 1**). The crystals diffracted to beyond 2.5 Å resolution (**Fig. 2**) and belong to space group $C222_1$, with unit-cell parameters a = 110.1, b = 126.2, c = 155.0 Å. A full 180° data set was collected, with 1° oscillation per image. The X-ray data collected on beamline ID14-3 (ESRF) were almost 100% complete to 2.45 Å but had to be cut to 2.8 Å in order to ensure high data quality (data-collection statistics are presented in **Table 1**).

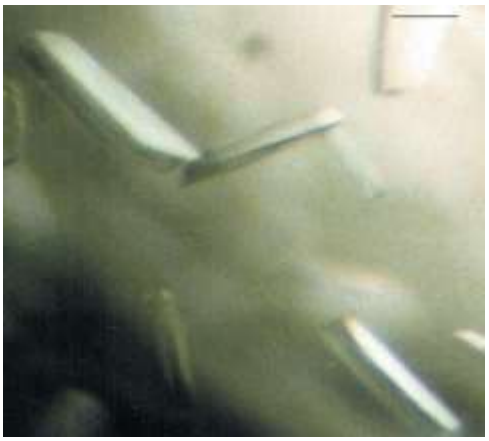

Figure 1 Crystals of D. desulfuricans ATPS (the scale bar is 0.1 mm in length).

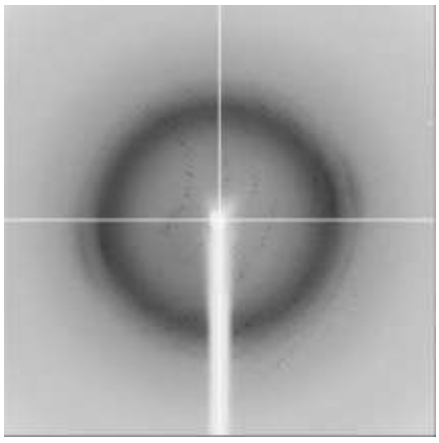

Figure 2 Diffraction pattern of the ATPS crystal (the resolution at the edge is 2.45 Å) obtained on beamline ID14-3 (ESRF).

Table 1. Data collection statistics. Values in parenthesis are for the highest resolution shell.

Values in parentheses are for the highest resolution shell.	
X-ray source	ID14-3 (ESRF, Grenoble)
Crystal data	
Crystal system	Orthorhombic
Unit-cell parameters (Å)	a = 110.1, b = 126.2, c = 155.0
Maximum resolution (Å)	2.8
Mosaicity (°)	1.1
Molecules per ASU	2
Matthews coefficient ($Å^3$ Da^{-1})	2.83
Data collection and processing	
Space group	C2221
Resolution limits (Å)	30–2.8 (2.95–2.8)
Wavelength (Å)	0.934
No. of observed reflections	189690 (27399)
No. of unique reflections	26876 (3853)
Redundancy	7.1
R_{merge}† (%)	0.154 (0.541)
Completeness (%)	99.9 (99.9)
$\langle I/\sigma(I) \rangle$	4.9 (1.4)

† $R_{merge} = \frac{\sum_{hkl} \sum_i |I_i(hkl) - \langle I(hkl) \rangle|}{\sum_{hkl} \sum_i I_i(hkl)}$, where $I_i(hkl)$ is the intensity of the measurement of reflection *hkl* and $\langle I(hkl) \rangle$ is the mean value of *I(hkl)* for all *i* measurements.

Although the early biochemical studies indicated the presence of a homotrimer in solution [97], the calculated Matthews coefficient is 2.83 $Å^3$ Da^{-1} [127], suggesting the presence of a dimer in the asymmetric unit, as predicted by sequence comparison with $ATPS_{th}$ and the structure of this enzyme. The selfrotation function (calculated using *POLARRFN*; [126]) exhibited clear peaks at $\kappa = 180°$, whereas no peaks were observed at $\kappa = 120°$ (data not shown), further supporting the presence of a dimer.

A preliminary structure solution has been obtained using *BALBES* [157], which used PDB entries 1jhd (*R. pachyptila*; [155], 1v47 (*T. thermophilus* HB8; [87] and 1r6x (*S. cerevisiae*; [71]

as search models (1v47 yielded the best solution). The solution found indicated the presence of a dimer in the asymmetric unit and the phases obtained yielded an interpretable map for at least 60% of the protein. The remainder of the protein still has poor density. A model is being built manually using *Coot* [139].

Acknowledgments

This work was supported in part by Fundacão para a Ciência e Tecnologia project POCI/QUI/59119/2004, by CRUP project E-62/06 and FCT grants SFRH/BPD/28380/2006 (OYuG) and SFRH/BD/24744/2005 (AVK). We also thank Carla Rodrigues for excellent technical help with ICP-AES (inductively coupled plasma-atomic emission spectroscopy) analysis.

Chapter 6

Structural stability of ATP sulfurylase (ATPS) from sulphate-reducing bacteria *Desulfovibrio desulfuricans* ATCC 27774

This chapter was prepared for publication as:

Sergey A. Bursakov, Olga Yu. Gavel, Anna V. Kladova, Laura S. Zamorano, Juan J. Calvete, Galina G. Zhadan, José J.G. Moura, Valery L. Shnyrov. 2010. Structural stability of ATP sulfurylase (ATPS) from sulphate-reducing bacteria *Desulfovibrio desulfuricans* ATCC 27774.

Abstract

ATP sulfurylase (EC 2.7.7.4. MgATP:SO_4^{2-} adenyltransferase) from *Desulfovibrio desulfuricans* ATCC 27774 ($ATPS_{des}$) was extensively purified and sequenced. The $ATPS_{des}$ has a single polypeptide chain of 423 amino acids in length and reveals high homology with many other bacterial ATP sulfurylases. The structural stability of $ATPS_{des}$ has been characterized by high-sensitivity differential scanning calorimetry, circular dichroism, steady-state tryptophan fluorescence. It has been shown that the thermal denaturation process is the irreversible, involving a highly cooperative transition between the native and denatured dimers with Arrhenius activation energy of around 105 kcal per mol. The process is strongly dependent upon the scan rate, suggesting that it is under kinetic control. Analysis of the kinetic parameters of the $ATPS_{des}$ denaturation was accomplished on the basis of the simple kinetic scheme: $N_2 \xrightarrow{k} D_2$, where *k* is a first-order kinetic constant that changes with temperature, as given by the Arrhenius equation; *N* is the native state, and *D* is the denatured state.

Introduction

ATP sulfurylases (EC 2.7.7.4. MgATP: SO_4^{2-} adenylyltransferase) are ubiquitous enzymes that catalyze the transfer of the adenylyl group from ATP to inorganic sulphate, yielding adenosine-5´-phosphosulphate (APS) and pyrophosphate (PPi):

$$MgATP + SO_4^{2-} \rightleftharpoons MgPP_i + APS$$

ATP sulfurylases are widely distributed in nature and play several different roles. Its certain kinetic properties are optimized for the physiological direction [50, 69].

Three different types of physiological reactions are known in which ATP sulfurylase is involved: catalysis of the first intracellular reactions in the assimilation of sulphate into reduced organic molecules through adenosine-5´-phosphosulphate (APS) or 3´-phosphoadenosine-5´-phosphosulphate (PAPS); formation of APS solely to serve as the terminal electron acceptor of heterotrophic metabolism; pyrophosphorolysis of APS recognised as the terminal step in the overall oxidation of reduced inorganic sulphur compounds to sulphate in the opposite direction of ATP sulfurylase reaction. The APS produced has a high-energy mixed phosphoric-sulphuric acid anhydride bond that is used for sulphate activation and reduction in the cell.

Some of ATP sulfurylases are part of a bifunctional polypeptide chain associated with APS kinase or with APS kinase and pyrophosphatase forming multidomain complex [56, 158]. It appears that as isolated from different sources, this family of enzymes is fairly heterogeneous in terms of amino acid sequences, molecular mass, subunit composition and behaviour.

ATP sulfurylases have been partially or extensively purified and characterized from a wide variety of sources. The molecular masses of native ATP sulfurylases vary with the species, which have different structural organizations. Two completely different, unrelated types of ATP sulfurylases can be distinguished:

- The heterodimeric type, which occurs exclusively in sulphate-assimilating prokaryotes, e.g. in *E. coli* K-12 (two subunits with masses of 23 and 53 kDa) [51], in *Mycobacterium tuberculosis* (35 kDa and 68 kDa) [74], *Acidithiobacillus ferrooxidans* [159] nodulating, and some other bacteria [51];

- All other ATP sulfurylases characterized in sufficient detail are monomers or homooligomers, with a range of molecular masses of 38–69 kDa per subunit [75, 76].

Several ATP sulfurylases as for example from thermophylic *A. aeolicus, P. duponti, T. thermophilus* HB8 and *A. fulgidus* have high thermal stability. While no universal rules can be found that explain protein thermal stability. ATP sulfurylase from thermophilic organisms has some specific properties that can be identified in comparison to the mesophilic homologs.

The oligomerization as well as presence of cofactor can serve also as factors of additional thermostability. Besides of the presence bifunctional enzymes, recently novel triple fusion protein of ATPS, APS-kinase and pyrophosphotase found in several protozoan genomes within the Stramenopile lineage [56]. They show also that triple complex more active than bi complex.

The thermal stability of the enzyme can be also enhanced to varying degrees in the presence of metal ions. ATP sulfurylases from mesophilic *D. desulfuricans* and *D. gigas* were identified, for the first time, as metalloproteins containing cobalt and zinc [97]. Cobalt and/or zinc in ATP sulfurylases from *Desulfovibrio* species are alternatively coordinated at the same metal-binding site and ligated with one imidazole nitrogen of histidine and three cysteine sulphur atoms [97].

The crystal structure of dimeric ATP sulfurylase from *T. thermophilus* has been resolved [87] and demonstrates the presence of zinc ions (one per subunit) that are tetrahedrally coordinated by three sulphur atoms of cysteines and the nitrogen atom of histidine in a motif ^{295}Cys-X_2-Cys-X_8-Cys-X_3-His [87]. This finding is in good agreement with the postulated metal-binding site for $ATPS_{des}$ [97]. The structure of *T. thermophilus* ATP sulfurylase suggests that deletion of two residues present between the third cysteine and the histidine will not affect the chelation of the metal ion.

In contrast to cadmium in *Sc. cerevisiae* ATP sulfurylase [70], zinc ions in the *T. thermophilus* ATP sulfurylase are not bound on the surface of enzyme subunit. The zinc-binding region is a hinge between catalytic domain II and domain III, and seems to be involved in protein-protein interactions in the ATP sulfurylase of *T. thermophilus* [87]. Zinc is distant from the active site and apparently does not play any role in the catalysis. The authors hypothesize that the ATP sulfurylase from thermophilic bacteria acquire thermostability by chelating zinc ions.

Because no available information about thermostability of the ATP sulfurylase during storage or catalysis and metals involvement, concerted studies addressing the preparation of apo-enzymes, site directed mutagenesis of metal-binding sites, and high-resolution crystallographic structure determination are required. Besides of scientific interest high output of this knowledge can lead for many applications in biotechnology, biochemistry or molecular biology.

Therefore, the object of this study is to establish thermodenaturation mechanism of $ATPS_{des}$ and gain further insight into the role of metal ion (cobalt and zinc) in protein stability using different physicochemical techniques.

Materials and methods

Protein purification.

The *D. desulfuricans* ATCC 27774 cells were grown under anaerobic conditions in the medium described by Liu and Peck [5]. The cells treatment and purification procedure were adapted from one published previously [97]. All purification procedures were performed aerobically at 4 ºC, and specific activities were determined after each purification step. The purity of the final preparation and subunits identity were confirmed by polyacrylamide gel electrophoresis and N-termini sequencing. The active $ATPS_{des}$ with specific activities 22.5 ± 0.8 units/mg in the reverse direction, and 28.9 ± 0.8 units/mg in the forward direction (molybdolysis) was distributed in small aliquots of 50 µl with a protein concentration of 10 mg ml^{-1} in 10 mM Tris⁄HCl buffer pH 7.5 and was stored at -70 ºC.

Molecular mass and purity determination.

The purity and subunit composition of ATPS were determined by 12.5 % (w/v) SDS-PAGE with Bio-Rad standards. The molecular mass of the purified native $ATPS_{des}$ was determined by gel filtration using a Superdex 200 column with Pharmacia standards and also estimated by amino acid composition analysis.

The molecular mass of the pure protein was determined by MALDI-TOF mass spectrometry (MS) using an Applied Biosystems Voyager-DE Pro mass spectrometer operated in linear mode. To this end, equal volumes (0.5 µl) of the protein solution and the matrix (sinapinic acid (Sigma) saturated in 50 % acetonitrile and 0.1 % trifluoroacetic acid) were mixed onto the MALDI-TOF plate. The mass calibration standard consisted of a mixture of the following proteins, whose isotope-averaged molecular mass in Daltons are given in between brackets: bovine insulin (5734.6), *E. coli* thioredoxin (11674.5, horse apomyoglobin (16952.6), *E. coli* N-acetyl-L-glutamate kinase (27159.5), *Pyrococcus furiosus* carbamoyl-phosphate synthetase (34297.4), *Parkia platycephala* seed lectin (47946.6), and bovine serum albumin (66431.4).

Protein assay.

Protein determination was performed colorimetrically according to bicinchonic acid method using a Pierce kit (Protein Assay Reagent; Thermo scientific), with bovine serum albumin as the standard.

Metal analysis.

Zinc and cobalt levels were determined chemically as indicated in reference [160, 161], respectively, by atomic absorption spectroscopy (Perkin-Elmer 1313, furnace 4100 ZL) and as well by inductively coupled plasma emission analysis.

Activity assays.

$ATPS_{des}$ activities were measured by continuous coupled spectrophotometric assays [97]. $ATPS_{des}$ activity for optimum pH determination was made in reverse direction by stop (end-point) reaction assay method [75] using bioluminescence kit HS II (Boehringer Mannheim). All assays were conducted at 30 °C in Tris/HCl buffer, pH 8.0. In all cases, activity is expressed in units per milligram of the protein where one unit is equivalent to the formation of 1 µmol of primary product per minute.

Protein sequencing

N-terminal sequencing. The N-terminal sequence was determined by automated Edman degradation of desalted sample (125-200 pmol) of $ATPS_{des}$ in an Applied Biosystem 120 analyzer model 477, following the manufacturer's instructions.

C-terminal and internal peptides sequencing.

Sample for C-terminal sequencing was prepared in 0.1% TFA/water and adsorbed onto a ProSorb filter. Lysine side chains were modified with 5 µl PIC/ACN (200 mM) under basic conditions (124 mM DIEA/ACN).

Proteolytic digestion of $ATPS_{des}$ (5 mg/ml) was performed with endoproteinase Lys-C by splitting peptide bonds at the carboxyl side of lysine residues at an enzyme:substrate ratio of 1:50 (by mass) followed in 25 mM Tris/HCl buffer pH 8.5, 1 mM ethylenediamine N,N,N tetraacetic acid (EDTA) at 37 ºC during 18 hrs. Resulting peptides were purified by reverse-phase to eliminate presence of low molecular weight molecules. Mass spectrometry MALDI-TOF and amino acid sequencing equipment, including ESI/MS MS/MS (QTrap instrument) were used for analysis.

Cleavage of $ATPS_{des}$ (10 mg/ml in 70 % (v/v) formic acid) at methionine residues was performed with cyanogen bromide (100 mg/ml final concentration) for 4 h at room temperature, in the dark, under a nitrogen atmosphere. The reaction mixture after neutralization with 10 M NaOH (1:5) was then diluted with Milli-Q water and lyophilized.

Peptides were isolated by reverse-phase HPLC on Lichrosorber RP-100 (Merck) column (25 × 0.4 cm, C_{18}, 5-mm particle size) eluting at 1 ml/min with a gradient of 0.1 % (v/v) trifluoroacetic acid in (A) water and (B) acetonitrile, following the absorbance at 220 nm and sequenced by automated Edman degradation.

Sequencing of plasmidic DNA.

The sequencing reactions were done in an Amersham Pharmacia ALF express II automated sequencer using standard protocol.

Molecular cloning and DNA sequencing.

The degenerated forward oligonucleotide primer AT3 (5'-GARAARTTYGARATGAC-3') and the degenerated reverse primer AT4 (5'-ATYTCYTGVGCYTCRAACAT-3') (where R=A+G, V=G+A+C, Y=C+T), were designed and used to amplify a specific region of the gene of interest by PCR. Redundancy of the primers was reduced based upon the codon frequency observed in other proteins from the same bacteria. DNA fragment coding $ATPS_{des}$ was amplified by PCR on the thermal cycler from Biometra with the following program: 1 cycle of 5 min at 94 ºC; 29 cycles where the temperature was for 2 min at 94º C, 1 min at 46.5 ºC and 3 min at 72 ºC. The last step was of 5 min at 72 ºC. The reaction product with 601 bp was isolated and sequenced.

Two pairs of the primers was designed for use with Universal GenomeWalker Kit™ (Clontech) forward GSP1C (5'-CTTCCGTCAGAACTACGGCATCAACAA-3') and GSP2C (5'-CGACCACGCCGGTGTGGGCGACTTCTA-3') for the C-termini and reverse GSP1N (5'-GAATTCGCCCTGCGAGAGAGCACTTTGAC-3') and GSP2N (5'-CGATATTGTATTCTTTCTGGGCCAGAAC -3') for the N-termini. The GenomeWalker DNA walking protocol consists of eight primary and secondary PCR amplifications of four experimental libraries prepared base on genomic DNA. Temperatures used during PCR amplification were for the primers of GSP1C/GSP2C (73 ºC, 68 ºC) / (76 ºC, 71 ºC) and for GSP1N/GSP2N (77 ºC, 72 ºC) / (72 ºC, 67 ºC) and number of cycles – 37.

The reaction product was isolated from 1 % agarose gel and fragment purified with a QIAquick Gel Kit Extraction protocol (QIAGEN) and ligated overnight at 4 ºC into the pGEM-T Easy Vector, following Promega's protocols and its applications guide. The cloning vector was subsequently transformed into the Epicurian Coli XL1-Blue ultracompetent cells (Stratagene), pre-grown in eppendorfs for 1 hr with SOC media and ampicillin (100 μg/ml). The plasmidic DNA was extracted with a common double stranded DNA miniprep protocol, and the insertion of the fragment into the plasmid was confirmed by digesting the template with the restriction enzyme EcoR1 (Promega). Finally, the recombinant clones were sequenced.

Differential Scanning Calorimetry.

The calorimetric experiments were performed on a MicroCal MC-2D differential scanning microcalorimeter (MicroCal Inc., Northampton, MA) with cell volumes of 1.22 ml, interfaced with a IBM-compatible personal computer, as described previously [117]. Scan rates in the range of 0.5-1.5 K/min were employed. Before measurement, sample and reference solutions were degassed in an evacuated chamber for 5 min at room temperature, and carefully loaded into the cells to avoid bubble formation. Exhaustive cleaning of the cells was undertaken

before each experiment. An overpressure of 2 atm of dry nitrogen was maintained over the sample solutions throughout the scans to prevent any degassing during heating. A background scan collected with a buffer in both cells was subtracted from each scan. Reversibility of the thermal transition was checked by performing the scan a second time, immediately after the sample had cooled subsequent to the first scan. The experimental calorimetric traces were corrected for the effect of instrument response time [162]. The excess heat capacity functions were plotted after normalization (M = 46900 g/mol of monomer) and chemical baseline subtraction using the Windows-based software package (Origin) supplied by MicroCal.

Spectroscopic methods.

UV/Visible absorption data were recorded on a Shimadzu UV-2101 PC and Shimadzu UV-265 split-beam spectrophotometers using 1 cm quartz cells.

The CD spectra in the far-ultraviolet range were recorded on a Jasco-715 spectropolarimeter, using a spectral band-pass of 2 nm and a cell pathlengths of 1 mm. Protein concentrations were 0.1 mg/ml. Four spectra were scanned for each sample at a scan rate of 50 nm/min and were then averaged. All spectra were background-corrected, smoothed, and converted to mean residue ellipticity $[\Theta] = 10\ M_{res}\ \Theta_{obs}\ l^{-1}\ p^{-1}$, where M_{res} is the mean residue molar mass, Θ_{obs} is the ellipticity measured (degrees) at wavelength λ, l is the optical path length of the cell (dm), and p is the protein concentration (mg/ml). Secondary structure analysis of the CD spectra was performed using the SELCON software package [106]. To study the dependence of ellipticity on temperature, the samples were heated from 25 to 60 ^{o}C at a constant heating rate (ca. 1 K/min), using a NESLab RT-11 programmable water bath.

Steady-state fluorescence measurements were carried out on a F-4010 Hitachi spectrofluorimeter. The intrinsic fluorescence of proteins arises from the aromatic amino acid residues, so here we used the fluorescence of tryptophan residues available in the enzyme. A fluorescence excitation wavelength of 297 nm was used to avoid the contribution of the emission of residues other than tryptophan. The monochromator slit width was kept at 5 nm in the excitation and emission channels. Fluorescence measurements of the enzyme were carried out in protein solutions with an optical density of less than 0.2 at 297 nm in order to avoid the inner filter effect. The emission spectra were corrected for instrumental spectral sensitivity. The position of the middle of a chord drawn at the 80 % level of maximum intensity (λ_{max}) was taken as the position of the spectrum. The temperature dependence of the emission fluorescence spectra was investigated using thermostatically-controlled water circulating in a hollow brass cell-holder. Sample temperature was monitored with a thermocouple immersed in the cell under observation. The heating rate was 1.3 K/min, and spectra were collected at the desired

temperatures over the entire temperature range. In titration experiments, pH values were adjusted by means of a polyethylene rod moistened with either 0.1 M HCl or 0.1 M NaOH.

Results and discussion

SDS-PAGE of the pure $ATPS_{des}$ disclosed single dye-stained band with mobility corresponding to molecular mass of ~45 kDa. One single N-termini found confirm identity of present subunits.

Most of the ATP sulfurylases studied have identical subunit compositions with only a few exceptions and can be structured depends of the species as a monomeric [163], dimeric [164], tetrameric [86], and hexameric [72, 165].

Sequencing.

A complete amino acid and nucleotide sequences of $ATPS_{des}$ were obtained base on the chemical and molecular biology sequencing methods (EMBL/GenBank/DDBJ databases accession number: AM949034). The $ATPS_{des}$ has a single polypeptide chain of 423 amino acids in length that correspond to the 46.9 kDa per subunit.

Comparison of the primary structure of the $ATPS_{des}$ with known sequences reveals high homology with many other bacterial ATP sulfurylases (**Fig. 1**). The identity of the ATPS from *D. desulfuricans* with that from *Sc. cerevisiae*, *Pn. chrysogenum*, the *Riftia pahyptila* symbiont, *T. thermophilus,* and *Aquifex aeolicus* for which the 3-D structures available attains 34 %, 33 %, 39 %, 39 %, and 35 %, respectively. In spite of this, all contain highly conserved motifs that are involved in substrate binding and catalysis. Thus, the HXXH (binds the PPi group of ATP and MgPPi), QXRNP (binds the phosphosulphate group of APS and the β-phosphate of ATP) and GRD (binds sulphate and ribose groups of APS and SO_4^{2-}) motifs, and also the mobile loop (hp)3HXhpXGXXKXXDhpXXXXR (hp-hydrophobic residues) (**Fig. 1.**), which does not interact directly with substrate but instead orients residues that do bind the substrate in the ATPS.

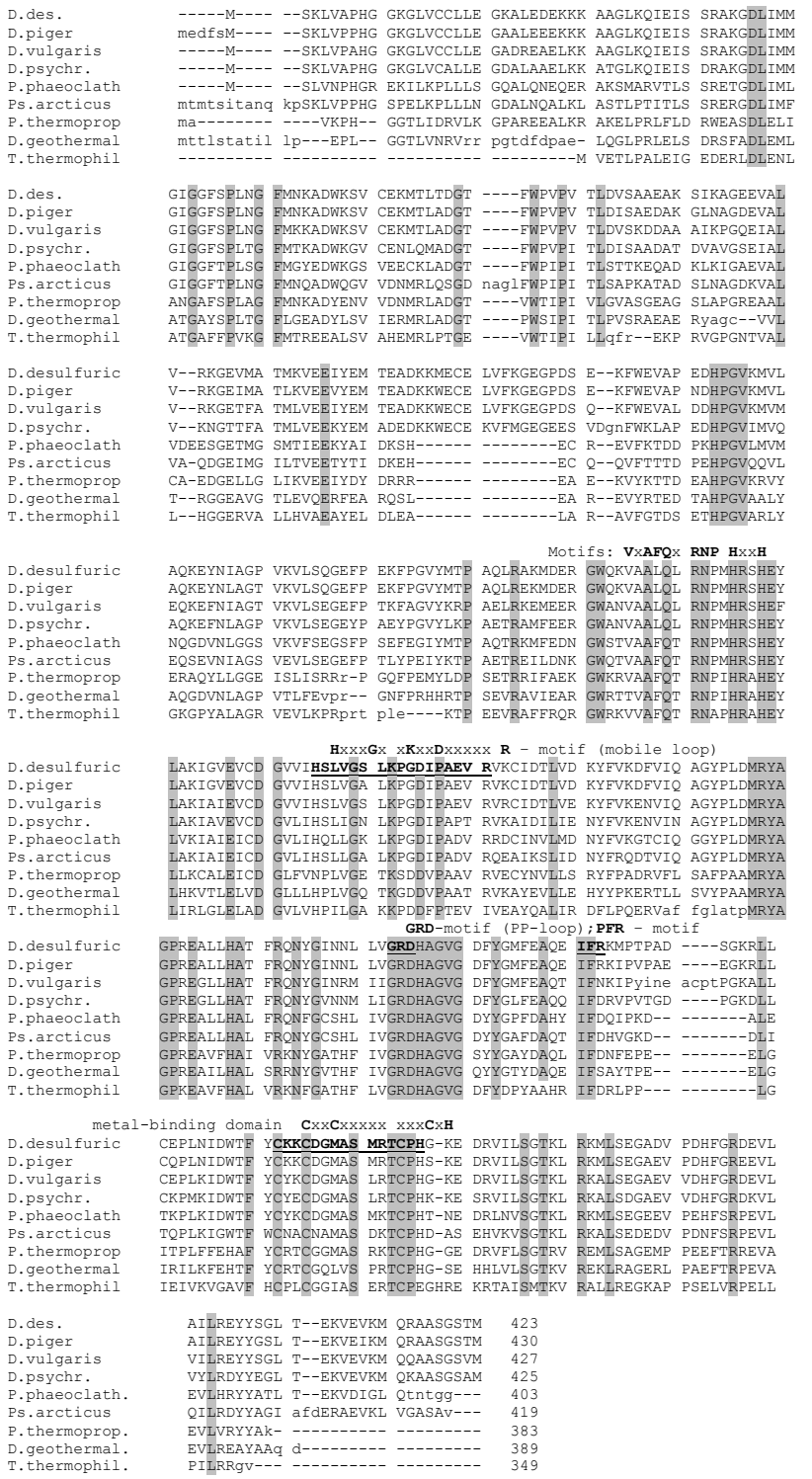

Fig. 1 Sequence alignment of ATPS$_{des}$ with mesophiles: *Desulfovibrio piger*, *Desulfovibrio vulgaris*, psichrophiles: *Desulfotalea psychrophila*, *Pelodictyon phaeoclathratiforme, Psychrobacter arcticus,* and thermophiles: *Pelotomaculum thermopropionicum*, *Deinococcus geothermalis, Thermus thermophilus.* The sequence identities between all are in grey.

The characterization of the ATPS from *D. desulfuricans* and *D. gigas* responsible for the activation of the sulphate molecule are key steps in the understanding of one of the ancient respiratory chains. Surprisingly, the enzymes from both *Desulfovibrio* strains were first identified as metalloproteins [97]. The sequence data show that tetra-coordinated cobalt or zinc is bound by most probably the nitrogen ^{363}His and three sulphur atoms ^{349}Cys, ^{352}Cys and ^{361}Cys. Alignment of homo-oligimeric ATPS sulfurylases (**Fig. 1**) exhibits the characteristic conserved Cys-X_2-Cys-X_8-Cys-$X_{(1-3)}$-His motif, which coincides with the proposed metal-binding site in the $ATPS_{des}$ [97]. We hypothesized that ATP sulfurylases having an analogous motif may capture metals. No similar metal binding sites and metals were seen in the *Penicillum* [81, 90] or *Riftia* ATP sulfurylases [155]. Thus, it appears that the cobalt or zinc present in *Desulfovibrio* species may maintain the structure of the ATP sulfurylases in the immediate vicinity of the metal site to keep the stability and integrity of the protein and its proper conformation.

The metal-binding site of both ATP sulfurylases from *D. desulfuricans* and *D. gigas* may be attributed to the structural site based on its geometric properties and the nature of the zinc and cobalt ligands. In general, structural zinc sites have four protein ligands with the sulphur of the cysteine residues as preferred ligands. The second most prevalent ligand is the imidazole nitrogen of histidine, which is often found in combination with cysteine sulphurs. Usually, catalytic zinc sites contain any three nitrogen, oxygen, and sulphur donors and metal-bound water molecule. In co-catalytic zinc sites two or three metal ions are closely grouped [166, 167].

Therefore, the zinc and cobalt ions in the ATP sulfurylases from *Desulfovibrio* strains seem to play a structural rather than catalytic role as well as zinc ion in the ATPS from *T. thermophilus* [97, 156]. The coordination chemistry of Co^{2+} is very similar to that of Zn^{2+}. Zinc or cobalt can be interexchanged in zinc proteins and they generally maintain of protein stability almost equally well and display comparable activities [168]. Cells do not have a strong preference for either, and metal availability as well as changes in the intracellular redox potential play a crucial role in the selection of the metal [169].

In the same time it is clear that metal binding site is present in all of bacterial group with different optimal temperature for maximal growth. Alignment of the known sequences of ATP sulfurylases has revealed that ATP sulfurylases from thermophilic bacteria such as *Archaeoglobus fulgidus, Pyrococcus abyssi,* and S*ulfolobus solfataricus* have a characteristic metal-binding motif. However, the Cys-X_2-Cys-X_8-Cys-X_{1-3}-His motif was also found in mesophiles and psychrophiles. So, zinc binding is not the only stabilizing feature in this case enhancing the thermal stability of ATP sulfurylases from thermophilic bacteria.

Therefore, we conclude that metal itself and metal binding site of the ATP sulfurylases does not influence directly to the thermostability of the protein. This site, most probably, is involved in interrelation between subunits and maintenance its correct conformation. This point strongly confirmed by X-ray structure of ATP sulfurylase from *T. thermophilus* [87].

Alignment of the ATP sulfurylases from different sources reveals interesting dependence between percent of homology and bacterial classification according to the optimum temperature of maximal growth. The most identical sequences of $ATPS_{des}$ can be found inside of the mesophilic group whereas it is fewer with psichrophilic and even less with thermophilic groups. The ratio of identity inside of ATP sulfurylases from mesophiles attains 92 %, in psichrophiles 73 % and thermophiles 60 %.

To gain insights on the basis of the above-described conformity of the $ATPS_{des}$ to the ATP sulfurylases from mesophilic group of bacteria we created a phylogenetic tree based on CLUSTALW alignments of the amino acid sequences of the $ATPS_{des}$ and a number of closest homologous. We also add to this tree ATP sulfurylases from *T. thermophilus* and *Aquifex aeolicus* for which the three-dimensional crystal structures have been determined. The results showed that represented ATP sulfurylases can be grouped with a few exceptions into three different clades dependent from the optimum of temperatures of maximal bacterial growth. $ATPS_{des}$ fall into the clade of ATP sulfurylases from mesophilic bacteria while clades of ATP sulfurylases of psichrophiles and especially thermophiles are located in the tree more distantly.

Additionally, from phylogenetic tree (**Fig. 2**) is clear that sequence of $ATPS_{des}$ is posted together with other ATP sulfurylases from mesophiles, whereas ATP sulfurylases from thermophiles or psychrophiles are located in different clades with just a few exceptions. At that point clade of psychrophiles ATP sulfurylases is situated more close in comparison to that of thermophiles.

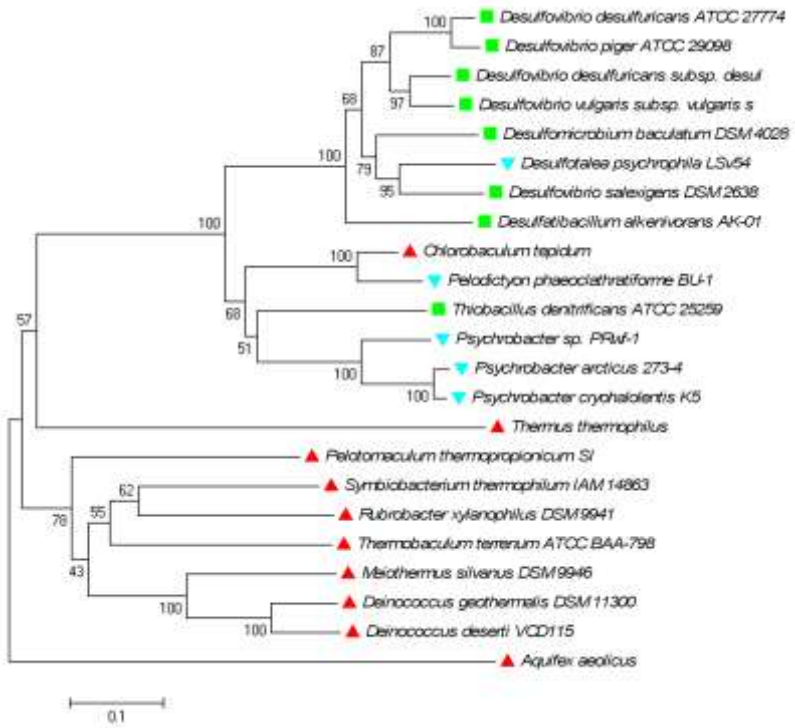

Fig. 2. Phylogenetic tree constructed with some closest amino acid sequences of homologous ATPS from mesophilic (■), psychrophilic (▼) and termophilic (▲) bacteria. Statistical significance of the respective interior nodes in bootstrap analysis is based on neighbour-joining tests and supported by 2,000 bootstrap runs.

pH Dependence of ATPS Intrinsic Fluorescence

To choose pH conditions most suitable for studies of ATPS structural stability, we have measured the pH dependence of tryptophan fluorescence for this enzyme **Fig. 3**.

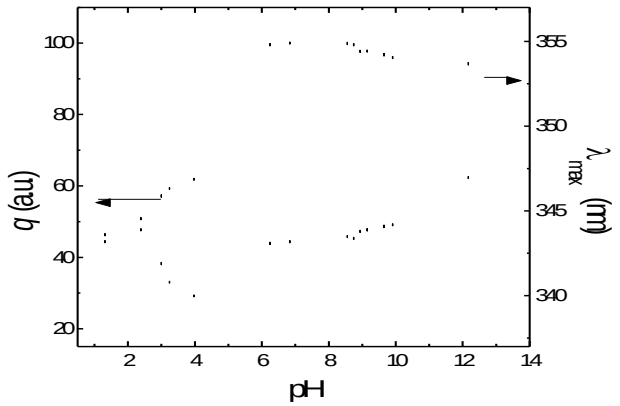

Fig. 3. pH-dependence of fluorescence parameters of ATPS at 25 °C. Measurements were performed in 20 mM universal buffer (CH_3COOH, H_3PO_4, H_3BO_3-NaOH) with a protein concentration of ca. 10 μM. The excitation wavelength was 296 nm. Open circles represent area under fluorescence spectrum (arbitrary units) which is proportional to fluorescence quantum yield, *q*, and closed circles correspond to the maximum of the fluorescence spectrum λ_{max}.

One of the most useful parameters of protein fluorescence spectrum is its maximum position (λ_{max}) that reflects polarity and mobility of the polar environment of emitting tryptophan residues in the protein and often reflects the degree of accessibility of the chromophores to solvent molecules [170]. As it is clear seen from **Fig. 3**, λ_{max} remains constant within the pH region from about 5.7 to 10.3 that implies that the accessibility of the $ATPS_{des}$ tryptophan side chains to water molecules remains essentially invariant in this pH-range. At the same time, fluorescence quantum yield (area under fluorescence spectrum) remains practically constant within the pH region from about 6 to 10 indicating that no changes in fluorescence quenching properties of tryptophan residues environment occur in this pH-range. Thus, the pH region from 6 to 10, characterized by the absence of evident pH-dependent fluorescence changes, seems to be the right choice for $ATPS_{des}$ physico-chemical characterization.

Increasing the pH value to more than 10.1 results in a pronounced (ca. 80 %) decrease in fluorescence quantum yield and a considerable (ca. 9 nm) red shift of the fluorescence spectrum reflecting a denaturation unfolding of the enzyme followed by a blue shift after pH 12.2. It is probably related to an aggregation that would preserve the complete hydration of tryptophan residues. The decrease in pH from 6 to 4 results in a ca. 2.5 nm blue shift of tryptophan fluorescence spectrum, reflecting a decrease in mobility/polarity of environment of some tryptophan side chains, and pronounced (ca. 40 %) changes in fluorescence quantum yield with apparent pK_a value about 5, which seems to be due to protonation of Asp or Glu carboxylic groups. Acidification of the enzyme solution down to a pH of less than 4 caused a 3.5 nm red shift in the fluorescence spectrum, followed by a blue shift after pH 2, brought about by protein aggregation and considerable (ca. 12 %) decreasing of fluorescence quantum yield that seems to reflect an acidic denaturation of $ATPS_{des}$.

In the same time apparent pH for activity of $ATPS_{des}$ is essentially constant between pH range of 7.0 to 9.0 with optimum determined to be around 8 (data not shown). The broad pH range and slightly alkaline optimum are common characteristics of ATP sulfurylases examined previously.

Thermal denaturation of ATPS

DSC technique was used to determine the parameters of structural stability of $ATPS_{des}$. To apply thermodynamic theory to the protein unfolding process, reversibility had to be tested by rescanning the samples after cooling. The lack of any detectable thermogram upon rescanning in the pH range from 6 to 10 indicates that the protein was thermally unfolding irreversibly. The pH of 9.5 was chosen to be the best for structural stability analysis of $ATPS_{des}$ as the pH value with minimal level of aggregation. All further mentioned data are considered to this pH value. The

thermal denaturation of $ATPS_{des}$ gave rise to well defined DSC transitions whose apparent T_m values were dependent on the temperature scan rate. This effect can be seen in **Fig. 4**, which shows the thermal transitions for $ATPS_{des}$ at three different scan rates. All this clearly indicates that observed thermal transitions characterize a kinetically controlled process. Since, $ATPS_{des}$ forms dimer thermally induced denaturation should be accompanied by its dissociation into subunits, which should produce a concentration dependence on T_m value [171, 172]. In fact, the T_m and ΔH_{cal} values for the thermal denaturation of $ATPS_{des}$ were found to be independent within the protein concentration of 0.4 – 2.1 mg mL^{-1} range (data not shown) suggesting that the dimer does not dissociate when unfolds. For this reason the analysis of DSC transitions was accomplished using the simple two-state irreversible model $N_2 \xrightarrow{k} D_2$, in which only the native (N_2) and final, irreversible denatured (D_2) dimers are significantly populated and the conversion from N_2 to D_2 is determined by a strongly temperature-dependent, first order rate constant (k) that changes with temperature, as given by the Arrhenius equation. In this case, the excess heat capacity C_p^{ex} is given by the following equation [173]:

(A)

where v = dT/dt (K/min) is a scan rate value; ΔH is the enthalpy difference between the denatured and native states; E_A is the activation energy of the denaturation process; R is a gas constant, and T^* is temperature, where k is equal to 1 min^{-1}.

The excess heat capacity functions obtained for $ATPS_{des}$ in this case were analyzed by fitting the data to the two-state irreversible model either individually or globally, using scan rate as an additional variable. The highest likelihood values for E_A and T^* obtained with the nonlinear least squares minimization procedure are shown in **Fig. 4** (solid lines) and in **Table 1**. As can be seen, when fitting was carried out both separately on the individual experimental curves and simultaneously on all the curves, a good approximation was achieved. Attempts to include different irreversible models for ATPS denaturation - the Lumry-Eyring model, with a fast equilibrating first step, and the model that includes two consecutive irreversible steps [120, 121] - did not improve the goodness of the fit, indicating that the two-state irreversible model is sufficient to quantitatively describe the kinetics of $ATPS_{des}$ denaturation. This conclusion was further confirmed by our spectral investigation on the thermal denaturation of this enzyme.

Table 1. Arrhenius equation parameters estimates for the two-state irreversible model of the thermal denaturation of ATPS at pH 9.5

Parameter	Temperature scan rate (K/min)			
	0.49	1.00	1.45	Global fitting
ΔH, kcal/mol	119.0	127.2	141.3	
T^*, ^{o}C	48.6	48.4	48.4	48.4
E_A, kcal/mol	102.2	104.5	105.8	105.2
r	0.9990	0.9991	0.9992	0.9989

The correlation coefficient r was calculated as  , where y_i and y_i^{calc} are respectively the experimental and calculated values of C_p^{ex}; y_i^m is the mean of the experimental values of C_p^{ex} and n is the number of points

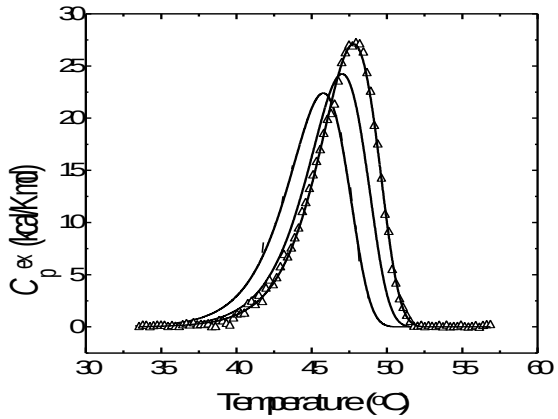

Fig. 4. Temperature dependence of the excess molar heat capacity of ATPS at scan rates of 29.4 K/h (squares), 59.9 K/h (circles) and 87 K/h (triangles) in 100 mM $NaHCO_3$/NaOH buffer, pH 9.5. Solid lines represent the best fit to each experimental curve using eq. (B). The protein concentration was 21 M.

Environmental changes in tryptophan side chains resulting from conformational changes in the tertiary structure of $ATPS_{des}$ were measured by intrinsic fluorescence spectroscopy. **Fig. 5A** shows the fluorescence spectra of intact (solid line) and thermally denatured (dashed line) $ATPS_{des}$ excited at 296 nm. Upon excitation at 296 nm, intact $ATPS_{des}$ showed a broad emission band with maximum at 343.2 nm. In the thermally denatured state at 60 °C, a loss of ~ 30 % of

the intensity was observed, along with a red shift in the maximum of tryptophan fluorescence spectrum position to 346.3 nm. In view of these results, we used the changes in the intensity and position of fluorescence spectra to analyze the effect of heating on the $ATPS_{des}$ denaturation. On increasing temperature (**Fig. 5B**, symbols), irreversible cooperative transition to the denatured state occurred, which was analyzed with nonlinear least squares fitting to the equation:

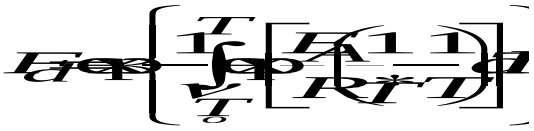

(B)

which is valid for two-state irreversible model and where F_d refers to the denatured fraction [173]. This fitting (solid line in **Fig. 5)** afforded the T^* parameter and the activation energy for $ATPS_{des}$. These results were 48.4 ± 0.2 °C and 103.4 ± 2.1 kcal/mol, respectively, which are in satisfactory agreement with the values obtained from DSC experiments (**Table 2**).

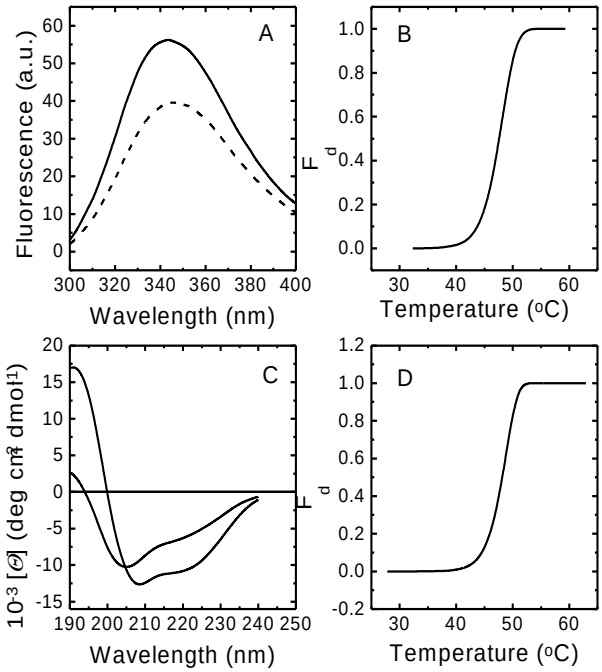

Fig. 5. Thermally induced denaturation of $ATPS_{des}$ studied by optical spectroscopy. (A) Fluorescence spectra of intact at 25 °C (solid line) and thermally denatured at 60 °C (dashed line) $ATPS_{des}$ at pH 9.5 and protein concentration of 15 μM. The excitation wavelength was 296 nm. (B) Fractional degree of thermal denaturation of $ATPS_{des}$ as function of temperature monitored by the changes in fluorescence quantum yield (open circles) and fluorescence spectrum maximum position (closed circles) obtained upon heating at constant scan rate of 78 K/h. The solid line represents the theoretical curve resulting from fitting the experimental data to the two-state irreversible model using **eq. B**. (C) Far-UV CD spectra of intact $ATPS_{des}$ at 25 °C (open circles) and thermally denatured $ATPS_{des}$ at 60 °C (closed circles) at pH 9.5 and protein concentration of 9.7 μM. The solid lines through the symbols are the best fits to the experimental data with CONTINLL program, using SP43 for the intact and SDP48 for denatured protein as reference sets. (D) Fractional degree of thermal denaturation of $ATPS_{des}$ as a function of temperature, at pH 9.5, monitored by the changes in ellipticity at 220 nm, obtained upon heating at a constant scan rate of 62 K/h. The solid line represents the best fit obtaining using **eq. B**.

The CD spectra of intact and thermally denatured $ATPS_{des}$ at pH = 9.5 are shown in **Fig. 5C**. Secondary structure analysis of CD spectra was performed using the CDPro software package [106]. The experimental data in 190-240 nm range were treated by three programs included in this software package SELCON3, CDSSTR, and CONTINLL, using SP43 and SDP48 (in case of denatured protein) reference sets. The markedly less rmsd between experimental data and theoretical curves produced by the programs with this reference set was for CONTINLL so results obtained with SELCON3 and CDSSTR were omitted. The fractions of secondary structure elements are given in **Table 2**. Upon heating the $ATPS_{des}$ up to the denaturation temperature, the shape of the spectrum changed, pointing to an increase in the unordered structure, mainly at the expense of the α-helical structure (see **Table 2**).

Table 2. Secondary structure elements (%) determined from analysis of CD spectra for ATPS at pH 9.5

	Secondary structure fractions (%)								α-helical segments		β- strand segments	
	α- helices			β-turns					N_α	Lα	N_β	L_β
protein	regular	distorted	total	regular	distorted	total	β-turns	unordered				
Intact	18	15	33	9	8	17	22	28	15.4	8.9	16.1	4.4
Denatured	8	9	17	12	8	20	17	46	9.4	7.5	15.8	5.1

The numbers (N) and average lengths (L) of α-helix (α) and β-strand (β) are given

The thermal denaturation of $ATPS_{des}$ was monitored by following the changes in molar ellipticity at 220 nm since at this wavelength the changes in ellipticity are significant upon enzyme denaturation. On increasing temperature (**Fig. 5**), irreversible cooperative transition to the denatured state occurred, which was analyzed using non-linear least squares fitting to **Eq. B** (see line through the data points). This fitting affords the T^* parameter and the activation energy of 48.7 ± 0.4 ^oC and 105.1 ± 1.9 kcal/mol, respectively, which are similar to the values for the same parameters obtained by the other methods used in this work. Thus all these independent experimental approaches support the conclusion that $ATPS_{des}$ thermal denaturation can be interpreted in terms of the irreversible two-state kinetic model, and that only two states of native and denatured dimmers are populated during denaturation process.

Different principles of structural organization used can be the base for increasing thermostability of proteins. For example ATP sulfurylase from *Aquifex aeolicus* have a higher packing efficiency. N and C terminals are shorter. Additionally, the N terminus packs against the protein core and C terminus does not extend past the protein core and C-terminal residue Asp546,

ion pairs with Arg399 to help fasten down the C terminus. Moreover, the volume of buried cavities in *Aquifex aeolicus* is one third less than in mesophilic *Pn. chrysogenum* [69].

In the same time hexameric, composed of nearly equal-size subunits and nearly identical amino acid compositions of ATP sulfurylases of thermophile *P. duponti* and mesophile *P. chrysogenum* have activation energies of 127 and 106 kcal respectively and the first enzyme is about 90 times more heat stable than the second one. At 50 $^{\circ}$C, the specific activity of *P. duponti* ATP sulfurylase is about twofold higher than that of the *Pn. chrysogenum* enzyme that dissociate into inactive subunits at 42 $^{\circ}$C. The more positive ΔS^* for inactivation of the *P. duponti* enzyme is consistent with a tighter or more highly ordered native state compared with that of the *Pn. chrysogenum* enzyme [165].

Acknowledgments:

This work was supported in part by Fundação para a Ciência e a Tecnologia (FCT) project PPCDT/POCI/QUI/59119/2004 (Portugal), Acçoes Integradas Luso Espanholas E-62/06 (Portugal-Spain), and FCT grants SFRH/BPD/28380/2006 (OYuG) and SFRH/BD/24744/ 2005 (AVK).

DISCUSSION

AK and ATP sulfurylase are essential enzymes for the growth and development of SRB and are indispensable for the bioenergetic metabolism of *Desulfovibrio*. ATP sulfurylase catalyses the first step of sulphate activation required for the reduction of sulphate to suphide that is used to drive oxidative phosphorylation and AK maintain a constant adenylate energy charge by interconverting stoichiometric amounts of ATP and AMP with two ADP molecules. Although these enzymes play important role in SRB, they have not been extensively studied.

Therefore, this work is devoted to the biochemical, physico-chemical, and structural characterization of AK and ATP sulfurylase from two Gram-negative strains of SRB *D. gigas* NCIB 9332 and *D. desulfuricans* ATCC 27774, respectively. The main focus was concentrated on the role of the metals found in ATPS and AK on structural organization and specifically stability properties of both enzymes.

The structural stability of ATP sulfurylase from *D. desulfuricans* and AK from *D. gigas* has been characterized by high-sensitivity differential scanning calorimetry, circular dichroism and steady-state tryptophan fluorescence methods. The mechanism of denaturation was studied by analysing the kinetic parameters in case of the ATP sulfurylase thermal denaturation process.

As it was reported earlier, the native AK from *D. gigas* and ATP sulfurylase from *D. desulfuricans*, are the Co^{2+}/Zn^{2+}- containing enzymes [24, 97]. Generally, the AK from Gram-positive bacteria contain a Cys-X_2-Cys-X_{16}-Cys-X_2-Cys/Asp structural motif in the LID domain that is responsible for the binding of zinc ion [13, 20, 22], whereas the AK from Gram-negative bacteria are usually devoid of metal ions, since their Cys residues are substituted by another four highly conserved amino acids - His, Ser, Asp and Thr, respectively [23]. Nevertheless, exceptions are the AK from *Desulfovibrio gigas* and *Desulfovibrio desulfuricans* ATCC 24774 with the metal- chelating motif ^{129}Cys-X_5-Hys-X_{15}-Cys-X_2-Cys, that binds either cobalt or zinc ion [24], the AK from *Paracoccus denitrificans*, overproduced in *E. coli* with the metal-chelating motif ^{126}Cys-X_2-Cys-X_{16}-Cys-X_2-Cys [15], that binds either zinc or iron, and the AK from *Chlamidia pneumoniae* and *Thermotoga neapolitana*, with the zinc-binding motifs ^{133}Cys-X_2-Cys-X_{12}-Cys-X_2-Cys and ^{134}Cys-X_2-Cys-X_{16}-Cys-X_2-Cys, respectively [25, 26]. Thus, to date three different metal ions - zinc, cobalt and iron have been found to be present in the AK from a few Gram-negative bacteria.

Biochemical and molecular biology methods and *in vivo* metal substitution techniques were applied to the fully cobalt-, zinc- and iron-substituted recombinant AK_{gig} overexpressed in *E. coli* cells.

Recombinant AK from *D. gigas* was overexpressed into *E coli* cells and homogeneous (with the ratio metal:protein 1:1) Co^{2+}-, Zn^{2+}- and Fe^{2+}- forms of the protein were received. The

conditions such as the type of the medium, the temperature, the time of incubation and the concentration of $MeCl_2$ (where Me= Co^{2+}, Zn^{2+} and Fe^{2+}) in the medium were optimized for production *in vivo* homogeneous Co^{2+}-, Zn^{2+}- and Fe^{2+}-AK_{gig} forms. The minimal medium M63B1 was chosen to be the best in a purpose to eliminate undesirable metal ion presence on it and get only one specific metal ion inside of LID domain in AK_{gig}. Specific conditions were developed to get desirable enzyme forms with sufficient yield and without excessive limitation of growth by presence of toxic concentrations of metals. For Co^{2+}-AK_{gig} production the time of incubation for 6 hours and the concentration of $CoCl_2$ of 160 µM were used, for Zn^{2+}-AK_{gig} - 4h and 250 µM $ZnCl_2$; for Fe^{2+}-AK_{gig}- 4h and 130 µM $FeCl_2$.

The pure AK_{gig} has a single polypeptide chain of 223 amino acids in length (accession number: CAZ66674) giving the MW value of 24.5 kDa. As were detected by MALDI-TOF and gel-filtration analysis, AK_{gig} forms monomer-dimer mixture with the MW values of 24.7 and 49.4 kDa, respectively, where monomer is the most populated form. Usually the molecular masses of AK range from 20 to 35 kDa per monomer [174] and most of them are monomers [35], but homodimeric [15] as well as homotrimeric [12, 14] forms of the enzyme are also known.

The UV-Visible absorbance spectrum of Co^{2+}-AK_{gig} originate from a d-d transitions due to Co^{2+} presence and ligand-to-metal charge transfer transitions (LMCT). Co^{2+}-AK_{gig} is blue in colour and exhibits five maxima at 275, 340, 610, 650 and 690 nm (ε_{340} = 3250 $M^{-1}cm^{-1}$, ε_{605} = 547 $M^{-1}cm^{-1}$ ε_{650} = 830 $M^{-1}cm^{-1}$, ε_{690} = 950 $M^{-1}cm^{-1}$), that are in good agreement with the UV-Vis spectrum of the native Co^{2+}/Zn^{2+}- form of AK_{gig} [24]. The absolute magnitude and molar absorption at around 340 nm records the number of thiolate groups coordinated to the metal and averages from 900 to 1300 $M^{-1}cm^{-1}$ per $S^{-}\rightarrow Co^{2+}$ bond [109, 175]. The energies of d-d transitions that are cantered at 610, 650 and 690 nm clearly validate ligation of cobalt ion predominantly via sulphur ligands [109].

Fe^{2+}-AK_{gig} exhibits three maxima at 275, 311 and 344 nm (ε_{311} = 5270 $M^{-1}cm^{-1}$, ε_{345} = 2390 $M^{-1}cm^{-1}$). The band at 311 nm and shoulder at 344 nm are due to the $S^{-}\rightarrow Fe^{2+}$ charge transfer, that are in good agreement with that of Fe^{2+}-form of AK_{den}, where iron (II) is ligated via four Cys amino acids [16].

The UV-Vis spectrum of Zn^{2+}-AK_{gig} exhibits one maximum at 275 nm, since $S^{-}\rightarrow Zn^{2+}$ charge transfer transitions are located at around 225 and 275 nm and should be hidden by aromatic amino acid absorbance that has a higher extinction coefficient [176].

The kinetic analysis of holo-AK_{gig} shows that the magnitude of K_m(AMP) and K_m(MgATP) of the forward reaction could be depicted in the following order: Fe^{2+}-AK_{gig}> Co^{2+}-AK_{gig}≈ Zn^{2+}-AK_{gig}, with very similar V_{max} values. The K_m(AMP) and K_m(MgATP) values are very similar

within each holo-form. The kinetic parameters of Co^{2+}- and Zn^{2+}-AK_{gig} for the forward reaction are very similar to those reported previously for AK_{col}. The K_m(ADP, MgADP) values for the backward reaction could be set in the following order Co^{2+}-AK_{gig}>Zn^{2+}-AK_{gig}>Fe^{2+}-AK_{gig}. Thus, the iron form of AK_{gig} has the highest K_m values (or the lowest affinity) to the substrates of the forward reaction (MgATP and AMP) and the lowest one (or the highest affinity) for the substrates of the backward reaction (MgADP and ADP), as compared to Co^{2+}- and Zn^{2+}- forms of AK_{gig}. These results show that the type of the metal ion inside LID domain of AK_{gig} influence the kinetic properties of the enzyme. This observation could be supported by previously published data, that LID and AMPbd domains of AK are related to catalysis while CORE is responsible for structural stability of enzyme [30]. At the same time this statement could not be in contradictory with that reported earlier for AK_{den}, where no changes were observed between Zn^{2+}- and Fe^{2+}- forms, since the metal binding center of the metal ion is different [16].

The disparities in the apparent optimal temperatures for enzymatic activity of Co^{2+}-, Fe^{2+}- and Zn^{2+}-AK_{gig} forms were found. All three temperature profiles have similar shapes, with maxima at 32 °C for Fe^{2+}-AK_{gig}, and 36 °C for Co^{2+}- and Zn^{2+}-AK_{gig}. This result clearly shows that the type of the metal ion in the LID mobile domain controls to some extent the temperature dependence of the enzyme's catalytic activity. This observations is in accord with previously published data of [13], where it was shown that the two mobile domains themselves (the AMPbind and LID domains), control the temperature dependence of the catalytic activity [30]. Here, we have shown that metal ion exchange in LID domain could cause considerable differences in temperature optimum of catalytic activity of the enzyme.

CD spectroscopy in far and near UV regions were performed for the purpose to investigate changes in secondary and teriary structures of holo-AK_{gig}. The far-UV CD spectra of metal-chelated forms of AK_{gig} are characterized by double minima at 208 and 222 nm, indicative of α-helical structure of the enzyme. A detailed secondary structure analysis of the far-UV CD spectra was performed using the CDPro software package. The results of this analysis show that the secondary structural elements of all metal-chelated forms of AK_{gig} are practically equal but slightly differ from the native Co^{2+}/Zn^{2+}-AK_{gig} [28]. In contrast to spectra obtained in the far-UV region, the near-UV CD spectra of all holo-forms of AK_{gig} are markedly different. In all holo-AK_{gig} studied, the contributions of phenylalanine and tryptophan residues are almost the same, while the contribution of tyrosine residues is different. Thus, for the Co^{2+}-form of AK_{gig} the negative minimum is observed at 278 nm; for the Zn^{2+}-form this peak is red-shifted to 282 nm with comparable amplitude, and finally for the Fe^{2+}-form this band displays a strong red shift to the 286 nm with two-fold amplitude. The Fe^{2+}-AK_{gig} has peaks that can be attributed to the presence of iron (314, 328 and 349 nm), while the Co^{2+}-AK_{gig} has peaks at 336, 356, 390 and

694 nm that are due to the cobalt presence. These data clearly indicate that nevertheless of the equal secondary structure content between all holo-AK_{gig}, the tertiary structure of Fe^{2+}- AK_{gig} is significantly differ from that of Co^{2+} and Zn^{2+}-AK_{gig}.

The factors contributing to the thermostability of a protein are known to be very subtle. In general, they include the hydrophobic packing density, the ratio of the surface area to volume, hydrogen bonding and salt bridging. Metal chelating may also be involved in increasing protein stability [23, 28]. DSC technique reveals the thermodynamic properties of the holo-AK_{gig}, the roles of cobalt, zinc and iron ions in enzyme's thermostability and how the nature of metal ion inside of LID domain influence the thermal transition process of the whole enzyme. Thus, reversible thermal denaturation process was detected for both cobalt and zinc forms, which can be described by a simple two-state equilibrium model with T_m values of 43.7 °C and 45.3 °C were observed for Co^{2+}- and Zn^{2+}- AK_{gig} forms, respectively. The irreversible thermal denaturation process was observed for Fe^{2+}-AK_{gig} with T_m value of approximately 45 °C. The T_s value of Fe^{2+}- form is only -12.9 °C, while for Zn^{2+}- and Co^{2+}-AK_{gig} it is -15.4 °C and -17.9 °C, respectively. The marked difference between this value for Fe^{2+}- AK_{gig}, compared to Co^{2+}- AK_{gig} and Zn^{2+}-AK_{gig} could be the reason of the tertiary structure differences observed for this form.

Co^{2+}-, Zn^{2+}- and Fe^{2+}-AK_{gig} and Co^{2+}/Zn^{2+}-$ATPS_{des}$ were crystallized and their corresponding three-dimensional structures were solved, that provide insight into understanding structure-function relationships additionally to the physico-chemical characterization.

Crystal structures of substrate-free forms of the Co^{2+}-, Zn^{2+}- and Fe^{2+}-AK_{gig} have been determined by X-ray crystallography with the resolution of 2.0, 2.1 and 3.0 Å, respectively. The best crystallization conditions were 0.2 M tartrate Na/K, 0.1 M MES (pH 6.5) and 20 % PEG 2K or 8K (the protein: well solution ratio in the drop was 1:1, 1:2 or 1:3 with the final drop volume of 4, 6 or 8 µl) using a protein stock concentration of ~10 $mg \cdot mL^{-1}$ at 277 K. Crystals grew to about 0.30 × 0.07 × 0.07 mm during 7 days at 4 °C. The presence of corresponding metals in the crystallized forms of AK was confirmed using the anomalous signals by X-ray fluorescence scan. Co^{2+}-AK_{gig} was crystallized as non-crystallographic dimer (*C2* space group) in a *back to back* manner, while Zn^{2+}- and Fe^{2+}-AK_{gig} were crystallized as monomers in *I222* space group. The *back to ba*ck dimer in the crystallographic asymmetric unit is stabilized by 6 hydrogen bonds and 6 salt bridge interactions. Residues 50-55 and residues 172-185 are mainly involved in this dimer formation. Co^{2+}-AK_{gig} also forms the crystallographic dimer with its rotational symmetry mate (-x, y, -z) in a *face to face* manner. The LID domain of the enzyme and the residues 10-15 are mainly contribute to these interactions. This dimer is held by 15 strong hydrogen bonding interactions. The non-accessible surface area in the interface of the *face to face* dimer is (~1010 $Å^2$) almost double compare to the *back to back* dimer (~ 606 $Å^2$). The Fe^{2+}-

and Zn^{2+}-AK_{gig} also form the *face to face* and *back to back* dimers. This is the first reported example of AK' s dimer formation performed by two manners.

The carbon skeleton (C_x) superposition of Zn^{2+}-AK_{gig} with Co^{2+}- and Fe^{2+}-AK_{gig} give the root mean square deviation (rmsd) values of around 0.1 and 0.37 Å respectively, indicating that all three holo-forms of AK_{gig} have very similar crystal structures. Moreover, the normal mode analysis (NMA) was performed to check the dynamics of these domains and to find out whether metal ion has any effect on the dynamic motions of the LID domain. Thus, irrespective of the metal ion nature, all three forms of the enzyme show the same directionality. The largest distance fluctuations for the residues have found in the LID domain and AMP binding region (AMP_{bd}). In spite of the fact that no changes were detected either in crystal structure or in dynamics of two catalytically important domains (LID and AMP_{bd}), various biochemical methods including kinetic, DSC and CD analysis display differences mainly between Fe^{2+}- and Co^{2+}/Zn^{2+}- forms of AK_{gig}. It is possible that all above mentioned differences, related to the holo-AK_{gig}, arise in solution phase and come to naught during crystallization process.

Around 50 crystal structures of AK have been reported till now. Nevertheless of the only 28 % sequence identity and metal lacks in human AK6, C_x- carbon skeleton superposition of it with AK_{gig} gives the highest similarity with the rmsd value of 2 Å.

The pure native Co^{2+}/Zn^{2+}- $ATPS_{des}$ has a single polypeptide chain of 423 amino acids (accession number CAQ30513) in which the APS kinase-like C-terminal domain of *Sacchromyces cerevisiae* and *Peniillium chrysogenum* ATP sulfurylases is lacking, as in *Riftia pahyptila* symbiont and *Thermus thermophilus*. The identities with others $ATPS_{des}$ is very high and attend to 92 % identity. In the same time, the identities of the $ATPS_{des}$ with the ATP sulfurylases from *Sacchromyces cerevisiae*, *Peniillium chrysogenum*, the *Riftia pahyptila* symbiont, *Thermus thermophilus,* and *Aquifex aeolicus* for which crystallographic structures are known, are only 34 %, 33 %, 39 %, 39 %, and 35 %, respectively. In spite of this, all contain highly conserved motifs that are involved in substrate binding and catalysis: the HXXH (binds the PP_i group of ATP and $MgPP_i$), QXRNP (binds the phosphosulphate group of APS and the β-phosphate of ATP) and GRD (binds sulphate and ribose groups of APS and SO_4^{2-}) motifs, and also the mobile loop (hp)3HXhpXGXXKXXDhpXXXXR (hp-hydrophobic residues), which does not interact directly with substrate but instead orients residues that do bind the substrate in the ATP sulfurylase. In the same time till now only one structure of the metal containing ATP sulfurylases was published [87].

It has been shown that at pH 9.5, the thermal denaturation process of $ATPS_{des}$ is irreversible and consists of a highly cooperative transition between the folded and unfolded dimers with the value of the free stabilization energy of around 105 kcal per mol at 25 °C. The process is

strongly dependent upon the scan rate, suggesting that it is under kinetic control. According to the $ATPS_{des}$ dimer formation in solution phase, the dissociation into subunits should give concentration dependence on thermal denaturation values. The T_m and ΔH_{cal} values of the $ATPS_{des}$ thermal denaturation process were found to be independent within the protein concentration range of 0.4 – 2.1 mg mL^{-1}, suggesting that the dimer does not dissociate into monomers when unfolds. Analysis of the kinetic parameters of $ATPS_{des}$ denaturation was accomplished on the basis of the simple kinetic scheme: $N_2 \xrightarrow{k} D_2$, where k is a first-order kinetic constant that changes with temperature, as given by the Arrhenius equation; N is the native state, and D is the denatured state, and thermodynamic information was obtained by extrapolation of the kinetic transition parameters to an infinite heating rate.

The crystal structure of substrate-free form of $ATPS_{des}$ has been determined by X-ray crystallography to the resolution 2.5 Å. $ATPS_{des}$ was crystallized as dimer in a C2221 space group. The only zinc ion was detected by X-ray anomalous fluorescence scan in $ATPS_{des}$ structure. The best crystallization conditions were 3 M ammonium sulfate, 100 mM Tris/HCl pH 7.5 with 10 % (v/v) MPD as an additive (the protein:well solution:MPD ratio was 1:1:0.2 and the final drop volume was 2.4 ml) using a protein concentration of 10 mg mL^{-1} at 277 K. Crystals grew to dimensions of about 0.2 × 0.1 × 0.05 mm.

CONCLUSIONS

1. The optimal conditions were established for overexpression *in vivo* of recombinant Co^{2+}, Zn^{2+} and Fe^{2+}- forms of AK_{gig} in *E. coli* cells.
2. The type of metal ion inside of LID domain of AK_{gig} does not influence to chromatographic properties during purification of the enzyme.
3. The apparent temperature optima for the activity of holo-AK_{gig} forms were determed. The Co^{2+}-, Zn^{2+}-AK_{gig} provide the same temperature optima at 36 °C, while for Fe^{2+}-AK_{gig} it is lower and equal to 32 °C.
4. The thermal denaturation mechanisms were established for holo-forms of AK_{gig}. Thus, for Co^{2+}- and Zn^{2+}-AK_{gig} reversible denaturation process was detected with T_m values of 43.7 °C and 45.3 °C, respectively, while the irreversible thermal denaturation was observed for Fe^{2+}-AK_{gig} with T_m value of approximately 45 °C.
5. The secondary structure elements content was determed for all tested holo-AK_{gig}, while tertiary structures produce recognisable differences.
6. Holo- AK_{gig} shows the highest affinity of Fe^{2+}-AK_{gig} to the substrates of the backward reaction (Mg^{2+}ADP/ADP), while Co^{2+}- and Zn^{2+}-AK_{gig} have the highest affinity to the substrates of the forward reaction AMP and MgATP, respectively. Thus, the magnitude of the K_m(AMP) and K_m(MgATP) could be depicted in the following order: Fe^{2+}-AK_{gig} > Co^{2+}-AK_{gig} ≈ Zn^{2+}-AK_{gig}, while for K_m(ADP,MgADP) this order is Co^{2+}-AK_{gig} > Zn^{2+}-AK_{gig} > Fe^{2+}-AK_{gig}.
7. Well ordered diffracted crystals of Co^{2+}-, Zn^{2+}- and Fe^{2+}-AK_{gig} were obtained, and the structures were resolved with a resolution of 2.0 Å, 2.1 Å and 3 Å, respectively.
8. Holo- AK_{gig} could form crystallographic dimers in both *face to face* and *back to back* manner. This dimer formation in both manners is the first one reported for adenylate kinases. The *face to face* is held by 15 strong hydrogen interactions, while *back to back* do only by 6 hydrogen bonds and 6 salt bridge interactions. The non- accessible surface area in the interface of the *face to face* dimer is ~1010 $Å^2$ and almost double if compare to the *back to back* dimer (~606 $Å^2$).
9. The structural differences between holo-AK_{gig} were revealed. The carbon skeleton superposition of Zn^{2+}- AK_{gig} with Co^{2+}- and Fe^{2+}-AK_{gig} gives the rmsd values of around 0.1 Å and 0.37 Å, respectively, indicating very similar crystal structures for all of them.
10. The NMA analysis indicates that metal ion nature does not influence the directionality of the substrate-binding domains (LID and AMP_{bd}).

11. ATPS thermal denaturation can be interpreted in terms of the irreversible two-state kinetic model: $N_2 \xrightarrow{k} D_2$, with the value of the free stabilization energy of around 105 kcal per mol at 25 °C, where only two states, native and denatured dimers are populated in its denaturation process. Therefore, ATP sulfurylase denaturation occurs without dissociation into the subunits in the transition region.
12. Well ordered diffracted crystals of native ATPS from *D. desulfuricans* were obtained and the structure was resolved with a resolution of 2.5 Å.

References

1. Cottrell, M.T., Cary, S.C., *Diversity of dissimilatory bisulfite reductase genes of bacteria associated with the deep-sea hydrothermal vent polychaete annelid Alvinella pompejana.* Appl. Environ. Microbiol. , 1999. **65**(3): p. 1127-32.
2. Ouattara, A.S., Patel, B.K., Cayol, J.L., Cuzin, N., Traore, A.S., Garcia, J.L., *Isolation and characterization of Desulfovibrio burkinensis sp. nov. from an African ricefield, and phylogeny of Desulfovibrio alcoholivorans.* Int J Syst Bacteriol., 1999. **49** (2): p. 639-43.
3. Rosencrantz, D., Rainey, F.A., Janssen, P.H., *Culturable populations of Sporomusa spp. and Desulfovibrio spp. in the anoxic bulk soil of flooded rice microcosms.* Appl Environ Microbiol., 1999. **65**(8): p. 3526-33.
4. Barton, L.L., Hamilton, W.A. , *Sulphate-reducing bacteria. Environmental and engineered systems* ed. C.U. Press. 2007.
5. Liu, C.L., Peck, H.D., *Comparative bionergetics of sulfate reduction in Desulfovibrio and Desulfotomaculum spp.* J. Bacteriol., 1981. **145**: p. 966-973.
6. Yu, L., Ishida, T., Ozawa, K., Akutsu, H., and Horiike, K., *Purification and characterization of homo- and hetero-dimeric acetate kinases from the sulfate-reducing bacterium Desulfovibrio vulgaris.* J. Biochem., 2001. **129**: p. 411-421.
7. Noda, L.H., *Adenylate kinase*. The Enzymes, ed. P.D. Boyer. Vol. VIII. 1973, New York: 3rd edn. Academic Press. 279-305.
8. Small, G.D., Cooper, C., *Studies on the occurrence and biosynthesis of adenosine tetraphosphate.* Biochemistry, 1966. **5**(1): p. 26-33.
9. Kupriyanov, V.V., Ferretti, J.A., Balaban, R.S., *Muscle adenylate kinase catalyzes adenosine 5'-tetraphosphate synthesis from ATP and ADP.* Biochim Biophys Acta. , 1986. **869**(1): p. 107-11.
10. Fry, D.C., Kuby, S.A., Mildvan, A.S., *NMR studies of the AMP-binding site and mechanism of adenylate kinase.* Biochemistry, 1987. **26**(6): p. 1645-55.
11. Brune, M., Schumann, R., Wittinghofer, F., *Cloning and sequencing of the adenylate kinase gene (adk) of Escherichia coli.* Nucleic Acids Res. , 1985. **13**(19): p. 7139-51.
12. Davlieva, M., Shamoo, Y., *Crystal structure of a trimeric archaeal adenylate kinase from the mesophile Methanococcus maripaludis with an unusually broad functional range and thermal stability.* Proteins, 2009. **0**: p. 00-00.
13. Bae, E., Phillips, G.N.Jr. , *Structures and analysis of highly homologous psychrophilic, mesophilic, and thermophilic adenylate kinases.* J. Biol. Chem. , 2004. **279**: p. 28202-28208.
14. Criswell, A.R., Bae, E., Stec, B., Konisky J. & Philips Jr.G.N., *Structures of the thermophilic and mesophilic adenylate kinases from the genus methanococcus.* J. Mol. Biol., 2003. **330**: p. 1087-1099.
15. Deligiannakis, Y., Boussac, A., Bottin, H., Perrier, V., Barzu, O., Gilles, A.-M. , *A new non-heme iron environment in Paracoccus denitrificans adenylate kinase studied by electron paramagnetic resonance and electron spin echo envelope modulation spectroscopy.* Biochemistry, 1997. **36**: p. 9446-9452.
16. Perrier, V., Burlacu-Miron, S., Boussac, A., Meier, A., Gilles, A.-M., *Metal chelating properties of adenylate kinase from Paracoccus denitrificans.* Protein Eng. , 1998. **11**(10): p. 917-23.
17. Müller, C.W., Schulz, G.E., *Structure of the complex between adenylate kinase from Escherichia coli and the inhibitor Ap5A refined at 1.9 A resolution. A model for a catalytic transition state.* J Mol Biol., 1992. **224**(1): p. 159-77.
18. Müller, C.W., Schlauderer, G.J., Reinstein, J., and Schulz, G.E., *Adenylate kinase motions during catalysis: an energetic counterweight balancing substrate binding.* Structure, 1996. **4**: p. 147-156.
19. Schlauderer, G.J., Schulz, G.E., *The structure of bovine mitochondrial adenylate kinase: comparison with isoenzymes in other compartments.* Protein Sci., 1996. **5**: p. 434-441.

20. Berry, M.B., Phillips, G.N.Jr., *Crystal structures of Bacillus stearothermophilus adenylate kinase with bound Ap5A, Mg^{2+} Ap5A, and Mn^{2+} Ap5A reveal an intermediate lid position and six coordinate octahedral geometry for bound Mg^{2+} and Mn^{2+}*. Proteins, 1998. **32**(3): p. 276-288.
21. Goelz, S.E., Cronan, J.E.Jr., *Adenylate kinase of Escherichia coli: evidence for a functional interaction in phospholipid synthesis.* Biochemistry, 1982. **21**(1): p. 189-95.
22. Gilles, A.M., Glaser, P., Perrier, V., Meier, A., Longin, R., Sebald, M., Maignan, L., Pistotnik, E., and Bârzu, O., *Zinc, a structural component of adenylate kinases from Gram-positive bacteria.* J Bacteriol., 1994. **176**(2): p. 520-523.
23. Perrier, V., Burlacu-Miron, S., Bourgeois, S., Surewicz, W.K., Gilles, A.-M., *Genetically Engineered Zinc-chelating Adenylate Kinase from Escherichia coli with Enhanced Thermal Stability.* J Biol Chem, , 1998. **273**(30): p. 19097-19101.
24. Gavel, O.Y., Bursakov, S.A., Rocco, G. Di, Trincão, J. , Pickering, I.J., Graham, G.N., Calvete, J.J., Shnyrov, V.L., Brondino, C.D., Pereira, A.S:, Lampreia, J., Tavares, P., Moura, J.J.G., Moura, I. , *A new type of metal-binding site in cobalt- and zinc-containing adenylate kinases isolated from sulfate-reducers Desulfovibrio gigas and Desulfovibrio desulfuricans ATCC 27774*. J Inorg Biochem, 2008. **102**(5-6): p. 1380-1395.
25. Miura, K., Inouye, S., Skai, K., Takaoka, H., Kishi, F., Tabuchi, M., Tanaka, T., Matsumoto, H., Shirai, M., Nakazawa, T., Nakazawa, A., *Cloning and characterization of adenylate kinase from Chlamydia pneumoniae.* J. Biol. Chem. , 2001. **276**: p. 13490-13498.
26. Vieille, C., Krishnamurthy, H., Hyun, H.-H., Savchenko, A., Yan, H., Zeikus, G., *Thermotoga neapolitana adenylate kinase is highly active at 30 degrees C.* Biochem. J. , 2003. **372**: p. 577-585.
27. Gavel, O.Y., *Novel metalloproteins from sulphate-reducing bacteria. Proteins containing cobalt, zinc and a heterometallic copper-molybdenum-sulphur cluster.*, in *Chemistry*. 2006, Universidade Nova de Lisboa: Caparica. p. 219.
28. Gavel, O.Y., Bursakov, S.A., Pina, D.G., Zhadan, G.G., Moura, J.J.G., Moura, I. and Shnyrov, V. L., *Structural stability of adenylate kinase from the sulfate-reducing bacteria Desulfovibrio gigas.* Biophysical Chemistry, 2004. **110**(1-2): p. 83-92.
29. Glaser, P., Presecan, E., Delepierre, M., Surewicz, W.K., Mantsch, H.H., Bârzu, O., Gilles, A.-M., *Zinc, a novel structural element found in the family of bacterial adenylate kinases.* Biochemistry, 1992. **31**(12): p. 3038-43.
30. Bae, E., Phillips, G.N.Jr., *Roles of static and dynamic domains in stability and catalysis of adenylate kinase.* Proc. Natl. Acad. Sci. U.S.A., 2006. **103**(7): p. 2132-7.
31. Rhoads, D.G., Lowenstein, J.M., *Initial velocity and equilibrium kinetics of myokinase.* J Biol Chem., 1968. **243**(14): p. 3963-72.
32. Hamada, M., Kuby, S.A., *Studies on adenosine triphosphate transphosphorylases. XIII. Kinetic properties of the crystalline rabbit muscle ATP-AMP transphorphorylase (adenylate kinase) and a comparison with the crystalline calf muscle and liver adenylate kinases.* Arch Biochem Biophys., 1978a. **190**(2): p. 772-9.
33. Hamada, M., Palmieri, R.H., Russel, G.A. Kuby, S.A., *Studies of adenosine triphosphate transphosphorylases. XIV. Equilibrium binding properties of the crystalline rabbit and calf muscle ATP--AMP transphosphorylase (adenylate kinase) and derived peptide fragments.* Arch. Biochem, Biophis., 1978b. **195**: p. 155-177.
34. Yan, H.G., Tsai, M.D., *Mechanism of adenylate kinase. Demonstration of a functional relationship between aspartate 93 and Mg^{2+} by site-directed mutagenesis and proton, phosphorus-31, and magnesium-25 NMR.* Biochemistry, 1991. **30**(22): p. 5539-46.
35. Yan, H., Tsai, M.D., *Nucleoside monophosphate kinases: structure, mechanism, and substrate specificity.* Adv Enzymol Relat Areas Mol Biol., 1999. **73**: p. 103-34.
36. Sheng, X.R., Li, X., Pan, X.M., *An iso-random Bi Bi mechanism for adenylate kinase.* J Biol Chem., 1999. **274**(32): p. 22238-42.

37. Vonrhein, C., Schlauderer, G. and Schulz, G.E., *Movie of the structural changes during a catalytic cycle of nucleoside monophosphate kinases.* Structure, 1995. **3**: p. 483–490.
38. Font, B., Gautheron, D.C., *General and kinetic properties of pig heart mitochondrial adenylate kinase.* Biochim Biophys Acta., 1980. **611**(2): p. 299-308.
39. Van Rompay, A.R., Johansson, M., Karlsson, A., *Phosphorylation of nucleosides and nucleoside analogs by mammalian nucleoside monophosphate kinases.* Pharmacol Ther., 2000. **87**(2-3): p. 189-98.
40. Ginger, M.L., Ngazoa, E.S., Pereira, C.A., Pullen, T.J., Kabiri, M., Becker, K., Gull, K., Steverding, D., *Intracellular positioning of isoforms explains an unusually large adenylate kinase gene family in the parasite Trypanosoma brucei.* J Biol Chem., 2005. **280**(12): p. 11781-9.
41. Ren, H., Wang, L., Bennett, M., Liang, Y., Zheng, X., Lu, F., Li, L., Nan, J., Luo, M., Eriksson, S., Zhang, C., Su, X.D., *The crystal structure of human adenylate kinase 6: An adenylate kinase localized to the cell nucleus.* Proc Natl Acad Sci U S A., 2005. **102**(2): p. 303-8.
42. Munier-Lehmann, H., Chenal-Francisque, V., Ionescu, M., Chrisova, P., Foulon, J., Carniel, E., Bârzu, O., *Relationship between bacterial virulence and nucleotide metabolism: a mutation in the adenylate kinase gene renders Yersinia pestis avirulent.* Biochem J., 2003. **373**: p. 515-22.
43. Purich, D.L., Fromm, H.J., *Studies on factors influencing enzyme responses to adenylate energy charge.* J Biol Chem., 1972. **247**(1): p. 249-55.
44. Kleczkowski, L.A., Randall, D.D. and Zahler, W.L., *Adenylate kinase from maize leaves – true substrates, inhibition by P1, P5-di(adenosine-5´)pentaphosphate and kinetic mechanism.* Z. Naturforsch., 1990. **45c**: p. 607-613.
45. Sillén, L.G., and Martell, A.E., *Stability constants of metal-ion complexes*, ed. I.S. Publication. Vol. 17. 1964: The Chemical Society, London.
46. Krishnamurthy, H., Lou, H., Kimple, A., Vieille, C., Cukier, R.I., *Associative mechanism for phosphoryl transfer: a molecular dynamics simulation of Escherichia coli adenylate kinase complexed with its substrates.* Proteins, 2005. **58**(1): p. 88-100.
47. Berry, M.B., Bae, E., Bilderback, T.R., Glaser, M., Phillips, G.N.Jr., *Crystal structure of ADP/AMP complex of Escherichia coli adenylate kinase.* Proteins, 2006. **62**(2): p. 555-6.
48. Cleland, W.W., Hengge, A.C., *Mechanisms of phosphoryl and acyl transfer.* FASEB J., 1995. **9**(15): p. 1585-94.
49. Liu, R., Xu, H., Wei, Z., Wang, Y., Lin, Y., Gong, W., *Crystal structure of human adenylate kinase 4 (L171P) suggests the role of hinge region in protein domain motion.* Biochemical and Biophysical Research Communications, 2008. **379**(1): p. 92-97.
50. Hanna, E., Ng, K.F., MacRae, I.J., Bley, C.J., Fisher, A.J., Segel, I.H., *Kinetic and stability properties of Penicillium chrysogenum ATP sulfurylase missing the C-terminal regulatory domain.* J Biol Chem., 2004. **279**(6): p. 4415-24.
51. Leyh, T.S., *The physical biochemistry and molecular genetics of sulfate activation.* Crit Rev Biochem Mol Biol., 1993. **28**(6): p. 515-42.
52. Leyh, T.S., Suo, Y., *GTPase-mediated activation of ATP sulfurylase.* J Biol Chem., 1992. **267**(1): p. 542-5.
53. Liu, C., Martin, E., Leyh, T.S., *GTPase activation of ATP sulfurylase: the mechanism.* Biochemistry, 1994. **33**(8): p. 2042-7.
54. Savage, H., Montoya, G., Svensson, C., Schwenn, J.D., Sinning, I., *Crystal structure of phosphoadenylyl sulphate (PAPS) reductase: a new family of adenine nucleotide alpha hydrolases.* Structure, 1997. **5**(7): p. 895-906.
55. Inagaki, Y., Doolittle, W.F., Baldauf, S.L., Roger, A.J., *Lateral transfer of an EF-1alpha gene: origin and evolution of the large subunit of ATP sulfurylase in eubacteria.* Curr Biol., 2002. **12**(9): p. 772-6.

56. Bradley, M.E., Rest, J.S., Li, W.-H., Schwartz, N.B., *Sulfate Activation Enzymes: Phylogeny and Association with Pyrophosphatase.* J. Mol. Evol., 2009. **68**: p. 1-13.
57. Gay, S.C., Fribourgh, J.L., Donohoue, P.D., Segel, I.H. and Fisher, A.J., *Kinetic properties of ATP sulfurylase and APS kinase from Thiobacillus denitrificans.* Archives of Biochemistry and Biophysics, 2009. **489**(1-2): p. 110-117.
58. Geller, D.H., Henry, J.G., Belch, J., Schwartz, N.B., *Co-purification and characterization of ATP-sulfurylase and adenosine-5'-phosphosulfate kinase from rat chondrosarcoma.* J Biol Chem., 1987. **262**(15): p. 7374-82.
59. Lyle, S., Stanczak, J., Ng, K., Schwartz, N.B., *Rat chondrosarcoma ATP sulfurylase and adenosine 5'-phosphosulfate kinase reside on a single bifunctional protein.* Biochemistry, 1994a. **33**(19): p. 5920-5.
60. Rosenthal, E., Leustek, T., *A multifunctional Urechis caupo protein, PAPS synthetase, has both ATP sulfurylase and APS kinase activities.* Gene, 1995. **165**(2): p. 243-8.
61. Lyle, S., Ozeran, J.D., Stanczak, J., Westley, J., Schwartz, N.B., *Intermediate channeling between ATP sulfurylase and adenosine 5'-phosphosulfate kinase from rat chondrosarcoma.* Biochemistry, 1994b. **33**(22): p. 6822-7.
62. Lyle, S., Stanczak, J.D., Westley, J., Schwartz, N.B., *Sulfate-activating enzymes in normal and brachymorphic mice: evidence for a channeling defect.* Biochemistry, 1995. **34**(3): p. 940-5.
63. Fuda, H., Shimizu, C., Lee, Y.C., Akita, H., Strott, C.A., *Characterization and expression of human bifunctional 3'-phosphoadenosine 5'-phosphosulphate synthase isoforms.* Biochem J., 2002. **365**: p. 497-504.
64. Lansdon, E.B., Fisher, A.J., Segel, I.H., *Human 3'-phosphoadenosine 5'-phosphosulfate synthetase (isoform 1, brain): kinetic properties of the adenosine triphosphate sulfurylase and adenosine 5'-phosphosulfate kinase domains.* Biochemistry, 2004. **43**(14): p. 4356-65.
65. Harjes, S., Bayer, P., Scheidig, A.J., *The crystal structure of human PAPS synthetase 1 reveals asymmetry in substrate binding.* J Mol Biol., 2005. **347**(3): p. 623-35.
66. Sun, M., Leyh, T.S., *Channeling in sulfate activating complexes.* Biochemistry, 2006. **45**(38): p. 11304-11.
67. Foster, B.A., Thomas, S.M., Mahr, J.A., Renosto, F., Patel, H.C., Segel, I.H., *Cloning and sequencing of ATP sulfurylase from Penicillium chrysogenum. Identification of a likely allosteric domain.* J Biol Chem., 1994. **269**(31): p. 19777-86.
68. MacRae, I.J., Rose, A.B., Segel, I.H., *Adenosine 5'-phosphosulfate kinase from Penicillium chrysogenum. site-directed mutagenesis at putative phosphoryl-accepting and ATP P-loop residues.* J Biol Chem., 1998. **273**(44): p. 28583-9.
69. Hanna, E., MacRae, I.J., Medina, D.C., Fisher, A.J., Segel, I.H., *ATP sulfurylase from the hyperthermophilic chemolithotroph Aquifex aeolicus.* Arch Biochem Biophys., 2002. **406**(2): p. 275-88.
70. Ullrich, T.C., Blaesse, M., Huber, R., *Crystal structure of ATP sulfurylase from Saccharomyces cerevisiae, a key enzyme in sulfate activation.* EMBO J., 2001a. **20**(3): p. 316-29.
71. Lalor, D.J., Schnyder, T., Saridakis, V., Pilloff, D.E., Dong, A., Tang, H., Leyh, T.S., Pai, E.F., *Structural and functional analysis of a truncated form of Saccharomyces cerevisiae ATP sulfurylase: C-terminal domain essential for oligomer formation but not for activity.* Protein Eng., 2003. **16**(12): p. 1071-9.
72. Renosto, F., Martin, R.L., Wailes, L.M., Daley, L.A., Segel, I.H., *Regulation of inorganic sulfate activation in filamentous fungi. Allosteric inhibition of ATP sulfurylase by 3'-phosphoadenosine-5'-phosphosulfate.* J Biol Chem., 1990. **265**(18): p. 10300-8.
73. MacRae, I., Segel, I.H., *ATP sulfurylase from filamentous fungi: which sulfonucleotide is the true allosteric effector?* Arch Biochem Biophys., 1997. **337**(1): p. 17-26.

74. Pinto, R., Tang, Q.X., Britton, W.J., Leyh, T.S., Triccas, J.A., *The Mycobacterium tuberculosis cysD and cysNC genes form a stress-induced operon that encodes a tri-functional sulfate-activating complex.* Microbiology, 2004. **150**: p. 1681-6.
75. Sperling, D., Kappler, U., Wynen, A., Dahl, C., Trüper, H.G., *Dissimilatory ATP sulfurylase from the hyperthermophilic sulfate reducer Archaeoglobus fulgidus belongs to the group of homo-oligomeric ATP sulfurylases.* FEMS Microbiol Lett., 1998. **162**(2): p. 257-64.
76. Kappler, U., Dahl, C., *Enzymology and molecular biology of prokaryotic sulfite oxidation.* FEMS Microbiol Lett., 2001. **203**(1): p. 1-9.
77. Bork, P., Holm, L., Koonin, E.V., Sander, C., *The cytidylyltransferase superfamily: identification of the nucleotide-binding site and fold prediction.* Proteins, 1995. **22**(3): p. 259-66.
78. Deyrup, A.T., Singh, B., Krishnan, S., Lyle, S., Schwartz, N.B., *Chemical modification and site-directed mutagenesis of conserved HXXH and PP-loop motif arginines and histidines in the murine bifunctional ATP sulfurylase/adenosine 5'-phosphosulfate kinase.* J Biol Chem., 1999. **274**(41): p. 28929-36.
79. Tweedie, J.W., Segel, I.H., *ATP-sulfurylase from Penicillium chrysogenum. I. Purification and characterization.* Prep Biochem., 1971. **1**(2): p. 91-117.
80. Yu, M., Martin, R.L., Jain, S., Chen, L.J., Segel, I.H., *Rat liver ATP-sulfurylase: purification, kinetic characterization, and interaction with arsenate, selenate, phosphate, and other inorganic oxyanions.* Arch Biochem Biophys., 1989. **269**(1): p. 156-74.
81. MacRae, I.J., Segel, I.H., Fisher, A.J., *Crystal structure of ATP sulfurylase from Penicillium chrysogenum: insights into the allosteric regulation of sulfate assimilation.* Biochemistry, 2001. **40**(23): p. 6795-804.
82. Murillo, M., Leustek, T., *Adenosine-5'-triphosphate-sulfurylase from Arabidopsis thaliana and Escherichia coli are functionally equivalent but structurally and kinetically divergent: nucleotide sequence of two adenosine-5'-triphosphate-sulfurylase cDNAs from Arabidopsis thaliana and analysis of a recombinant enzyme.* Arch Biochem Biophys., 1995. **323**(1): p. 195-204.
83. Bicknell, R., Cullis, P.M., Jarvest, R.L., Lowe, G., *The stereochemical course of nucleotidyl transfer catalyzed by ATP sulfurylase.* J Biol Chem., 1982. **257**(15): p. 8922-7.
84. Seubert, P.A., Renosto, F., Knudson, P., Segel, I.H., *Adenosinetriphosphate sulfurylase from Penicillium chrysogenum: steady-state kinetics of the forward and reverse reactions, alternative substrate kinetics, and equilibrium binding studies.* Arch Biochem Biophys., 1985. **240**(2): p. 509-23.
85. Renosto, F., Martin, R.L., Borrell, J.L., Nelson, D.C., Segel, I.H., *ATP sulfurylase from trophosome tissue of Riftia pachyptila (hydrothermal vent tube worm).* Arch Biochem Biophys., 1991. **290**(1): p. 66-78.
86. Renosto, F., Patel, H.C., Martin, R.L., Thomassian, C., Zimmerman, G., Segel, I.H., *ATP sulfurylase from higher plants: kinetic and structural characterization of the chloroplast and cytosol enzymes from spinach leaf.* Arch Biochem Biophys., 1993. **307**(2): p. 272-85.
87. Taguchi, Y., Sugishima, M., Fukuyama, K., *Crystal structure of a novel zincbinding ATP Sulfurylase from Thermus thermophilus HB8.* Biochemistry, 2004. **43**: p. 4111-4118.
88. Saridakis, V., Christendat, D., Kimber, M.S., Dharamsi, A., Edwards, A.M., Pai, E.F., *Insights into ligand binding and catalysis of a central step in NAD+ synthesis: structures of Methanobacterium thermoautotrophicum NMN adenylyltransferase complexes.* J Biol Chem., 2001. **276**(10): p. 7225-32.
89. Zhang, H.a.L., T.S., *α-Thio-APS: a stereomechanistic probe of activated sulfate synthesis.* J. Am. Chem. Soc., 1999. **121**: p. 8692–8697.
90. MacRae, I.J., Segel, I.H., Fisher, A.J., *Allosteric inhibition via R-state destabilization in ATP sulfurylase from Penicillium chrysogenum.* Nat Struct Biol., 2002. **9**(12): p. 945-9.

91. MacRae, I.J., Segel, I.H., Fisher, A.J., *Crystal structure of adenosine 5'-phosphosulfate kinase from Penicillium chrysogenum.* Biochemistry, 2000. **39**(7): p. 1613-21.
92. Lansdon, E.B., Segel, I.H., Fisher, A.J., *Ligand-induced structural changes in adenosine 5'-phosphosulfate kinase from Penicillium chrysogenum.* Biochemistry, 2002. **41**(46): p. 13672-80.
93. Monod, J., Wyman, J., Chanfeux, J.P., *On the nature of allosteric transitions: a plausible model.* J Mol Biol., 1965. **12**: p. 88-118.
94. Rubin, M.M., Changeux, J.P., *On the nature of allosteric transitions: implications of non-exclusive ligand binding.* J Mol Biol., 1966. **21**(2): p. 265-74.
95. Segel, I.H., *Enzyme kinetics: behaviour and analysis of rapid equilibrium and steady-state enzyme systems*, ed. Wiley-Interscience. 1993, New York.
96. Venkatachalam, K.V., *Human 3'-phosphoadenosine 5'-phosphosulfate (PAPS) synthase: biochemistry, molecular biology and genetic deficiency.* IUBMB Life, 2003. **55**(1): p. 1-11.
97. Gavel, O.Y., Bursakov, S.A., Calvete, J.J., George, G.N., Moura, J.J.G. and Moura, I., *ATP sulfurylase, a metalloprotein containing cobalt and zinc.* Biochemistry, 1998. **37**: p. 16225–16232.
98. Schulz, G.E., *Binding of nucleotides by proteins.* Curr. Opin. Struct. Biol., 1992. **2**: p. 61-67.
99. Perrier, V., Surewicz, W.K., Glaser, P., Martineau, L., Craescu, C.T., Fabian, H., Mantsch, H.H., Bârzu, O., Gilles, A.-M., *Zinc Chelation and Structural Stability of Adenylate Kinase from Bacillus subtilis.* Biochemistry, 1994. **33**(33): p. 9960–9967.
100. Burlacu-Miron, S., Perrier, V., Gilles, A.-M., Pistotnik, E., and Craescu, C.T., *Structural and Energetic Factors of the Increased Thermal Stability in a Genetically Engineered Escherichia coli Adenylate Kinase.* J. Biol. Chem., 1998. **273**(30): p. 19102-19107.
101. Wolf-Watz, M., Thai, V., Henzler-Wildman, K., Hadjipavlou, G., Eisenmesser, E.Z., Kern, D., *Linkage between dynamics and catalysis in a thermophilic-mesophilic enzyme pair.* Nat Struct Mol Biol., 2004. **11**(10): p. 945-9.
102. Bârzu, O., Michelson, S., *Simple and fast purification of Escherichia coli adenylate kinase.* FEBS Lett., 1983. **153**(2): p. 280-4.
103. Laemmli, U.K., *Cleavage of structural proteins during the assembly of the head of bacteriophage T4.* Nature, 1970. **227**(5259): p. 680-5.
104. Jänis, J., Rouvinen, J., Vainiotalo, P., Turunen, O., Shnyrov, V.L., *Irreversible thermal denaturation of Trichoderma reesei endo-1,4-beta-xylanase II and its three disulfide mutants characterized by differential scanning calorimetry.* Int J Biol Macromol., 2008. **42**(1): p. 75-80.
105. Lumry, R., Eyring, H. , *Conformation changes of proteins.* J. Phys. Chem. , 1954. **58**: p. 110-120.
106. Sreerama, N., Venyaminov, S.Y., Woody, R.W., *Estimation of the number of alpha-helical and beta-strand segments in proteins using circular dichroism spectroscopy.* Protein Sci., 1999. **8**(2).
107. Ulschmid, J.K., Rahlfs, S., Schirmer, R.H., Becker, K., *Adenylate kinase and GTP:AMP phosphotransferase of the malarial parasite Plasmodium falciparum. Central players in cellular energy metabolism.* Mol Biochem Parasitol., 2004. **136**(2): p. 211-20.
108. Maret, W., Vallee, B.L., *Cobalt as probe and label of proteins.* Methods Enzymol., 1993. **226**: p. 52-71.
109. May, S.W., Kuo, J.Y., *Preparation and properties of cobalt(II) rubredoxin.* Biochemistry, 1978. **17**(16): p. 3333-8.
110. Holmquist, B., Vallee, B.L., *Metal-coordinating substrate analogs as inhibitors of metalloenzymes.* Proc Natl Acad Sci U S A., 1979. **76**(12): p. 6216-20.

111. Fenton, D.E., Schroeder, R.R., Lintvedt, R.L., *A unique two-electron reversible reduction of a binuclear copper(Il) complex. Observation of the electrochemical behavior predicted by Polcyn and Shain for the sequential transfer of two electrons at the same potential.* JACS, 1978. **100** p. 1932-1934.
112. Krishnamurthy, H., Munro, K., Yan, H., Vieille, C., *Dynamics in Thermotoga neapolitana adenylate kinase: 15N relaxation and hydrogen-deuterium exchange studies of a hyperthermophilic enzyme highly active at 30 degrees C.* Biochemistry, 2009. **48**(12): p. 2723-39.
113. Venyaminov, S.Y., Vassilenko, K.S., *Determination of protein tertiary structure class from circular dichroism spectra.* Anal Biochem., 1994. **222**(1): p. 176-84.
114. Kahn, P.C., *The interpretation of near-ultraviolet circular dichroism.* Methods Enzymol., 1979. **61**: p. 339-78.
115. Becktel, W.J., Schellman, J.A., *Protein stability curves.* Biopolymers., 1987. **26**(11): p. 1859-77.
116. Privalov, P.L., Potekhin, S.A., *Scanning microcalorimetry in studying temperature-induced changes in proteins.* Methods Enzymol., 1986. **131**: p. 4-51.
117. Zamorano, L.S., Pina, D.G., Arellano, J.B., Bursakov, S.A., Zhadan, A.P., Calvete, J.J., Sanz, L., Nielsen, P.R., Villar, E., Gavel, O., Roig, M.G., Watanabe, L., Polikarpov, I., Shnyrov, V.L., *Thermodynamic characterization of the palm tree Roystonea regia peroxidase stability.* Biochimie, 2008. **90**(11-12): p. 1737-49.
118. Zamorano, L.S., Vilarmau, S.B., Arellano, J.B., Zhadan, G.G., Cuadrado, N.H., Bursakov, S.A., Roig, M.G., Shnyrov, V.L., *Thermal stability of peroxidase from Chamaerops excelsa palm tree at pH 3.* Int J Biol Macromol., 2009. **44**(4): p. 326-32.
119. Klibanov, A.M., Ahern, T.J. , *Thermal stability of proteins*. Protein Engineering, ed. D.L.a.F. Oxender, C. F. 1987, New York: Alan R. Liss. 213–218.
120. Lyubarev, A.E., Kurganov, B.I., *Modeling of irreversible thermal protein denaturation at varying temperature. I. The model involving two consecutive irreversible steps.* Biochemistry (Mosc). 1998. **63**(4): p. 434-40.
121. Lyubarev, A.E., Kurganov, B.I., *Modeling of irreversible thermal protein denaturation at varying temperature. II. The complete kinetic model of Lumry and Eyring.* Biochemistry (Mosc). 1999. **64**(7): p. 832-8.
122. Pace, C.N., Laurents, D.V., *A new method for determining the heat capacity change for protein folding.* Biochemistry, 1989. **28**(6): p. 2520-5.
123. Henzler-Wildman, K.A., Thai, V., Lei, M., Ott, M., Wolf-Watz, M., Fenn, T., Pozharski, E., Wilson, M.A., Petsko, G.A., Karplus, M., Hübner, C.G., Kern, D., *Intrinsic motions along an enzymatic reaction trajectory.* Nature, 2007. **450**(7171): p. 838-44.
124. LeGall, J., Mazza, G., and Dragoni, N., *Cytochrome C3 of Desulfovibrio gigas.* Biochim. Biophys. Acta, 1965. **99**: p. 385-387.
125. Jancarik, J., Kim, S.-H., *Sparse matrix sampling: a screening method for crystallization of proteins.* J. Appl. Cryst., 1991. **24**: p. 409-411.
126. *Collaborative-Computational-Project-Number-4.* Acta Cryst, 1994. **D50**: p. 760-3.
127. Matthews, B.W., *Solvent content of protein crystals.* J. Mol. Biol. , 1968. **33**: p. 491–497.
128. Weiss, M.S., *Global indicators of X-ray data quality.* J. Appl. Cryst., 2001. **34**: p. 130-135.
129. Bae, E., Phillips, G.N.Jr., *Identifying and engineering ion pairs in adenylate kinases. Insights from molecular dynamics simulations of thermophilic and mesophilic homologues.* J Biol Chem., 2005. **280**(35): p. 30943-8.
130. Wild, K., Bohner, T., Aubry, A., Folkers, G., Schulz, G.E., *The three-dimensional structure of thymidine kinase from herpes simplex virus type 1.* FEBS Lett., 1995. **368**(2): p. 289-92.

131. Teplyakov, A., Sebastiao, P., Obmolova, G., Perrakis, A., Brush, G.S., Bessman, M.J., Wilson, K.S., *Crystal structure of bacteriophage T4 deoxynucleotide kinase with its substrates dGMP and ATP.* EMBO J., 1996. **15**(14): p. 3487-97.
132. Vonrhein, C., Bönisch, H., Schäfer, G., Schulz, G.E., *The structure of a trimeric archaeal adenylate kinase.* J Mol Biol., 1998. **282**(1): p. 167-79.
133. Wild, K., Grafmüller, R., Wagner, E., Schulz, G.E., *Structure, catalysis and supramolecular assembly of adenylate kinase from maize.* Eur J Biochem., 1997. **250**(2): p. 326-31.
134. Meng, G., Zhai, R., Liu B. and Zheng X., *Identification of a novel nuclear-localized adenylate kinase from Drosophila melanogaster.* MAIK Nauka, 2008. **73**(1): p. 38-43.
135. Leslie, A.G.W., *Joint CCP4 and ESF-EACBM Newsletters on Protein Crystallography.* 1992. **26**.
136. Kabsch, W., Acta Cryst., 1978. **A34**: p. 827-828.
137. McCoy, A.J., Grosse-Kunstleve, R.W., Adams, P.D., Winn, M.D., Storoni, L.C., Read, R.J., *Phaser crystallographic software.* J. Appl. Cryst., 2007. **40**: p. 658-674.
138. Murshudov, G.N., Vagin, A.A., Dodson, E.J., *Refinement of macromolecular structures by the maximum-likelihood method.* Acta Crystallogr D Biol Crystallogr., 1997. **53**: p. 240-55.
139. Emsley, P., and Cowtan, K., *Coot: model-building tools for molecular graphics.* Acta Cryst. Biological Crystallography, 2004. **D60**: p. 2126–2132.
140. Bellinzoni, M., Haouz, A., Graña, M., Munier-Lehmann, H., Shepard, W., Alzari, P.M., *The crystal structure of Mycobacterium tuberculosis adenylate kinase in complex with two molecules of ADP and Mg^{2+} supports an associative mechanism for phosphoryl transfer.* Protein Sci., 2006. **15**(6): p. 1489-93.
141. Miyoshi, K., Egi, Y., Shioda, T., Kawasaki, T., *Evidence for in vivo synthesis of thiamin triphosphate by cytosolic adenylate kinase in chicken skeletal muscle.* J Biochem., 1990. **108**(2): p. 267-70.
142. Hanas, J.S., Larabee, J.L. & Hocker, J.R., *Zinc finger proteins: From atomic contact to cellular functions*, ed. E.c.a.K.A. Landes Bioscience. Vol. chapter 8. 2005: Plenum Publishers. 39-46.
143. Walker, J.E., Saraste, M., Runswick, M.J., Gay, N.J., *Distantly related sequences in the alpha- and beta-subunits of ATP synthase, myosin, kinases and other ATP-requiring enzymes and a common nucleotide binding fold.* EMBO J., 1982. **1**(8): p. 945-51.
144. Bahar, I., Rader, A.J., *Coarse-grained normal mode analysis in structural biology.* Curr Opin Struct Biol., 2005. **15**(5): p. 586-92.
145. Miyashita, O., Onuchic, J.N., Wolynes, P.G., *Nonlinear elasticity, proteinquakes, and the energy landscapes of functional transitions in proteins.* Proc Natl Acad Sci U S A., 2003. **100**(22): p. 12570-5.
146. Maragakis, P., Karplus, M., *Large amplitude conformational change in proteins explored with a plastic network model: adenylate kinase.* J Mol Biol., 2005. **352**(4): p. 807-22.
147. Lou, H., Cukier, R.I., *Molecular dynamics of apo-adenylate kinase: a principal component analysis.* J Phys Chem B., 2006. **110**(25): p. 12796-808.
148. Suhre, K., Sanejouand, Y.H., *ElNemo: a normal mode web server for protein movement analysis and the generation of templates for molecular replacement.* Nucleic Acids Res., 2004. **32**: p. W610-4.
149. Holm, L., Kääriäinen, S., Rosenström, P., Schenkel, A., *Searching protein structure databases with DaliLite v.3.* Bioinformatics, 2008. **24**(23): p. 2780-1.
150. Mulder, G.J., *Sulfation of drugs and related compounds*. CRC Press, Boca Raton, ed. G.J. Mulder, Ed. 1982. 56-69.
151. Robbins, P.W., and Lipmann, F., *Separation of the two enzymatic phases in active sulfate synthesis.* J. Biol. Chem., 1958. **233**: p. 681-685.

152. Robbins, P.W., and Lipmann, F., *Enzymatic synthesis of Adenosine-5'- Phosphosulfate.* J. Biol. Chem., 1958. **233**: p. 686-690.
153. Ullrich T.C., B.M., Huber R., *Crystal structure of ATP sulfurylase from Saccharomyces cerevisiae, a key enzyme in sulfate activation.* EMBO J., 2001a. **20**(3): p. 316-29.
154. Ullrich, T.C., and Huber, R., *The complex structures of ATP sulfurylase with thiosulfate, ADP and chlorate reveal new insights in inhibitory effects and the catalytic cycle.* J. Mol. Biol., 2001b. **313**: p. 1117-1125.
155. Beynon, J.D., MacRae, I.J., Huston, S.L., Nelson, D.C., Segel, I.H., and Fisher, A.J., *Crystal structure of ATP sulfurylase from the bacterial symbiont of the hydrothermal vent tubeworm Riftia pachyptila.* Biochemistry, 2001. **40**: p. 14509–14517.
156. Taguchi, Y., Hoseki, J., Kakuta, Y., and Fukuyama, K., *Overproduction, crystallization and preliminary X-ray diffraction analysis of probable ATP sulfurylase from Thermus thermophilus HB8.* Acta Cryst. Biological Crystallography, 2003. **D59**: p. 1645-1647.
157. Long, F., Vagin, A.A., Young, P., and Murshudov, G.N. , *BALBES: a molecular-replacement pipeline.* Acta Cryst. Biological Crystallography, 2008. **D64**: p. 125–132.
158. Bradley M.E., R.J.S., Li W.-H., Schwartz N.B., *Sulfate Activation Enzymes: Phylogeny and Association with Pyrophosphatase.* J. Mol. Evol., 2009. **68**: p. 1-13.
159. Valdés, J., Veloso, F., Jedlicki, E., Holmes, D., *Metabolic reconstruction of sulfur assimilation in the extremophile Acidithiobacillus ferrooxidans based on genome analysis.* BMC Genomics., 2003. **4**(1): p. 51.
160. Homsher, R., Zak, B., *Spectrophotometric investigation of sensitive complexing agents for the determination of zinc in serum.* Clin Chem., 1985. **31**(8): p. 1310-3.
161. Evans, C.H., *The spectrophotometric determination of micromolar concentrations of Co2+ using o-phenanthroline.* Anal Biochem., 1983. **135**(2): p. 335-9.
162. Lopez-Mayorga, O., Freire, E., *Dynamic analysis of differential scanning calorimetry data.* Biophys Chem., 1987. **27**(1): p. 87-96.
163. Li, J.J., Saidha, T., Schiff, J.A., *Purification and properties of two forms of ATP sulfurylase from Euglena.* Biochim Biophys Acta., 1991. **1078**(1): p. 68-76.
164. Osslund, T., Chandler, C., Segel, I.H., *ATP Sulfurylase from Higher Plants : Purification and Preliminary Kinetics Studies on the Cabbage Leaf Enzyme.* Plant Physiol., 1982. **70**(1): p. 39-45.
165. Renosto, F., Schultz, T., Re, E., Mazer, J., Chandler, C.J., Barron, A., Segel, I.H., *Comparative stability and catalytic and chemical properties of the sulfate-activating enzymes from Penicillium chrysogenum (mesophile) and Penicillium duponti (thermophile).* J Bacteriol., 1985. **164**(2): p. 674-83.
166. Auld, D.S., *Zinc coordination sphere in biochemical zinc sites.* Biometals., 2001a. **14**(3-4): p. 271-313.
167. Auld, D.S., *Handbook on metalloproteins*. Marcel Dekker, ed. A.S.a.H.S.e. in I.Bertini. 2001b, New York.
168. Bertini, I., *The coordination chemistry of metalloproteins*, ed. D.R.S. Bertini I., Luchinat C. . 1983: Reidel Publishing Co., Dordrecht, the Netherlands.
169. Maret, W., Vallee, B.L., *Thiolate ligands in metallothionein confer redox activity on zinc clusters.* Proc Natl Acad Sci U S A., 1988. **95**(7): p. 3478-82.
170. Permyakov, E.A., Reyzer, I.L., Berliner, L.J., *Effects of Zn(II) on galactosyltransferase activity.* J Protein Chem., 1993. **12**(5): p. 633-8.
171. Freire, E., Comm. Mol. Cell. Biophys. , 1989. **6**: p. 123-140.
172. Sanchez-Ruiz, J.M., *Theoretical analysis of Lumry-Eyring models in differential scanning calorimetry.* Biophys J., 1992. **61**(4): p. 921-935.
173. Kurganov, B.I., Lyubarev, A.E., Sanchez-Ruiz, J.M., Shnyrov, V.L., *Analysis of differential scanning calorimetry data for proteins. Criteria of validity of one-step mechanism of irreversible protein denaturation.* Biophys Chem., 1997. **69**(2-3): p. 125-35.

174. Elamrani, S., Berry, M.B., Phillips, G.N.Jr, McCammon, J.A., *Study of global motions in proteins by weighted masses molecular dynamics: adenylate kinase as a test case.* Proteins, 1996. **25**(1): p. 79-88.
175. Vasák, M., Kägi, J.H., Holmquist, B., Vallee, B.L., *Spectral studies of cobalt (II)- and Nickel (II)-metallothionein.* Biochemistry, 1981. **20**(23): p. 6659-64.
176. Swenson, D., Baenziger, L.N., Coucouvanis, D., *Tetrahedral mercaptide complexes. Crystal and molecular structures of [(C H)4P] M(SC H) complexes (M = cadmium(II), zinc(II), nickel(II), cobalt(II), and manganese(II)).* J. Am. Chem. Soc., 1978. **100**: p. 1932-1934.